Master's Thesis

Engineering Balloon Flight (JAXA TARF B23-06) for the GRAMS Experiment

July 26th 2024

Waseda University

Graduate School of Advanced Science and Engineering

Department of Pure and Applied Physics

Yorita Kohei Laboratory

5322AG03-2 Riki NAKAJIMA

Abstract

Dark matter, constituting approximately 25% of the mass-energy content of the universe, remains one of the most profound mysteries in modern physics. The true nature of dark matter is yet to be known with numerous experiments designed for its search.

The GRAMS experiment is a next-generation balloon experiment utilizing a liquid argon time projection chamber (LArTPC) which aims to simultaneously detect MeV gamma rays and low-energy cosmic antiparticles. The final objective of the GRAMS experiment is a long-duration balloon flight at the South Pole where the rigidity cutoff is lowered enabling the detection of low-energy cosmic rays (antideuterons for indirect dark matter search).

As LAr is cost-effective and abundant in the atmosphere, it has been widely used in numerous experiments. However, a LArTPC has never been operated at balloon altitudes. Therefore, an engineering flight using a prototype LArTPC (with 3ch), accepted by JAXA's balloon committee was conducted on 27th July 2023, marking a crucial milestone for GRAMS. The main goal of this flight was to monitor and control LAr during the flight and obtain environmental data to understand the LAr response to balloon altitudes. Furthermore, operating the LArTPC to obtain cosmic ray data was another objective. As this was the first balloon flight for the GRAMS collaboration, it was important to identify R&D issues that may become crucial for upcoming balloon flights with larger LArTPCs and complex systems.

The payload consisted of a gondola which held the cryostat containing LAr with the detector system, a pressurized vessel for all the electronics, JAXA's balloon bus system for radio communication with the ground, and two other piggyback experiments. To handle LAr, an absolute pressure valve was used with a differential pressure valve and rupture disk for safety. During the descent, LAr was to be evacuated for safety measures.

The flight was successfully conducted on 27th July 2023 in which the balloon reached a maximum altitude of 28.9 km and 44 minutes of level flight was achieved. During the flight, LAr conditions were monitored and controlled stably. Also, the LArTPC was successfully operated to obtain cosmic ray data. During the descent, the LAr was fully evacuated and the recovery of the gondola with the flight data was completed. In analyzing the LArTPC data, the purity of LAr was evaluated and the LAr purity was maintained at a sub-ppb level during the flight. Furthermore, the rate of cosmic rays entering the LArTPC was calculated, which was compared to a Geant4 simulation. The results show that both the data and simulation exhibit a shower maximum curvature at 20 km.

Looking ahead, a balloon flight funded by the NASA/APRA program is planned to be launched in Arizona, USA between fall 2025 and spring 2026. For this flight, a larger LArTPC with particle tracking ability will be used which will require a larger cryostat and upgraded electronics. In preparing for the next balloon flight, the insights gained from this engineering flight will be leveraged and applied. Additionally, further preparations are ongoing for the balloon flight at the South Pole in the 2030s and a possible satellite mission in the future.

Contents

List of Figures

List of Tables

1 Dark Matter

This section introduces the characteristics of dark matter and delves into various pieces of evidence on the existence of dark matter from cosmological observations. Subsequently, it covers the leading candidate for dark matter, describing the various search methods and current/past experiments with a particular focus on indirect dark matter search through cosmic antiparticles. This focus on indirect searches is one of the key motivations for the GRAMS experiment.

1.1 About Dark Matter

Dark matter is a hypothetical, non-luminous mass in the universe that could provide explanations for numerous cosmological and astrophysical observations, ranging from the scale of individual galaxies to the entire universe. Being non-luminous (dark) derives from the fact that dark matter does not interact electromagnetically. Moreover, it must be extremely long-lived, at least comparable to the age of the universe; it must interact with other particles at the weak scale; and it must be non-relativistic (cold) as the universe ages.

Recent observations made by the Planck observatory on the Cosmic Microwave Background (CMB) suggest that the universe is roughly 68% dark energy, 27% dark matter, and 5% ordinary matter as shown in Figure 1.1

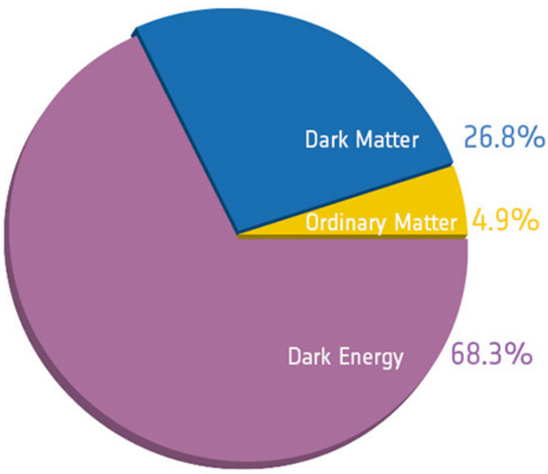

Figure 1.1: Composition of the universe from the CMB.

Despite the Standard Model (SM) of particle physics being able to explain physical phenomena below the electroweak scale, there is no single particle in the SM that fits the characteristics of dark matter. Consequently, the discovery and understanding of dark matter are crucial for particle physics and astronomy.

1.2 Dark Matter Evidence

The existence of dark matter has been confirmed by various cosmological and astrophysical observations. However, all of the accumulated evidences rely on the gravitational effect of dark matter and its true nature is still yet to be known. Dark matter was first introduced by Fritz Zwicky in the mid-1930s when he applied the virial theorem to the dynamics of the Coma Cluster. He found out that the calculated mass-to-light ratio of the galaxies in the Coma Cluster is approximately 800 solar units, which is several orders of magnitude greater than what one would expect if the mass of the Coma galaxies is mostly stars [1].

Four decades after Zwicky's initial observations on the Coma Cluster, Rubin, Ford, and Thonnard began to analyze the rotation curves of galaxies using new spectroscopic techniques. They measured the rotation curves of the Andromeda Galaxy via the Doppler shift of the spectral signatures and discovered a flat rotation curve. This suggested the existence of invisible mass extending beyond the stars and gas clouds [2]. From Kepler's law and Newtonian dynamics, the rotation velocity of a galaxy can be expressed as:

$$\frac{v(r)^2}{r} = G\frac{M(r)}{r^2} \tag{1.1}$$

Where r is the radius of the galaxy, $v(r)$ is the rotation velocity, G is the gravitational constant, and $M(r)$ is the total mass of the galaxy. Since $v(r)$ is inversely proportional to r, at the outer regions of the galaxy where r is large, the rotation velocity should decrease. However, from the observation of galaxy NGC 3198 [3] shown in Figure 1.2, the rotation velocity stays constant as the radius increases.

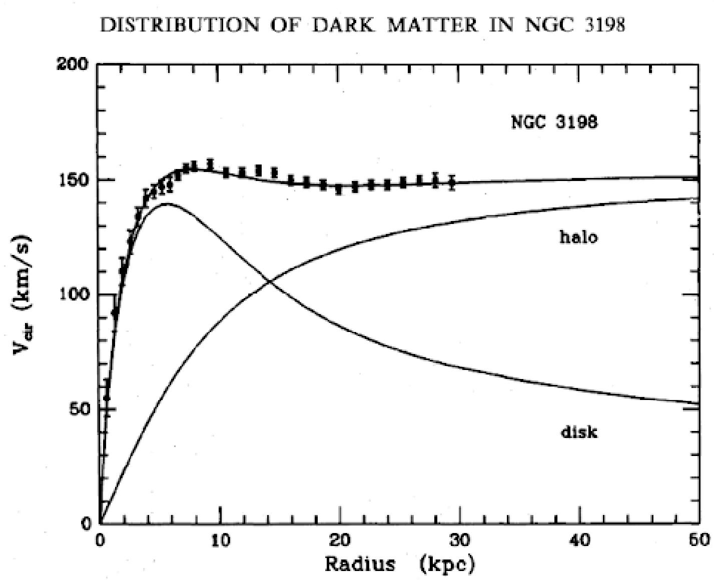

Figure 1.2: Rotation curve of galaxy NGC 3198.

An alternative method, rather than depending solely on visible matter, utilizes the phenomenon of gravitational lensing. Light from a distant source is bent as it travels towards the observer due to massive celestial bodies causing a sufficient curvature of spacetime. This method was used when observing two colliding galaxy clusters. Figure 1.3 shows the image of the Bullet cluster where the x-ray emission taken by the x-ray telescope and the gravitational potential seen with the gravitational lens is mapped as the pink and blue regions correspondingly [4]. From the separation of the pink and blue regions, it is deduced that most of the luminous matter is concentrated in the region of collision. Whereas, the gravitational mass resides in the outer region, probing as a direct evidence of dark matter.

Figure 1.3: Image of the colliding galaxy clusters (the Bullet cluster, 1E 0657-56).

1.3 Weakly Interacting Massive Particle

A leading candidate for non-baryonic cold dark matter is weakly interacting massive particles (WIMP). It is a hypothesized particle with masses ranging from GeV/c^2 to TeV/c^2, interacting with ordinary matter at or below the weak scale. The interest in WIMPs as dark matter stems from the fact that WIMPs in thermal equilibrium in the early Universe could naturally explain the relic density of dark matter in the current universe. By assuming that WIMPs can annihilate into ordinary matter (SM particles), WIMPs χ and SM particles q are in thermal equilibrium during the early universe when the temperature is extremely high ($\chi\chi \rightleftarrows qq$). Furthermore, the time evolution of WIMP number density n_χ is explained by the Boltzmann equation,

$$\frac{d}{dt}n_\chi = -3Hn_\chi - \langle\sigma_{ann}\nu\rangle(n_\chi^2 - n_{\chi,eq}^2) \tag{1.2}$$

where H is the Hubble Constant, $\langle\sigma_{ann}\nu\rangle$ is the thermally averaged annihilation cross section and $n_{\chi,eq}$ is the co-moving number density in thermal equilibrium.

As the universe expands and the temperature cools, the WIMP production rate will decrease due to SM particles having insufficient energy for WIMP pair production to occur. Also, the WIMP annihilation rate will decrease due to the average distance between WIMPs increasing. Following this, the number density of WIMPs in an expanding volume will be in a "freeze-out" state as shown in Figure 1.4. The current WIMP density can be numerically calculated from Eq.(1.3) as

$$\Omega_\chi \approx 0.2 \left(\frac{1pb \cdot c}{\langle \sigma_{ann} \nu \rangle} \right) \tag{1.3}$$

By considering an electroweak scale particle with mass m_χ =100 GeV/c^2 and coupling constant $\alpha = 0.01$, $\langle \sigma_{ann} \nu \rangle \approx \alpha^2/m_\chi^2 = 1$ pb. This then agrees with the observed relic density of dark matter $\Omega_\chi \approx 0.27$, often named the "WIMP miracle" [5].

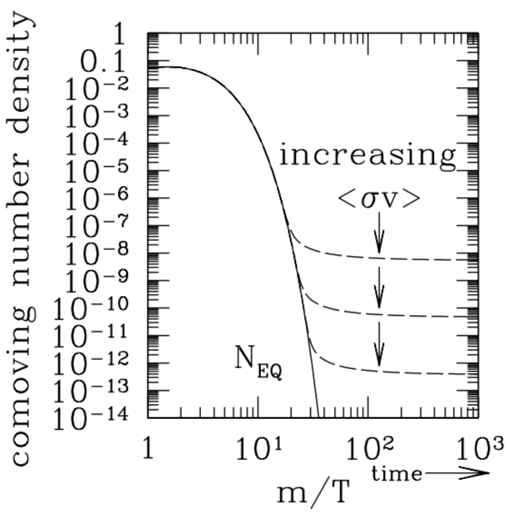

Figure 1.4: Time evolution of WIMP co-moving number density.

There are three interaction channels between WIMP and SM particles which probes methods to detect WIMP dark matter. As shown in Figure 1.5, the three interactions are annihilation, scattering (DM-SM interaction), and production. The annihilation process is used in indirect searches, looking for heavy cosmic antiparticles originating from dark matter. Additionally, the scattering process is used in direct searches in which the signal originates from the elastic scattering between the detector material and dark matter. Finally, the production process is used in collider experiments, where high-energy particles are collided to produce other particles to search for invisible mass.

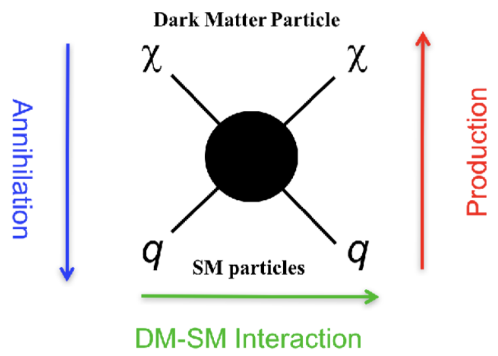

Figure 1.5: Interactions between dark matter and SM particles.

1.4 Indirect Dark Matter Search with Cosmic Antiparticles

Various particles are raining down from outer space, including antiparticles such as antiprotons and positrons. Antiparticles are thought to be produced secondarily when primary cosmic rays such as protons collide with interstellar gas in the universe as they propagate through the galaxy. After being produced, cosmic ray antiparticles are affected by various physical phenomena before they propagate through the galaxy and the heliosphere to reach the Earth. Therefore, measuring the flux of cosmic rays is very important for understanding the propagation model of cosmic rays and solar modulation. It has also been suggested that antiparticles may be produced by annihilation or decay of dark matter. Secondary antiparticles are limited in their production at low energies due to the kinematics of collisions, while primary antiparticles (produced from dark matter) are not limited by kinematics and may therefore be distinguished from secondary antiparticles. Although positrons and antiprotons have already been observed in various experiments, it is difficult to distinguish between dark matter-induced and secondary cosmic antiparticles because the flux of secondary cosmic antiparticles is larger than the predicted flux from dark matter. Therefore, the search for antideuterons, in which the flux of secondary cosmic antiparticles is smaller than the predicted flux due to dark matter, is now attracting attention and could be a smoking gun for indirect dark matter search.

1.4.1 Cosmic Antideuteron

A single antideuteron atom is a bound state of antiproton and antineutron, therefore having a charge of $-1e$. The first observation of antideuteron occurred in 1965 with a collider experiment. However, cosmic antideuterons have never been observed yet. [6]

- **Antideuterons from ISM Collision (Secondary)** [7]

The source term for cosmic antideuterons from ISM collision is given as:

$$Q_{\bar{d}}^{sec}\left(\mathbf{r}, E_{kin}^{\bar{d}}\right) = \sum_{i\in\{p,He,\bar{p}\}} \sum_{i\in\{p,He\}} 4\pi n_j\left(\mathbf{r}\right) \times \int_{E_{kin,min}^{i}}^{\infty} dE_{kin}^{i} \left(\frac{d\sigma_{prod}}{dE_{kin}^{\bar{d}}}\right)_{ij} \Phi_i\left(\mathbf{r}, E_{kin}^{i}\right) \quad (1.4)$$

In this equation, all incident cosmic ray species are represented by i with flux Φ_i and kinematic energy per nucleon E_{kin}^{i}. The index j represents the ISM components with the number densities: $n_p = 0.9\ \mathrm{cm}^{-3}$ and $n_{He} = 0.1\ \mathrm{cm}^{-3}$ used to calculate source functions. The term $\left(\frac{d\sigma_{prod}}{dE_{kin}^{\bar{d}}}\right)$ represents the antideuteron differential production cross section with the primary cosmic ray fluxes involved in the collision.

- **Antideuterons from Dark Matter (Primary)**

The source term for cosmic antideuterons from dark matter annihilation is given as:

$$Q_{\bar{d}}^{DM,ann}\left(\mathbf{r}, E_{kin}^{\bar{d}}\right) = \frac{1}{2}\left(\frac{\rho\left(\mathbf{r}\right)}{m_{DM}}\right)^2 \langle\sigma\mu\rangle_f \frac{dN_f^{\bar{d}}}{dE_{kin}^{\bar{d}}} \quad (1.5)$$

where $\rho(\overrightarrow{r})$ is the local dark matter density, $\langle\sigma\mu\rangle_f$ is the velocity averaged dark matter annihilation cross section into given channels such as $\chi\chi \rightarrow b\bar{b}$ or W^-W^+. The antideuteron multiplicity produced from one annihilation event is represented as $\frac{dN_f^{\bar{d}}}{dE_{kin}^{\bar{d}}}$.

The cosmic ray propagation can be described by the Fokker-Planck equation:

$$\frac{\partial\psi}{\partial t} = Q\left(\mathbf{r}, p\right) + \nabla\cdot\left(D_{XX}\nabla\psi - \mathbf{V}\psi\right) + \frac{\partial}{\partial p}p^2 D_{pp}\frac{\partial}{\partial p}\frac{\psi}{p^2} - \frac{\partial}{\partial p}\left[\psi\frac{dp}{dt} - \frac{p}{3}\left(\nabla\mathbf{V}\right)\psi\right] - \frac{\psi}{\tau} \quad (1.6)$$

where $\psi = \psi\left(\mathbf{r}, p, t\right)$ is the time-dependent cosmic ray density per unit of the total particle momentum at position $\mathbf{r}$. The source term of a given cosmic ray (primary or secondary) is represented as $Q\left(\mathbf{r}, p\right)$. The spatial diffusion coefficient is given as D_{XX}, the convection velocity as $\mathbf{V}$, and the diffusive re-acceleration coefficient as D_{pp}. The last term $\frac{\psi}{\tau}$ accounts for particles lost via decay. By using the source terms described above, the flux of antideuterons can be calculated which is shown in Figure 1.6. The left and right plots in Figure 1.6 show the antideuteron flux from dark matter annihilating to $b\bar{b}$ and W^-W^+, respectively. It can be seen that as the mass of dark matter increases, the peak shifts to the right, and the flux is decreased. Furthermore, at low energies, the antideuteron flux from dark matter annihilation is an order or two of magnitude larger than the background (ISM collision produced antideuterons).

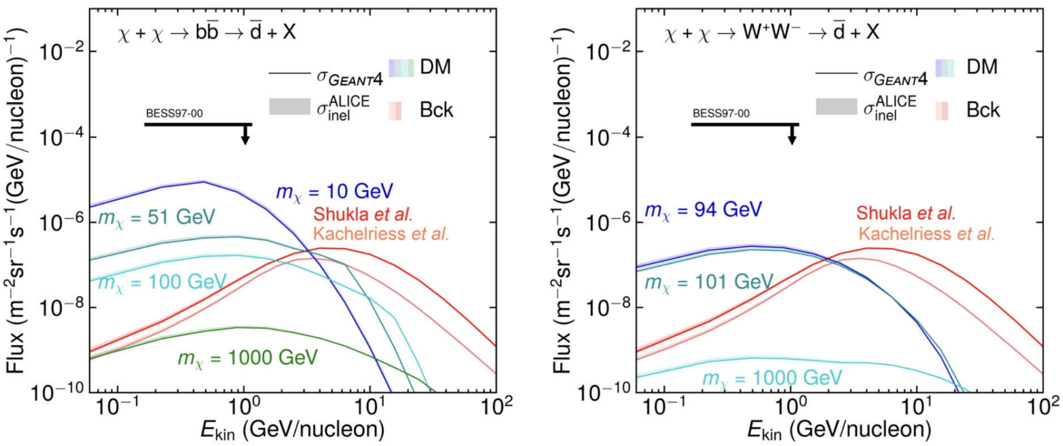

Figure 1.6: Antideuteron fluxes from cosmic ray collisions and dark matter annihilation.

1.4.2 Experiments Searching for Cosmic Antiparticles

- **AMS-02 Experiment** [8]

The AMS-02 experiment (AMS: Alpha Magnetic Spectrometer) is a satellite experiment on the International Space Station (ISS) operating at an altitude of about 410 km, with the objective to precisely measure fluxes of cosmic (anti)particles. The detector configuration is shown in Figure 1.7: A permanent magnet to bend incoming particles, TRD to identify electrons/positrons, ToF to measure the velocity and dE/dx of incoming particles, silicon detector to measure charge and track the particle trajectory, Ring Imaging Cerenkov Detector (RICH) to further measure charge and velocity for higher energies, Anit-Coincidence Counters (ACC) to identify particles incident on the side of the detector and a calorimeter (ECAL). Particle identification can be performed by combining information obtained from multiple detectors. Particularly, the identification of electric charges and momentum using the velocity and curvature of the particle track.

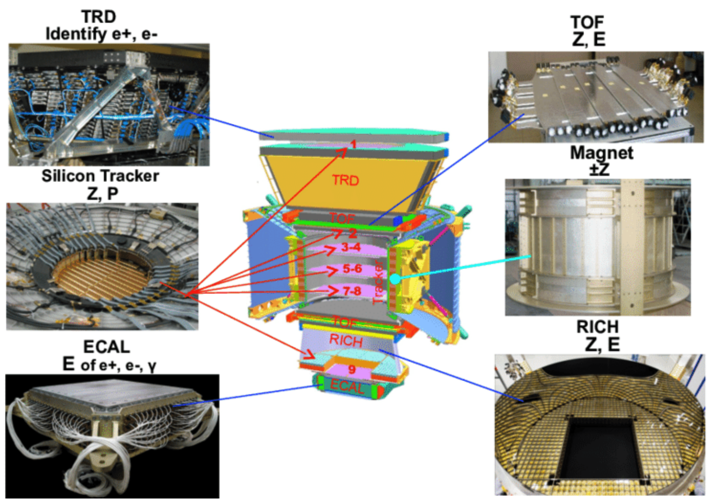

Figure 1.7: AMS-02 detector design.

Among the numerous nuclei AMS-02 has detected over the past years, antiprotons are particularly interesting for dark matter search. Figure 1.8 shows the measured antiproton flux. The measured antiproton flux shown in red can be mostly described by the background component shown in green. Here, the background components are secondary antiprotons produced from the collision of primary cosmic rays and interstellar medium, described in the previous section. However, in the low energy region, there is an excess in the measured antiproton flux. The primary antiproton flux from dark matter annihilation could explain this excess, where the dark matter mass ranges from 20 to 80 GeV with a cross-section of $(0.2 - 5) \times 10^{-26}$ $cm^3 s^{-1}$, for the $b\bar{b}$ channel. The primary antiproton flux shown in Figure 1.8 is 47 GeV. Therefore, these observations from AMS-02 provide valuable constraints on the parameter space of dark matter models, guiding future searches and theoretical developments.

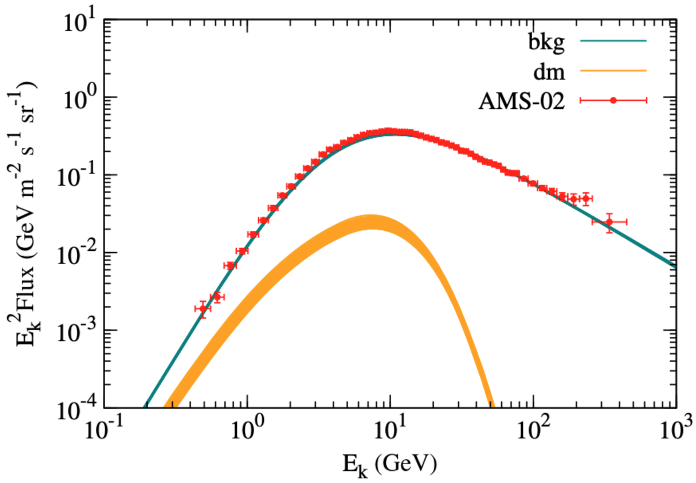

Figure 1.8: Antiproton flux measured by AMS-02.

- **BESS Experiment** [9]

The BESS experiment is a balloon experiment using a cylindrical detector equipped with a superconducting magnet that has been flown over Antarctica for a total of more than 30 days in 2004 (BESS-Polar I) and 2007-2008 (BESS-Polar II). The detector consists of an internal track detector, a solenoid coil, an aerogel Cerenkov counter, and a ToF scintillator. A schematic diagram of the detector is shown in Figure 1.9.

The upper and lower ToF scintillators measure the velocity of the particles, and the JET chamber and the ToFs measure dE/dx. In addition, particle identification is possible by bending the incoming charged particles with the magnet and measuring the rigidity and mass of incoming particles with an internal track detector surrounded by solenoid coils. The BESS-Polar II experiment was successful in measuring cosmic ray fluxes with a flight duration of 30 days. Although no antideuterons were observed, it is the only experiment to place an upper limit on the antideuteron sensitivity as shown in Figure 1.10 [10]. When considering the primary flux of antideuterons from dark matter with a

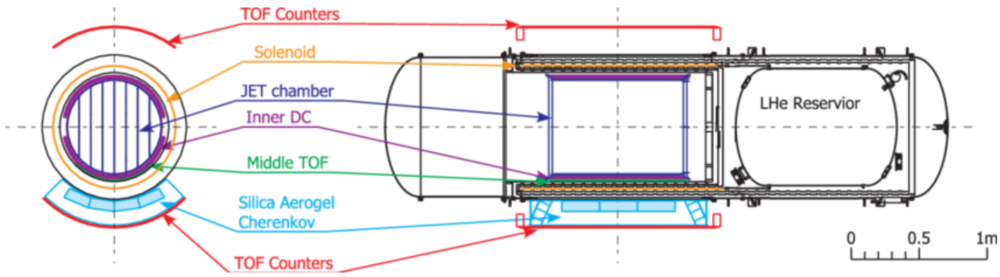

Figure 1.9: BESS-Polar II detector.

mass of around 50 GeV, the sensitivity has to be lowered by almost 2 orders of magnitude to detect a single antideuteron.

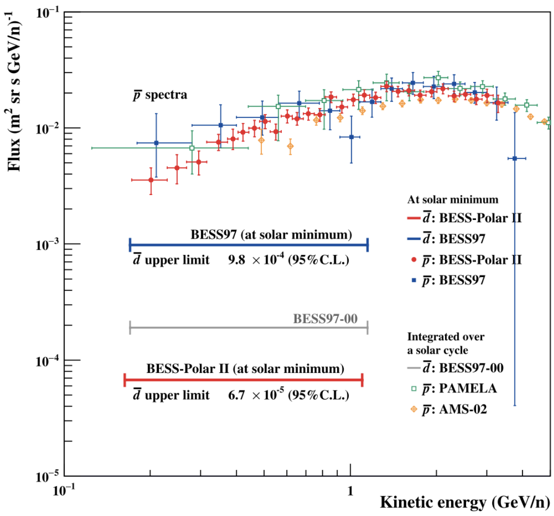

Figure 1.10: Measured antiproton flux and antideuteron upper limits.

- **GAPS Experiment** [11]

The General Anti-Particle Spectrometer (GAPS) project is a current-generation balloon experiment searching for low-energy cosmic antiparticles. Unlike AMS-02 and BESS, the GAPS detector does not use a magnet for particle identification. The detector design is shown in Figure 1.11 where a ToF system surrounds the Si(Li) trackers. As a magnet is not used, the particle identification is done by the velocity information from the ToFs, dE/dx, and range (if stopped) from the Si trackers and an exotic atom technique described in Section 2.3.1 and shown in Figure 1.12. Incoming negatively charged particles are captured by Si nuclei and form an exotic atom with the Si nucleus. The negatively charged particles emit characteristic X-rays as they undergo de-excitation, finally annihilating with the nucleus to produce multiple hadrons that can be detected. By using such a strategy, the mass volume of the detector is reduced as a magnet is not needed and hence enables low-energy particles to reach the detector volume. The exotic atom technique has been validated in an antiproton beam test using nitrogen gas as the detector material [12], and a balloon experiment (pGAPS) [13] with a prototype detector was successfully conducted in June 2012 in Hokkaido, Japan. The GAPS project is currently preparing for a long-duration flight in Antarctica planned in late 2024 with projected sensitivities shown in Figure 2.2.

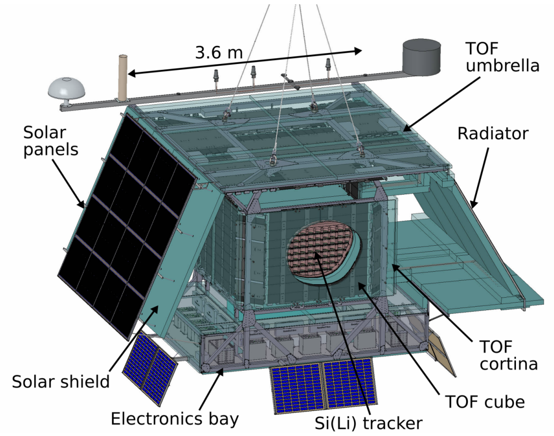

Figure 1.11: GAPS detector design.

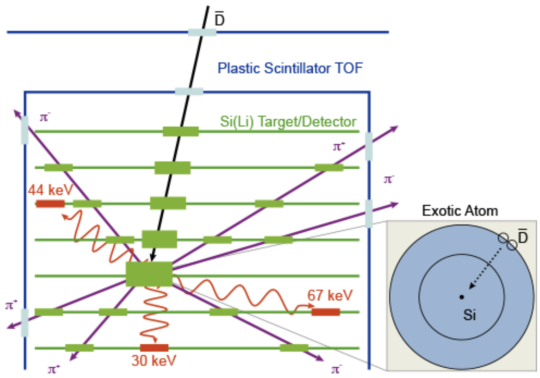

Figure 1.12: GAPS detection technique.

2 GRAMS Experiment

The GRAMS experiment (Gamma-Ray And AntiMatter Survey) is a next-generation balloon experiment using a liquid argon time projection chamber (LArTPC), aiming at a long-duration balloon flight in Antarctica and a satellite mission in the future. It is the first project to simultaneously target both astrophysical observations of MeV gamma rays and indirect dark matter search through cosmic antiparticles. Currently, the project is being conducted jointly by Waseda University, Osaka University, Northeastern University, Columbia University, and other research institutes in Japan and the United States. At Waseda University, the R&D for GRAMS is particularly focused on indirect dark matter search using cosmic antiparticles. In this section, an overview of the GRAMS experiment will be given, describing the detector design, detection concept, milestones, and a brief introduction to the R&D being conducted at Waseda University.

2.1 Physics Goals

As stated above, the GRAMS experiment has two main physics goals: astrophysical observation of MeV gamma rays and indirect dark matter search with cosmic antiparticles.

Recent astrophysical observations from the Large Area Telescope [14] and the Nuclear Spectroscopic Telescope Array (NuSTAR) [15] have improved the sensitivities and unraveled physics in the hard X-Ray (up to 80 keV) and high-energy gamma ray (above 20 MeV) regions, respectively. On the other hand, gamma rays in the MeV energy range have not been well explored. As shown in Figure 2.1, the Imaging COMPton TELescope (COMPTEL) currently sets the best sensitivity in the MeV region, however only 30 objects have been detected [16]. The difficulty in MeV gamma-ray physics arises from the interaction of MeV gamma rays being Compton scattering dominated which complicates the event reconstruction and the vast background from in and out of the detector volume. However, gamma-ray astronomy in the MeV energy region is key to understanding nucleosynthesis processes from nuclear line emissions and various astrophysical phenomena.

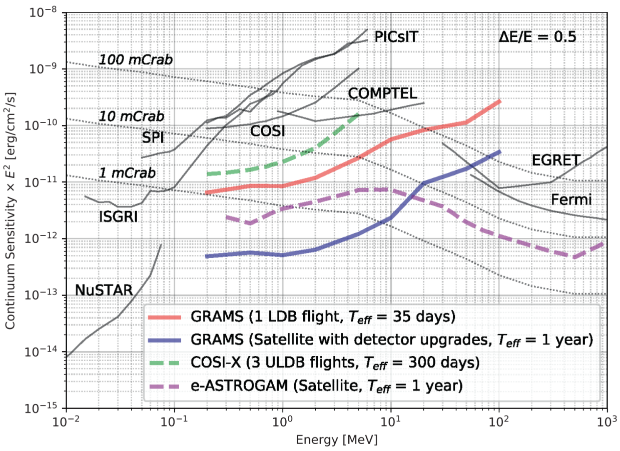

Figure 2.1: Continuum gamma-ray sensitivities.

In addition, as stated in Section 1.4.1, low-energy antideuterons are of particular interest due to the flux of antideuterons from dark matter annihilation being an order or two of magnitude larger than the background. Figure 2.2 shows the predicted antideuteron flux from 30 GeV dark matter annihilating into $b\bar{b}$ and the target sensitivity of GRAMS.

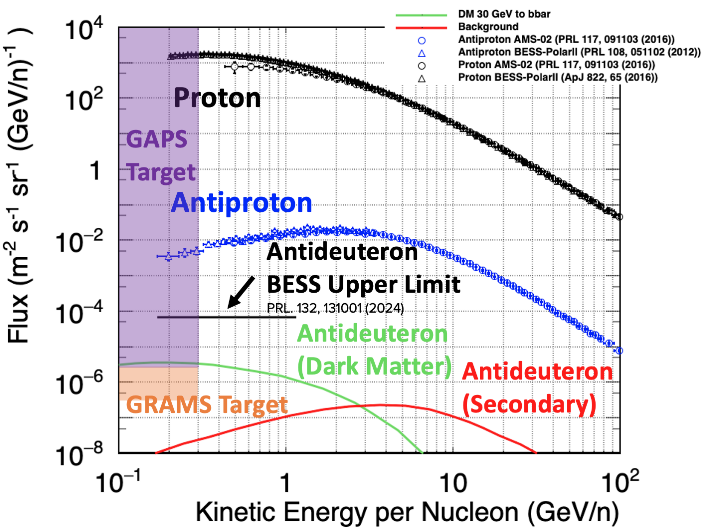

Figure 2.2: Antideuteron flux from 30 GeV dark matter and target sensitivity.

2.2 Liquid Argon Time Projection Chamber (LArTPC)

As LAr is dense (40% denser than water), abundant (1% of the atmosphere) and very sensitive to incoming particles (40 photon/keV for scintillation and 1 fc/mm for ionization), Liquid Time Projection Chambers (LArTPC) have therefore become standard technology in particle physics experiments particularly for direct detection and neutrino experiments [17–19]. Further details of liquid argon characteristics and the operation principle of a LArTPC will be discussed in the following sections.

2.2.1 LAr Characteristics

Argon is a noble gas and the third most abundant gas in the atmosphere which enables detector volumes to be increased with lower cost compared to other less abundant materials. The basic properties of liquid argon are shown in Table 2.1 [20] and the phase diagram is shown in Figure 2.3. The W-values on Table 2.1 are of liquid argon. As shown in Figure 2.3, a liquid phase does not exist below 0.7 bar, and at 1 bar, the liquid and gas phases are only separated by a few degrees. Therefore in operating and maintaining liquid argon in a detector, it is extremely important to control the pressure and temperature.

When a particle interacts with liquid argon, the energy is deposited in two main channels other than heat: ionization and excitation as illustrated in Figure 2.4. The equation for ionization can be written as:

$$Ar + E_{recoil} \rightarrow Ar^{+} + e^{-} \tag{2.1}$$

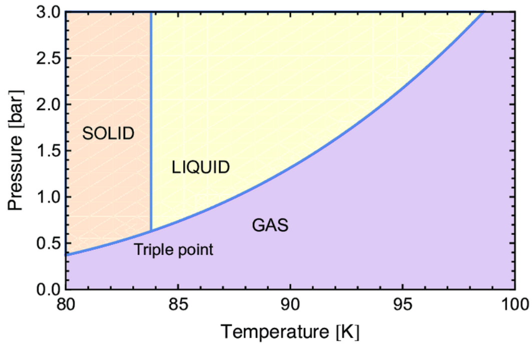

Figure 2.3: Phase diagram of argon.

Property	Value
Atomic Number	18
Atomic Weight	39.9
Boiling Point (1atm)	87.3 K
Melting Point (1atm)	83.8 K
Density (Liquid)	1.395 g/cm^3
W-Value (Ionization)	23.6 eV
W-Value (Scintillation)	19.5 eV
Scintillation Wavelength	128 nm

Table 2.1: Properties of argon.

If there is an electric field applied, the majority of the ionized electrons will drift along the electric field and a portion will recombine with surrounding argon atoms to form an Ar_2^* excimer [21]. The recombination factor can be expressed as:

$$R = \frac{Q_{rec}}{Q_0} = \frac{A}{1 + \frac{E}{k} \cdot \frac{dE}{dx} \cdot \frac{1}{p}} \tag{2.2}$$

where Q_0 is the number of ionized electrons, Q_{rec} is the number of ionized electrons after recombination, E is the applied electric field, ρ is the liquid argon density and A and k are fit parameters ($A = 0.800 \pm 0.003, k = 0.0486 \pm 0.0006$). Moreover, electronegative impurities such as oxygen and water have to be filtered out as the ionized electrons get absorbed:

$$O_2 + e^- \rightarrow O_2^- \tag{2.3}$$
$$H_2O + e^- \rightarrow H_2O^- \tag{2.4}$$

The primary scintillation signal in liquid argon results from the relaxation of the Ar_2^* excimer as shown as:

$$Ar + E_{recoil} \rightarrow Ar^* \tag{2.5}$$
$$Ar^* + 2Ar \rightarrow Ar_2^*({}^1\Sigma_u^+ or {}^3\Sigma_u^+) + Ar \tag{2.6}$$
$$Ar_2^* \rightarrow 2Ar + h\nu(128nm) \tag{2.7}$$

The Ar^* exciton immediately forms an excimer of either a single or triplet state (with lifetimes of 7 ns and 1.6 μs) and decays. The scintillation light spectrum peaks at 128 nm and lies in the vacuum ultraviolet (VUV) region.

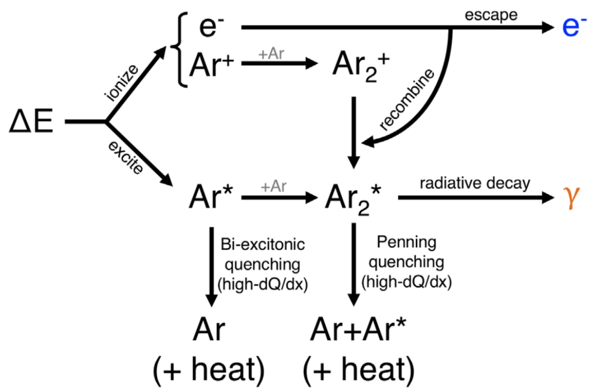

Figure 2.4: Ionization and excitation channels in liquid argon.

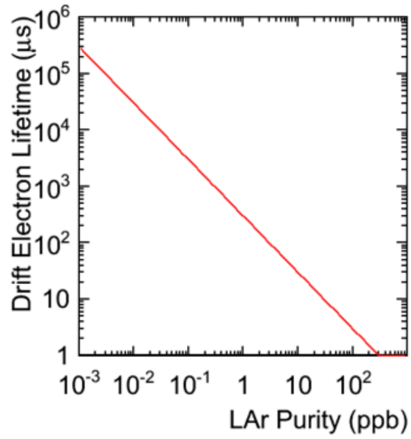

Figure 2.5: Lifetime of ionized electrons against LAr purity.

2.2.2 LArTPC Operation Principle

A LArTPC detector uses ionization electrons and scintillation light signals to measure dE/dx and track particles. A schematic diagram of a LArTPC is shown in Figure 2.6. As stated in the previous section, when a particle deposits energy in liquid argon, ionized electrons and scintillation light are produced. By applying an electric field between the cathode and anode, the electrons drift towards the anode plane for charge readout where the X and Y positions of the ionized electrons are obtained. The anode can be wired or a pad depending on the experiment. The scintillation light is detected by a cryogenic photosensor (PMT or SiPM) and the time difference between the scintillation light detection and the arrival of ionized electrons on the anode enables the Z position to be determined. By placing a grid just below the anode, the ionized electrons leave a signal only when they are drifting between the grid and the anode. This enables a larger signal and a countermeasure to the pile-up of events at high rates.

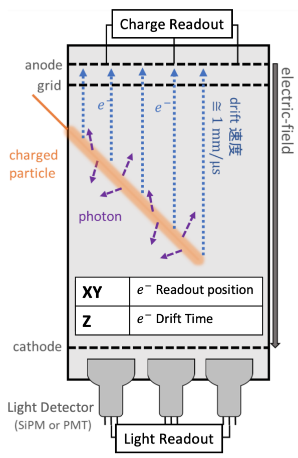

Figure 2.6: Schematic diagram of a LArTPC.

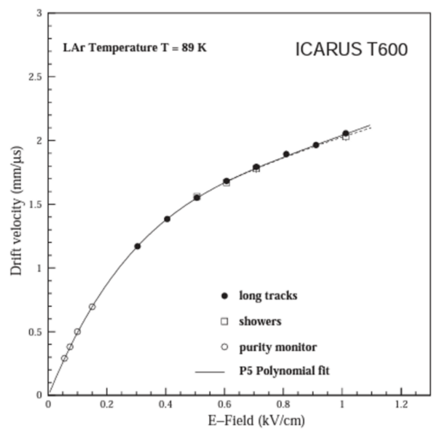

Figure 2.7: Relationship between electric field strength and electron drift velocity in liquid argon.

The drift velocity of the ionized electrons depends on the applied electric field strength as represented in Figure 2.7. The drift velocity could be calculated from the electric field strength E and temperature T with the following equation given by the ICARUS experiment [22]:

$$v_d\left(T, |E|\right) = \left(P_1\left(T - T + 0\right) + 1\right)\left(P_3\,|E|\ln\left(1 + \frac{P_4}{|E|}\right) + P_5\,|E|^{P_6}\right) + P_2\left(T - T_0\right) \quad (2.8)$$

The value of each parameter is shown in Table 2.2. Therefore, given a LArTPC of height 10 cm and an electric field of 200 V/cm, it would take around 100 μs for the electron to drift from the cathode to the anode.

Property	Value
P_1	$-0.01481 \pm 0.00095\ K^{-1}$
P_2	$-0.0075 \pm 0.0028\ K^{-1}$
P_3	$0.141 \pm 0.023\ \left(\frac{kV}{cm}\right)^{-1}$
P_4	$12.4 \pm 2.7\ \left(\frac{kV}{cm}\right)$
P_5	$1.627 \pm 0.078\ \left(\frac{kV}{cm}\right)^{-P_6}$
P_6	0.317 ± 0.021
T_0	$90.371\ K$

Table 2.2: Drift velocity equation parameter values.

2.3 GRAMS Detector

As mentioned in Section 1.4.2, in detecting low-energy antiparticles, the mass volume of the detector instrument must be reduced as much as possible for the low-energy antiparticles to reach the fiducial volume. The GAPS project aims to achieve this by utilizing an exotic atom technique instead of a magnet which will be described in detail in the next section. As the GAPS project utilizes a semiconductor layered detector, the energy resolution is very high but with a drawback of cost and hence the difficulty to scale its detector in size. Therefore, the GRAMS experiment is a next-generation experiment to GAPS which will utilize the same detection technique, but by using a LArTPC which is relatively easy to scale up in size due to the abundance and low cost of argon, higher sensitivities to antideuterons are expected.

The proposed detector design is shown in Figure 2.8. The LArTPC which acts as a calorimeter, particle tracker for cosmic rays, and Compton camera for gamma rays is surrounded by two layers of plastic scintillators that measure the velocity of incoming particles. Also, for gamma-ray observation, cosmic rays are background events and therefore could be vetoed by the ToFs.

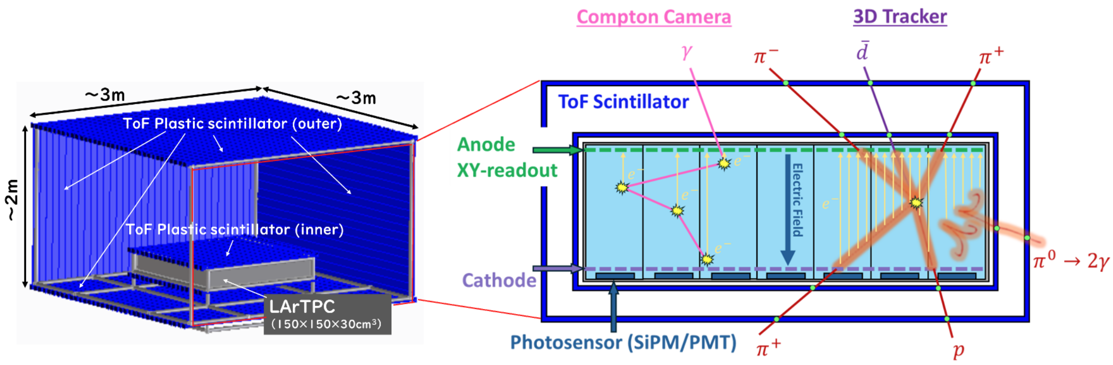

Figure 2.8: GRAMS detector concept design.

2.3.1 Particle Identification Technique

It can be seen from Figure 2.2 that to detect one antideuteron event, 10^4 antiproton events and 10^9 proton events must be rejected from the background (and all other particles). Therefore, a strong background rejection power is essential for antideuteron search. This section will describe the particle identification ability of a LArTPC.

Firstly, the GRAMS detector can obtain dE/dx from the charge signals in the LArTPC and velocity information from the ToFs. On top of that, to distinguish antideuterons from the background, the exotic atom technique mentioned briefly in previous sections is shown in detail in Figure 2.9 [23]. As the antideuteron enters the LArTPC, it deposits energy and stops to form an exotic atom with the Argon nucleus. As the atom de-excites, characteristic X-rays are released and the reaction ends in a nuclear annihilation producing multiple hadrons. The LArTPC can create tracks of the hadrons from the stopping point. For antiprotons and antideuterons with the same velocity, antideuterons will penetrate deeper into the LArTPC and release more energy per unit length (dE/dx). Furthermore, the average number of hadrons released from nuclear annihilation from antideuterons is more than antiprotons. From the points stated above, the LArTPC has a strong particle identification ability.

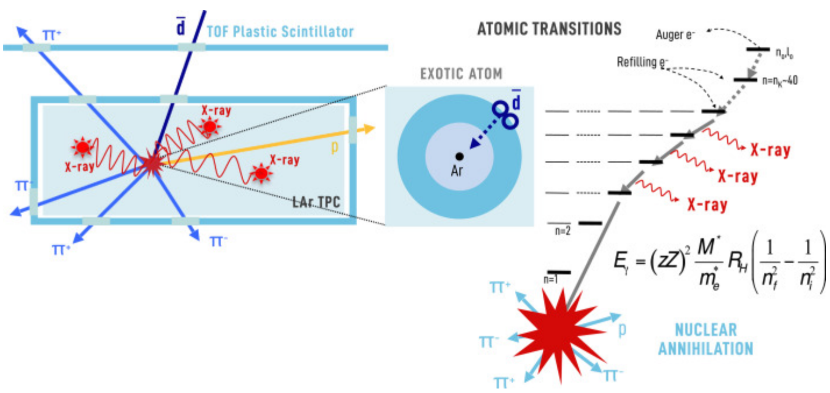

Figure 2.9: Exotic Atom Technique in LAr.

2.4 Antideuteron Single Event Sensitivity

As mentioned in the previous sections, the current upper limit on the antideuteron sensitivity is calculated by the BESS experiment at 6.7×10^{-5} $\mathrm{m^{-2}s^{-1}sr^{1}(GeV/n)^{-1}}$. The GRAMS experiment plans to conduct a long-duration (∼30days) balloon flight at the South Pole which is expected to improve the current upper limit by more than an order of magnitude.

To calculate the single event sensitivity to antideuterons, the GRAMS detector setup was implemented in Geant4 shown in Figure 5, antideuterons were generated uniformly from a sphere surrounding the detector and the ratio of events that ended with antideuterons being captured in the LArTPC was recorded for various energies.

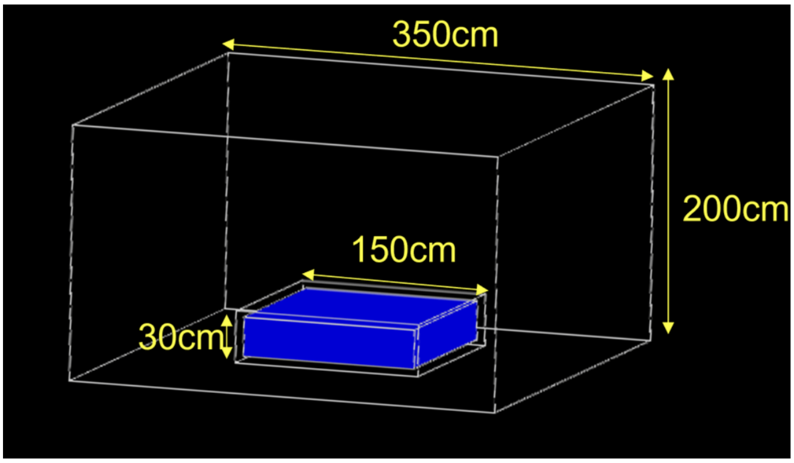

Figure 2.10: GRAMS detector setup in Geant4.

The calculation for the single event sensitivity is shown below:

$$Flux\ [\mathrm{m^{-2}s^{-1}sr^{-1}\,(GeV/n)^{-1}}] = \frac{N}{S[\mathrm{m^2}] \times T[\mathrm{s}] \times \Omega[\mathrm{sr}] \times E[\mathrm{GeV/n}]} \tag{2.9}$$

$$Sensitivity\ [\mathrm{m^{-2}s^{-1}sr^{-1}\,(GeV/n)^{-1}}] = \frac{Flux}{R \times \epsilon} \tag{2.10}$$

Here, S is the orthodrome area of the sphere on which antideuterons were generated, T is the expected time of the balloon flight, Ω is the solid angle, E is the energy, R is the ratio of captured events and ϵ is the particle ID efficiency of the LArTPC which is set to 1 (100% particle ID ability) for this calculation. As shown in Figure 2.11, the solid pink line represents the calculated sensitivity for the GRAMS detector operated for 30 days, improving the current upper limit by more than an order of magnitude. The dotted line shows the sensitivity for a 30 × 30 × 30 $\mathrm{cm^3}$ operated for 1 week. It can be seen that with a LArTPC with a size comparable to the GRAMS40 detector (explained in the next section), a sensitivity on par with the current best limit can be achieved.

The locations for conducting balloon experiments like GRAMS which search for low-energy cosmic rays, are crucial for maximizing data collection and improving sensitivity.

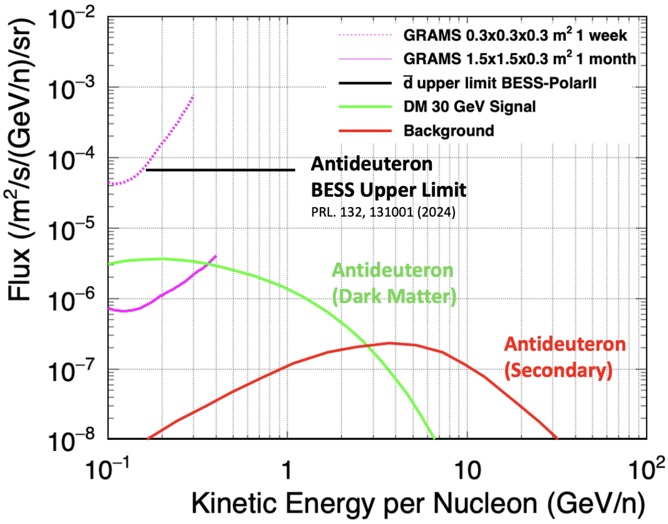

Figure 2.11: Calculated single event sensitivity compared to the antideuteron flux.

Figure 2.12 shows the flux of proton and helium at different altitudes and latitudes, calculated from the EXcel-based Program for calculating Atmospheric Cosmic-ray Spectrum (EXPACS) [24]. It can be seen that the flux is heavily dependent on the latitude and for helium, there is a strong cutoff at latitudes below 50° to 60° indicating the geomagnetic cutoff. Furthermore, the proton flux peaks at 30km but the helium flux increases gradually from 0 km to 60 km. This is due to the protons that are reflected or secondarily produced from lower altitudes. Therefore, when considering the altitude for balloon experiments, an altitude higher than 30 km is ideal (BESS-Polar II max altitude: 38km). Therefore, these factors make high altitudes at the South Pole an ideal location for long-duration balloon experiments aimed at indirect dark matter searches with low-energy cosmic antiparticles. In addition, the South Pole is particularly advantageous due to its prolonged periods of stable atmospheric conditions, allowing for extended balloon flights.

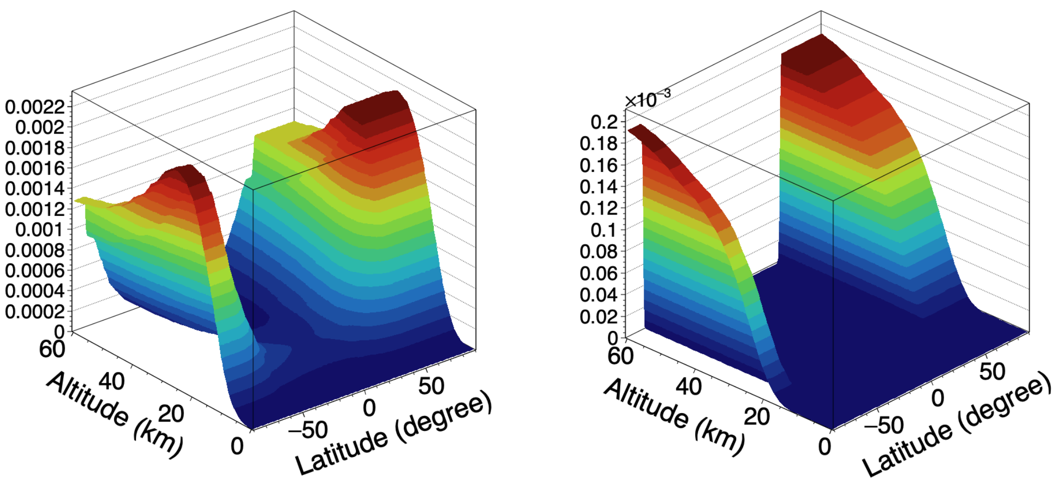

Figure 2.12: Calculated flux ($cm^{-2}s^{-1}$) of proton (left) and helium (right) for different latitudes and altitudes.

2.5 GRAMS Milestones

The target for the GRAMS experiment is to conduct a science balloon flight in Antarctica in the late 2020s and a satellite mission in the 2030s. Towards achieving this goal, three major milestones need to be accomplished.

- **Understanding Antiparticle Capture in LAr**

Although the exotic atom technique has been experimented with using an antiproton beam by the GAPS project, the exotic atom technique has never been observed in liquid argon. Therefore, for GRAMS it is essential to understand the reaction of antiparticles in LAr not only to confirm the validity of the exotic atom technique but also to feedback and improve simulation packages for antiparticle capture such as the ones found in Geant4.

- **Operating a LArTPC as a Compton Camera**

As GRAMS sets one of its goals as MeV gamma-ray observation, it is crucial to develop a LArTPC that is functional as a Compton camera, able to reconstruct gamma-ray Compton scattered events. To achieve this, the LArTPC and readout electronics must have high spatial resolution and energy resolution. Furthermore, the event reconstruction algorithms need to be developed.

- **Establishing LAr Handling System for Balloon Flights**

Although LArTPCs have been widely used for experiments on the ground, it has never been operated at balloon altitudes. Therefore, establishing a system that can handle LAr at balloon altitudes safely, with high reliability is also very important.

2.5.1 GRAMS40 Detector @ Waseda University

At Waseda University, as a first step to verifying the particle-antiparticle identification technique, a $30 \times 30 \times 30\ cm^3$ LArTPC (GRAMS40) was developed and operated [25]. As an operational check for this LArTPC, a cosmic muon test was conducted as described below.

The GRAMS40 LArTPC has a volume of $30 \times 30 \times 30\ cm^3$ which makes a liquid argon fiducial mass of 40 kg. The GRAMS40 detector is shown in Figure 2.13 and the anode pad design is shown in Figure 2.14. The GRAMS40 LArTPC consists of a cathode, grid, and anode. There are horizontal electrode pads on all 4 side plates (walls) which are connected at the corners of the TPC. Furthermore, a 100 MΩ resistor is placed between each electrode and thus induces a uniform electric field between the cathode and anode. On the inner side of the TPC walls, a reflective sheet (ESR) with TetraPhenyl Butadiene (TPB) deposited is placed to shift the scintillation light wavelength from 128 nm to 420 nm to be detected by a PMT. As shown in Figure 2.14, 5 mm anode pads are connected in a zig-zag fashion to create X and Y channel readouts. Therefore, the spatial resolution is 1 cm and the total readout channels are 60.

As primary cosmic rays collide with the Earth's atmosphere, showers of secondary particles are produced in which muons are included. Muons can have both charges μ^+ or

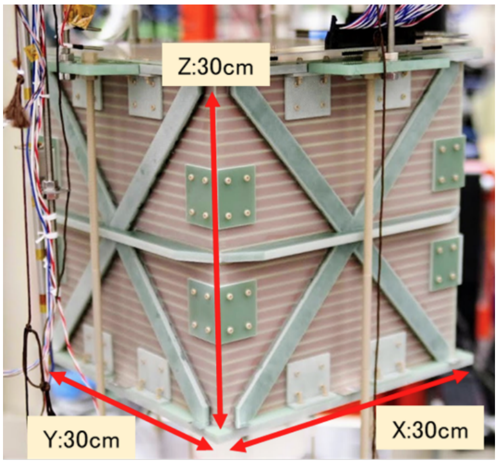

Figure 2.13: GRAMS40 LArTPC.

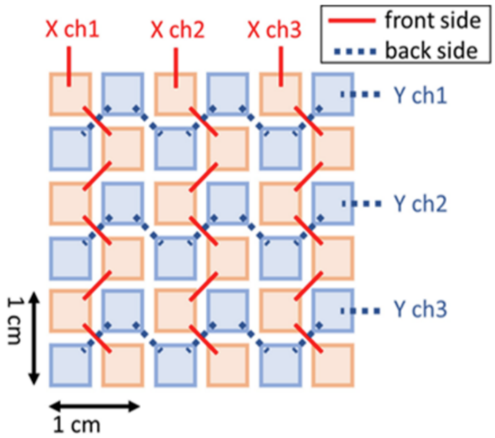

Figure 2.14: Anode Pad Configuration for GRAMS40.

μ^- and approximately one muon hits one cm^2 of the Earth's surface per minute. When a muon enters a LArTPC, it can either penetrate the TPC, decay, or get captured by the argon nucleus. Both μ^+ and μ^- can decay into a neutrino and a Michel electron but only μ^- can get captured as shown in the equations below:

- **Muon Decay**

$$\mu^+ \to \nu_e + \overline{\nu_\mu} + Michel\ e^+ \tag{2.11}$$
$$\mu^- \to \overline{\nu_e} + \nu_\mu + Michel\ e^- \tag{2.12}$$

- **Muon Capture**

$$\mu^- + p \to n + \nu_\mu \tag{2.13}$$

The decay and capture events can be distinguished by whether or not a muon emits a Michel electron after stopping. Reconstructing and observing the track of this Michel electron is synonymous with observing the track of emitted hadrons after an antiparticle nuclear capture event in the LArTPC, and is, therefore, an important step towards verifying this principle. In operating the GRAMS40 LArTPC, the charge signals were read out with an ADC onboarded readout board and triggered by the scintillation light signals detected by the PMT. A capture event and decay event obtained is shown in Figure 2.15, where the top event corresponds to a capture event and the bottom event corresponds to a decay event.

2.5.2 Purpose of this Study

The primary aim of this study is targeted towards the GRAMS milestone of establishing a LAr handling system for balloon flights. To achieve this milestone, an engineering balloon flight was conducted with a compact prototype LArTPC in collaboration with

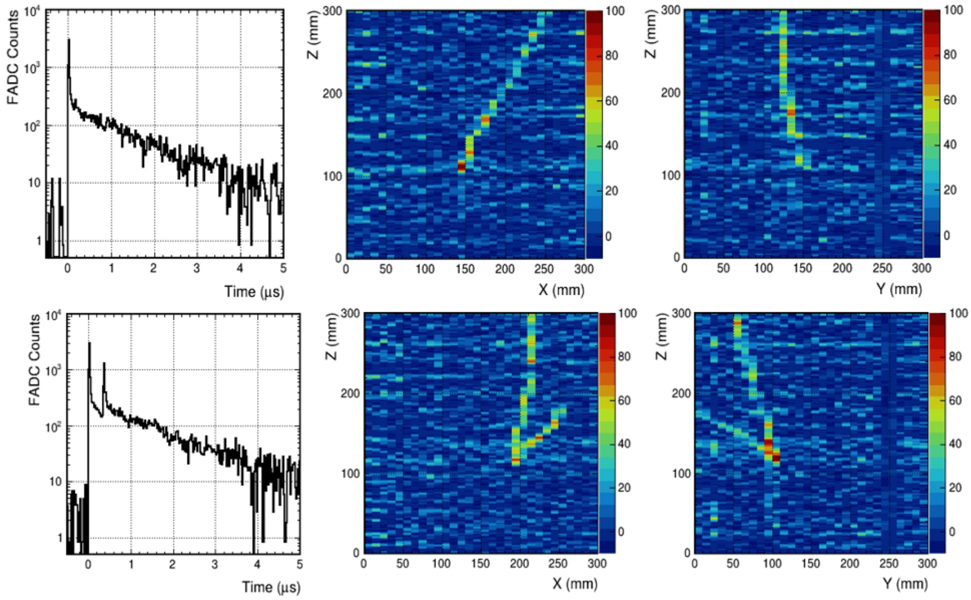

Figure 2.15: Muon capture and decay events in GRAMS40.

the Japan Aerospace Exploration Agency (JAXA). This engineering flight campaign was accepted as one of JAXA's balloon flights for the 2023 fiscal year and was labeled B23-06. The flight was successfully conducted on 27th July 2023. This thesis will delve into the details of the flight campaign, the LAr system used in the flight, and the results from the flight data as well as the LArTPC data. For this engineering flight, my main contribution was designing and constructing the LArTPC as well as the data analysis of the LArTPC data obtained during the flight. In Section 3 an overview of this engineering flight campaign will be described. The detector system as well as the LAr handling system will be explained in Section 4. Lastly, the results from the analysis of the prototype LArTPC will be given in Section 5.

3 B23-06 Flight Campaign

As stated above, it is essential to conduct a compact experiment to provide a basic proof-of-concept before a full-scale GRAMS experiment using a large LArTPC and a prototype pGRAMS experiment using a medium-sized liquid LArTPC (to be launched in Arizona in fall 2025 to spring 2026). As an initial step to tackle this milestone, an engineering flight was conducted to gain experience in conducting a balloon experiment as well as gain insight into the methods to operate LAr at balloon altitudes. This section will describe the balloon base held by JAXA which was used for the B23-06 flight. Furthermore, the success criteria for this flight and the flight conditions proposed will be explained. In addition, the challenges of operating a LArTPC at balloon altitudes will be discussed and the R&D timeline for this flight will be introduced.

3.1 JAXA/ISAS Domestic Flight Campaigns

Since 2008, the Japanese balloon base has been relocated from the Sanriku Balloon Center (SBC) to the Taiki Aerospace Research Field (TARF) located in Taiki, Hokkaido [26]. In 2008, two balloon flights were conducted to verify the performance of the newly built balloon operation system at TARF. Upon the successes of the two flights, balloon experiments which were selected annually by the JAXA/ISAS Scientific Balloon Program Advisory Committee have been conducted since 2009. The engineering flight for the GAPS experiment (pGAPS) was conducted at TARF in 2012 [13]. The application for the GRAMS engineering flight was made during the Scientific Balloon Symposium which took place on November 2022. In April of 2023, the GRAMS engineering flight was officially approved as one of the balloon flights for 2023, labeled B23-06.

A bird's-eye view of TARF is shown in Figure 3.1 and the area of TARF is shown in red. The hangar of sizes W30 m, H35 m, and L83 m is used to fill the balloons with helium, and a balloon with a total lift of 2500 kg is possible to be filled. After the balloon has been filled, the launcher that holds the gondola moves out to the handling area for launch as shown in Figure 3.2. The balloon operation building has radio telemetry systems used to communicate with the bus system on the gondola to control the balloon during the flight.

The flight season spans from May to September when the seasonal wind pattern is east wind in the upper stratosphere and strong west-wind jet streams as shown in Figure 3.3 [27]. However, due to recent climate changes, optimal wind conditions have become rarer. In recent years, the flight season has been getting shorter (July to September). As a countermeasure, piggyback experiments have been utilized which onboard the gondola used for the main experiment. For B23-06, there were two piggyback experiments: Morphing Experiment for DUrable Smart Antenna (MEDUSA) [28] and an experiment for High Precision Verification of General Relativity by Laser Frequency Comparison [29].

Regarding the flight path, as the balloon gets launched from TARF, it flies towards the sea (east direction) as it ascends. As the altitude increases, the wind direction changes and the balloon flies back towards TARF (west direction). The release of the gondola is

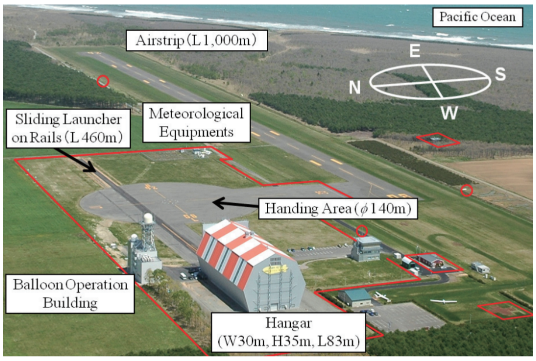

Figure 3.1: A bird's-eye view of TARF, area shown in red.

Figure 3.2: Sliding launcher holding the gondola for B23-06.

done above the sea and therefore the gondola and balloon are collected out at sea with a boat as shown in Figure 3.4 [26]. By releasing helium or ballast (weight), altitude control is possible and a "boomerang" style flight is conducted. A boomerang flight enables a longer duration flight and collection out at sea relatively close to the land (∼30 km).

The feasibility of a flight is determined from the results of the flight simulation conducted by the JAXA balloon group. The data used for the flight simulation are data from the Japan Meteorological Agency and the National Center of Environmental Prediction (NCEP). Upon conducting the simulation, the payload weight, maximum altitude, and the duration of the level flight are considered. The maximum altitude and duration of level flight is requested and proposed from the user side as mentioned in the next section. Therefore, to increase the chances of flight, the minimization of payload weight and request for low maximum altitude and no level flight is ideal. The users are given a notice a week in advance of a possible flight. The simulation is continuously conducted until the day of flight. In parallel, the user side has to finish the final preparation before the flight.

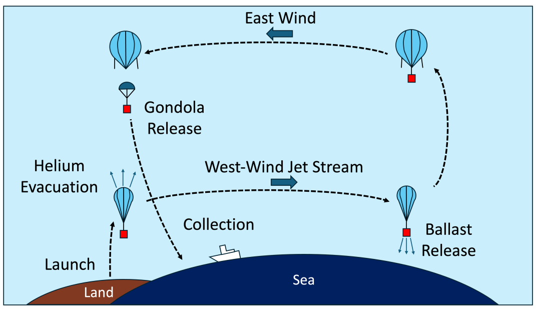

Figure 3.3: "Boomerang" flight trajectory from TARF.

Figure 3.4: Collection of gondola out at sea.

3.2 Success Criteria

As the motivation for this engineering flight was to establish a LAr handling system for balloon flights, the main objective was to maintain and control LAr by monitoring the pressure and temperature of LAr during the flight and designing a reliable system that can safely handle any emergencies (sudden changes in LAr environment) during the flight. Therefore, to accomplish this objective, high altitudes, and long level flight duration were not required.

For balloon flights held by JAXA, the success criteria are split into two stages: minimum success and full success. From the user side, the maximum altitude and level flight duration are requested for both minimum and full success. In conducting balloon flights with JAXA, the flight will be conducted if the wind conditions meet the requirements for the minimum success, and if the user is lucky enough that wind conditions can enable a flight to meet the full success criteria, the balloon will be operated as so. Therefore, the lighter the minimum success criteria, the higher the chances of flight.

For this engineering flight, the maximum altitude and level flight duration proposed for the success criteria are shown in Table 3.1. As shown in Table 3.1, a relatively low maximum altitude and no level flight was requested for the minimum success to increase the chances of flight. In addition, the minimum success was defined as maintaining and controlling LAr until the balloon reached 25 km during ascent. During the ascent, the LArTPC will be operated and data from the environmental sensors will be obtained to gain an understanding of the surrounding environment and how LAr operates under such conditions. On top of the minimum success, full success was defined as obtaining both gamma-ray and cosmic-ray data during a 10-minute flight at an altitude of 28 km.

	Maximum Altitude	Level Flight Duration
Minimum Success	≥ 25 km	≥ 0 min
Full Success	≥ 28 km	≥ 10 min

Table 3.1: Success Criteria Proposal.

3.3 Challenges to Operate a LArTPC at Balloon Altitudes

Although LArTPCs have been widely used in various experiments, it has never been operated above ground, let alone in a balloon experiment. From 1997 to 2000, several balloon campaigns were held for the Liquid Xenon Gamma-Ray Imaging Telescope (LXeGRIT) experiment [30]. Since then, no other experiment has operated a liquid noble gas TPCs at balloon altitudes.

There were various challenges unique to balloon experiments for operating a LArTPC. The main challenges are listed below:

- **Impact and vibrations:**
  The detector system contained in the cryostat is prone to vibrations and impacts from launching the balloon and opening the parachute. Furthermore, as the gondola is suspended from the balloon, the payload is prone to rotation.

- **Weight limitation:**
  The maximum weight of the payload depends on the balloon size and the amount of helium. In general, the lighter the balloon, the greater the chance of flight. Also, higher altitudes can be reached with smaller balloons with a smaller weight.

- **Power limitations:**
  Power is supplied by batteries or solar cells. Primary batteries were used for this engineering flight. A cooling system that can reduce the overall heat inflow requires a lot of power, hence no cooling system was used.

- **Changes in environment:**
  The atmospheric pressure changes from 1 atm to several Pa and the temperature changes from room temperature to -60°C as shown in Figure 3.5 [31]. Since the triple point pressure of Ar is 0.068 MPa, it will solidify if the pressure drops to the surrounding pressure. Furthermore, high-voltage discharges are more likely to occur at lower pressures.

- **Remote control of detectors:**
  Voltage control of photodetectors and TPC electric field, and DAQ settings have to be controlled from the ground. Temperature and pressure have to be monitored remotely as well.

- **Safe recovery:**
  The payload has to be recovered for environmental considerations and data collection. In the case of LAr, risk assessments for accessing the payload during recovery should be considered; for example, the cryostat may explode due to continuous evaporation of residual LAr increasing the internal pressure.

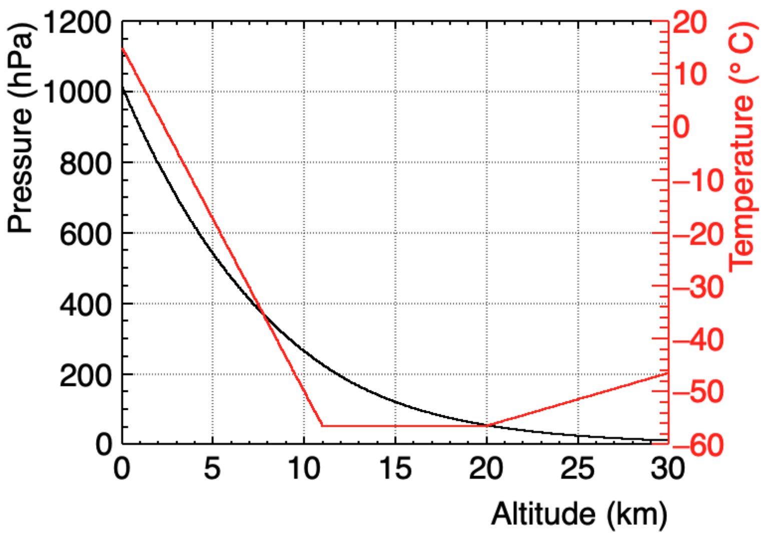

Figure 3.5: Pressure and temperature against altitude.

Other than the challenges listed above, there were various steps that needed to be overcome for a successful flight. The countermeasures to such problems and challenges will be discussed in Section 4.

3.4 Balloon System Overview

A schematic diagram showing the main components of the B23-06 balloon system provided by JAXA is shown in Figure 3.6. A polyethylene film-based balloon is connected to the parachute and gondola with a strong fiber rope. The balloon has an exhaust valve that can release helium to control the lift strength. Additionally, vent tubes are connected to the balloon to equalize the balloon pressure to the surrounding pressure. A cutter which can be activated remotely is used to detach the gondola from the balloon. The balloon size depends on the weight of the payload. For this engineering flight, the balloon used had a maximum capacity of 30000 m^2, 42 m in diameter. For reaching higher altitudes, larger balloons are used. A GPS tracker is installed in the balloon and the gondola to provide location during recovery at sea.

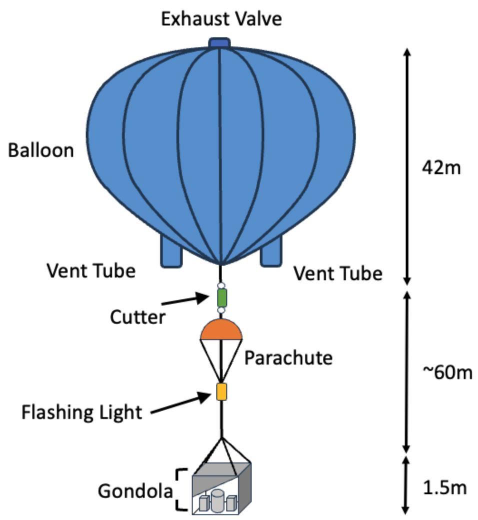

Figure 3.6: A schematic diagram of JAXA's balloon system.

For balloon experiments held by JAXA, the user side has to prepare the gondola which houses the scientific equipment and other components required for conducting a balloon experiment. For this flight, the cryostat containing the LArTPC detector was placed in the gondola with the other electronics. The weight of each component in the B23-06 flight system is shown in Table 3.2. Here, the weight of LAr used for the flight (around 15 kg) is not included.

	Component	Weight [kg]
Balloon	Balloon	152
System	Packing	49
Gondola	Gondola Frame	75
System	Ballast	158
GRAMS	Cryostat	71
System	Pressurized Vessel	31
Others	2 Piggyback experiments	107

Table 3.2: Weight of components in B23-06 flight system.

3.5 B23-06 Timeline

In this section, the schedule between the flight proposal and the launch will be briefly described. The details of the R&D and the results of various tests will be described in Section 4. The timeline of the flight will be described in Section 5.

3.5.1 Preparation Phase

This engineering flight was proposed to the JAXA/ISAS Scientific Balloon Program Advisory Committee through the Scientific Balloon Symposium which was conducted on November 7th, 2022. This engineering flight was officially accepted on April 20th, 2023. Therefore, from the date of the proposal to the launch, there were only 6 months of preparation and R&D.

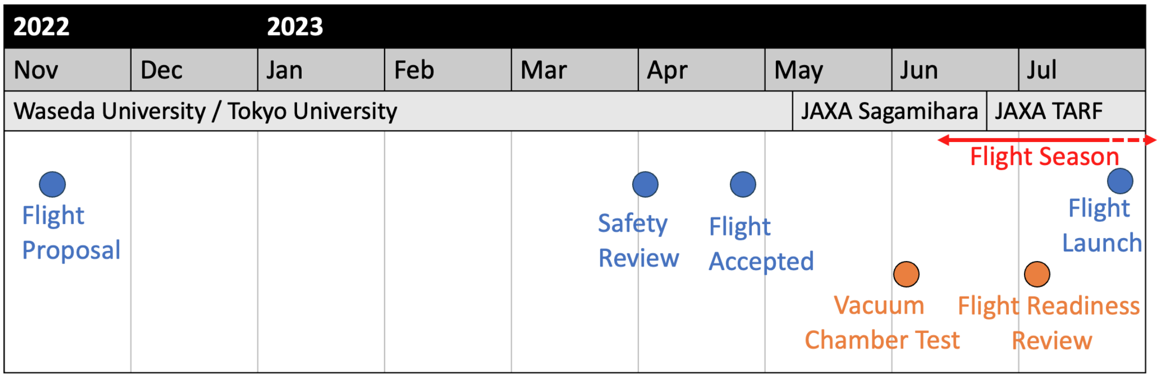

Figure 3.7: Timeline of the B23-06 flight campaign.

The timeline for this flight campaign is shown in Figure 3.7. The initial phase of the R&D which lasted until mid-May was conducted at Waseda University and Tokyo University. In this phase, mainly the hardware such as the gondola frame, cryostat, and the LArTPC was developed at Waseda Univ. and the electronics with the software were developed at Tokyo Univ. The main objective of the initial phase was to complete the detector setup within the cryostat and conduct an integration test between the cryostat & detector system developed at Waseda Univ. with the readout and housekeeping electronics developed at Tokyo Univ. Although the whole system was not finalized, a successful LAr test was completed.

From mid-May to mid-June, the flight setup was transported to JAXA's Sagamihara Campus. In this phase of preparation, the setup was finalized for the flight and an operation test with the vacuum thermostatic chamber was conducted. The photo of the vacuum thermostatic chamber used at JAXA Sagamihara Campus is shown in Figure 3.8. The vacuum thermostatic chamber was able to control the pressure and temperature enabling an environmental test for the flight setup. Additionally, the telemetry and command system was provided and integrated with the flight setup.

Figure 3.8: Vacuum chamber at JAXA Sagamihara Campus.

After clearing the vacuum thermostatic chamber test, the flight setup was transported to JAXA TARF on June 19th, 2023. The final steps at TARF were communication tests, final checkups, and establishing a standby state in which a flight was possible on any day. Communication tests were conducted to search for any noise sources within the gondola that may affect the telemetry and command communication lines. In addition, three final tests were conducted before the flight. These tests were conducted under conditions similar to those of actual operations. The first test was a ”Flight Readiness Review” (FRR), which was conducted as a final debugging process to determine if there were no problems and the balloon was ready for launch. If there are no problems in this test, the balloon will be ready to be released when the wind conditions allow for a flight. This test was conducted on July 5th and confirmed that there were no problems, but the actual release was scheduled for July 27th due to unfavorable weather conditions. Therefore, there was a standby period of about three weeks in which the flight system had to be constantly prepared for a flight in a few days. In this period, LAr ELF tanks were supplied periodically as sufficient LAr for flight had to be secured each day. Also, the cryostat was continuously vacuum-pumped until the previous day of launch to reduce outgas. A photo of the standby state of the gondola and the LAr ELF tank connected to the cryostat is shown in Figure 3.9. The second and third test was conducted on the previous day and the day of launch, respectively as shown in Figure 3.10.

Figure 3.9: Standby state when waiting for favorable wind conditions.

3.5.2 Flight Timeline

The timeline for the flight is shown in Figure 3.10. The second and third final tests (named Final Test 1 and 2 in Figure 3.10) were operation tests that used the same operation user manual as the flight. The checklist includes starting the DAQ, applying the high voltage to the LArTPC and opening the LAr evacuation valve through the telemetry and command, and so on. On the day before the flight at 8:00 am, LAr was filled into the cryostat. Then, the gondola was transported to the sliding launcher for the second operation test. Upon clearance, JAXA's balloon group went into the final preparation for the flight. Since the flight was planned for around 4:00 am on the next day, the LAr was monitored until the final operation test which was conducted at 2:00 am. As no problems were found during the final operation test, the sliding launcher that held the gondola moved out from the hangar to the launch area and helium was filled into the balloon.

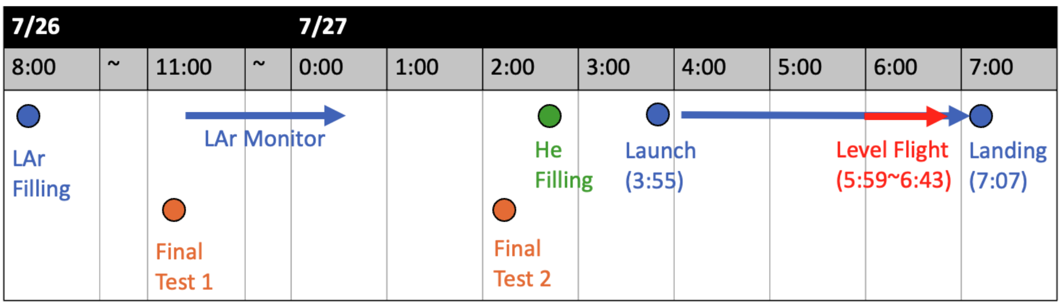

Figure 3.10: Flight timeline between LAr filling and Landing of the gondola at sea.

Regarding the flight, the balloon was launched at 3:55 am, released the gondola at 6:43 am, and landed at sea at 7:07 am resulting in a 3-hour and 12-minute flight. The maximum altitude reached was 28.9 km and 44 minutes of level flight (5:59 am to 6:43 am) was achieved. The plot showing the change in altitude over time is represented in Figure 3.11. As the wind direction changed at around 18 km, the flight trajectory represented in Figure 3.12 shows a boomerang flight trajectory. The gondola landed 30 km from the land and was successfully collected. Finally, the gondola was transported back to TARF for the collection of scientific equipment and flight data.

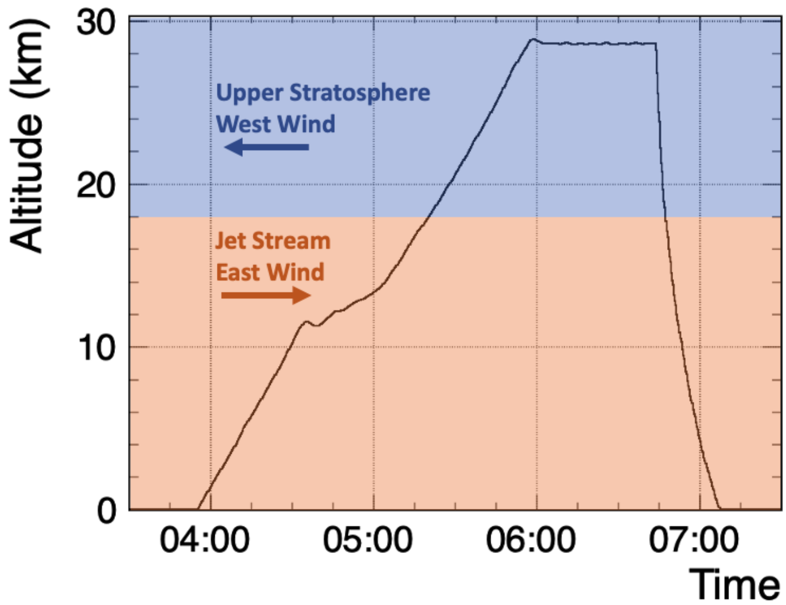

Figure 3.11: Altitude plot for flight B23-06.

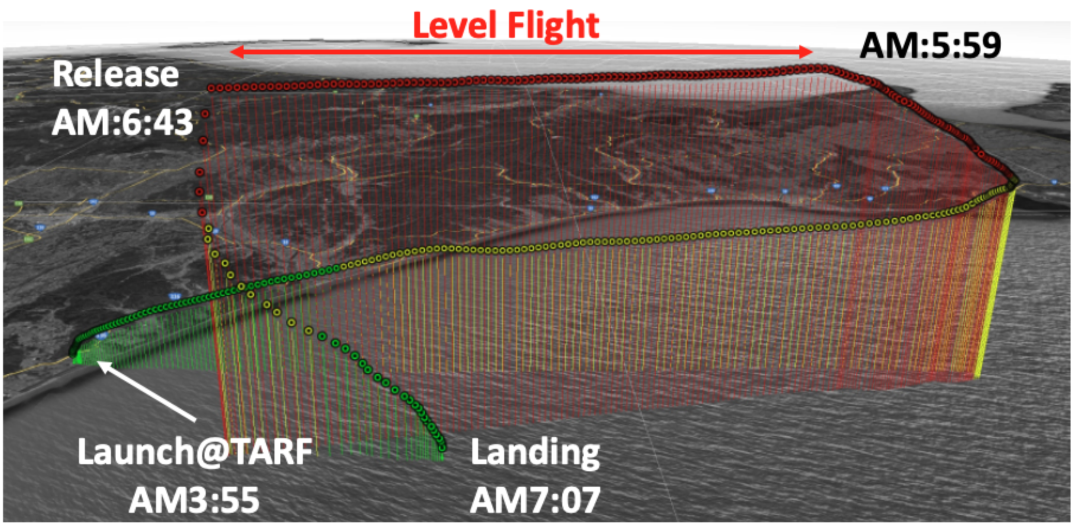

Figure 3.12: Flight trajectory for flight B23-06.

4 Payload

In this section, the details of the components in the payload will be addressed and the counter-measurements for the challenges mentioned in Section 3.3 will be described. The payload consisted of the cryostat containing the LArTPC, a pressurized vessel for the electronics, JAXA's bus system for communication, two ballast boxes, and two piggyback experiments. As shown in Figure 4.1, the cryostat was placed in the middle of the gondola, and the two ballast boxes were placed on the sides of the cryostat. This was to ensure that the heaviest components were placed near the center of the gondola.

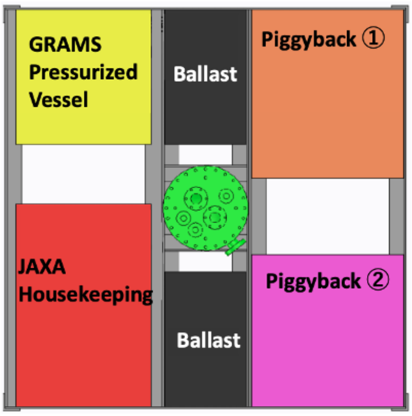

Figure 4.1: Bird's eye view layout of each component in the gondola.

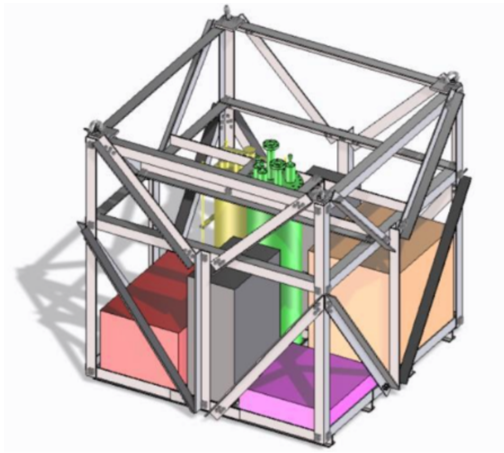

Figure 4.2: 3D CAD diagram of gondola.

The gondola was required to withstand 2G in horizontal (2 axes) and vertical directions for the impact during release and 5G in the vertical direction for the impact during parachuting. The gondola frame consisted of L-shaped steel (A6065-t5, $50 \times 50 \times$ t5 mm) and H-shaped steel (A6065-t5, $50 \times 50 \times$ t4 $\times$ t3 mm). The overall size is a cube of $1.2 \times 1.2 \times 1.2$ m. The frames are fastened to each other with stainless screws. Stainless steel eye nuts were used at the suspension points, and extra-strong duralumin (A7075) was installed at the eye nut fixing points.

The gondola was wrapped with Styrofoam on all sides for three major reasons: heat insulation, buoyancy, and visibility. As the atmospheric temperature drops to around -60°C, drastic temperature changes in the gondola need to be reduced. In terms of buoyancy, as the collection of the gondola will be out at sea, the Styrofoam was used as a float. To prevent the gondola from tipping upside down after landing at sea, Styrofoam was installed in the top half of the gondola as shown in Figure 4.3. Lastly, the Styrofoam was painted in white and orange to improve visibility as shown in Figure 4.4.

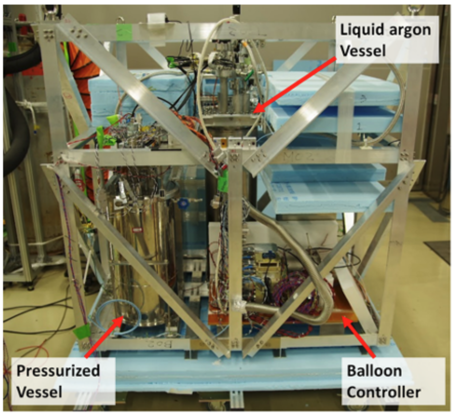

Figure 4.3: Photo of the cryostat and pressurized vessel in the gondola.

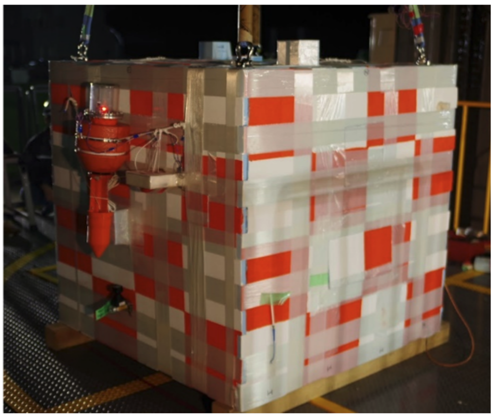

Figure 4.4: Gondola with painted Styrofoam on all sides.

4.1 Cryostat

To maintain argon as a liquid, it was required to keep the inner pressure of the cryostat at around 1 atm and a temperature of -186°C despite the changes in the surrounding environment. Therefore in designing the cryostat, the heat inflow had to be minimized and vibrations during launch and mid-flight had to be accounted for.

The designed cryostat is an open-bath type vacuum-insulated container with a top flange, made with stainless steel shown in Figure 4.5. The blueprint of the cryostat and the top flange is given in the Appendix as Figure A.1 and Figure A.2, respectively. The cryostat was 800 mm in height and 250 mm in width resulting in a maximum capacity of 22 L. The top flange had two ICF70 ports, where each port was used for LAr handling mentioned in the next section and another port was used for the LArTPC signals and high voltages. Also, the top flange had three VCR ports. Each VCR port was used for GAr release, LAr filling, and LAr evacuation.

To minimize the heat inflow, the cryostat had a 17 mm thick vacuum-insulated outer layer with super-insulation sheets installed on the inner layer side. To calculate the heat inflow of this cryostat, the liquid level was monitored during an LAr run as shown in 4.6. In this LAr run, the top flange was closed and the LArTPC was installed in the cryostat. The liquid level plot was fitted with a 1st-order polynomial function to obtain the gradient. The fit shows that the liquid level decreased by 0.75 cm/hour (0.0002 cm/s). This equates to a gas argon production of ≈ 180 L/hour (3 L/min). In order to calculate the heat inflow, the following equations were used:

$$M = \pi r^2 h\rho = \pi \times 10^2 \times 0.0002 \times 1.39 = 0.0278\pi \ g/s \tag{4.1}$$

$$Q = M \times L = 0.0278\pi \times 161 \approx 14 \ W \tag{4.2}$$

Here, M represents the mass loss per second, h represents the liquid level drop rate in cm/s, Q is the heat inflow in watts, and L is the latent heat of evaporation for liquid

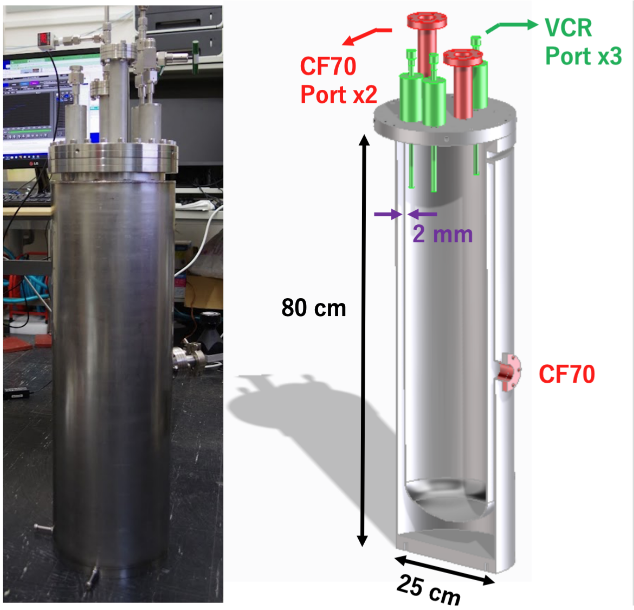

Figure 4.5: Photo of the cryostat and 3D CAD showing the cross-section.

argon.

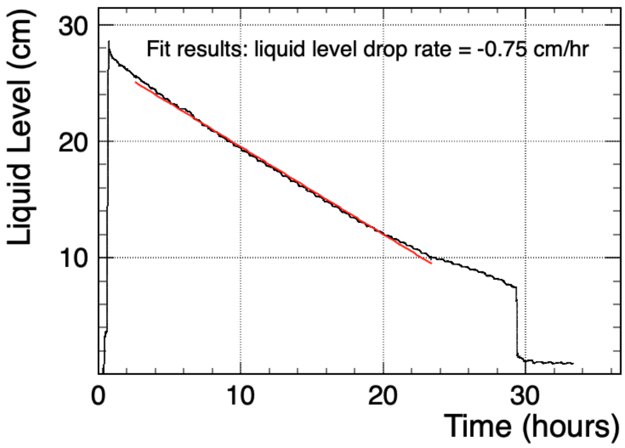

Figure 4.6: Liquid level drop rate against time for LAr.

As 2G of force is expected during launch and the gondola is prone to vibrations during the flight, LAr is expected to move inside the cryostat. Therefore, to minimize the risk of LAr touching the top flange and causing a sudden increase in internal pressure, the cryostat was designed to be thin and tall. Furthermore, a pin attachment is placed between the inner and outer walls to prevent the vacuum-insulated layer from breaking. The cryostat was designed to withstand a pressure of 7 atm. A pressure test up to an internal pressure of 4 atm was conducted using GAr. Figure 4.7 shows the result of the pressure test for the cryostat. A differential pressure of 3 atm (absolute pressure = 4 atm) was maintained for more than 10 minutes during the pressure test.

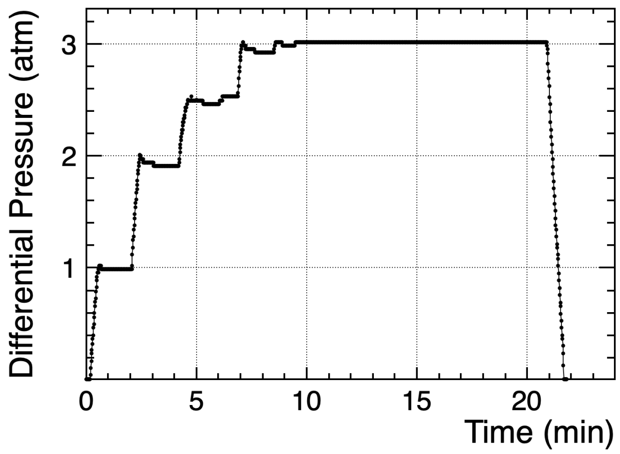

Figure 4.7: Internal pressure during pressure test.

4.2 LAr Handling System

In handling LAr for the flight, there were three main steps: filling, maintaining, and evacuation. Before setting the payload to the sliding launcher, high-purity LAr had to be filled to the cryostat. After launch, the LAr had to be controlled and maintained during the whole flight. Upon parachuting, the LAr had to be evacuated as any residual LAr during recovery of the payload, increases the risk for the recovery crew members. The setup that connects the LAr ELF tank to the cryostat is shown in Figure 4.8. The LAr ELF tank is connected to the LAr ELF tank with a LAr filter in between. This setup is the same as the photo shown in Figure 3.9 where the components surrounded in the blue dashed line can be detached from the cryostat and therefore left on the ground. Whereas, the components in the red dashed lines are in the gondola and used for flight.

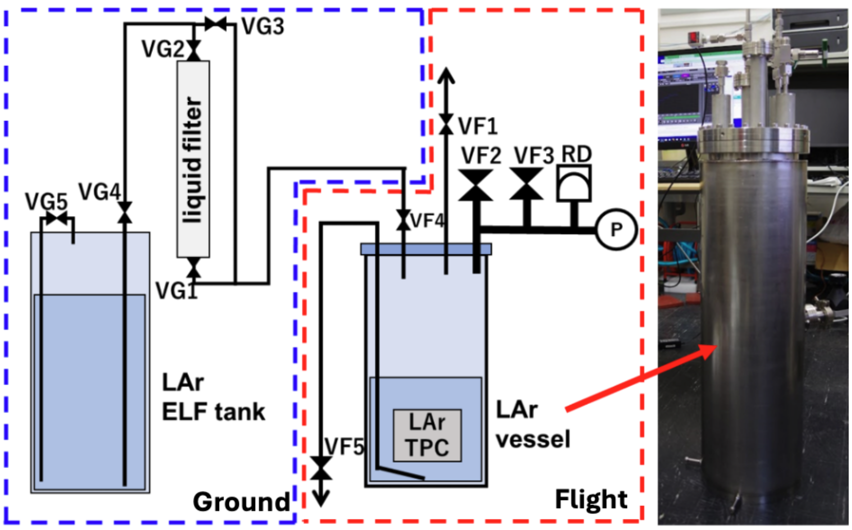

Figure 4.8: Schematic diagram showing the LAr ELF tank connected to the cryostat.

4.2.1 Filling LAr

In filling liquid argon, electronegative impurities need to be filtered out. Hence, a LAr filter with reduced copper R3-11G (to remove oxygen) and molecular sieve 4A (to remove water) was used [32]. Also, during the standby phase, the cryostat was vacuum pumped through the manual valve VF3, to reduce outgassing as much as possible. Furthermore, as shown in the flight timeline represented by Figure 3.10, there were 20 hours from filling LAr into the cryostat to the launch. Therefore, sufficient LAr needed to be filled for the liquid level to be above the LArTPC before and during the flight. From Figure 4.6, it can be seen that the liquid level drop rate was 0.75 cm/hr which meant that 20 hours would equate to a 15 cm decrease in liquid level. In addition, for a few hours of flight, a few cm of LAr was expected to evaporate. Upon filling, a liquid meter was used to monitor how much LAr was filled in the cryostat. LAr was filled until there was 22 cm of LAr above the LArTPC. This meant that there was about 7 cm of LAr above the LArTPC during launch and sufficient for the whole flight.

4.2.2 LAr control and monitoring

To maintain argon as a liquid, it was required to keep the inner pressure of the cryostat at around 1 atm and a temperature of -186°C despite the changes in the surrounding environment. Since no refrigerator was used for this flight, LAr was continuously being evaporated from the heat inflow and GAr was produced. Therefore, an absolute pressure valve which opens at 1.2 atm with a maximum flow rate of 20 L/min (VF1 in Figures), manufactured by TAVCO (product number:2391243.2.9) was used to keep the inner pressure constant. As mentioned in the previous section, at normal operating conditions, the GAr flow rate is 3 L/min and therefore the absolute pressure valve is sufficient for maintaining the inner pressure. However, for safety measures when there is a sudden increase in LAr evaporation, a differential pressure valve that opens at 1.5 atm with a maximum flow rate of 600 L/min (VF2 in Figures), manufactured by Venn Corporation (product number: SL-39) was used. In addition, for emergency purposes, a rupture disk which breaks at 2.0 atm (RD in Figures), manufactured by V TEX Corp. was installed.

An absolute pressure gauge manufactured by Nagano Keiki (product number: KP15) was used to monitor the cryostat pressure. In this system, the absolute pressure valve was at the end of a flex hose connected to one of the VCR ports. The differential pressure valve, the rupture disk, and the pressure gauge were connected to one of the ICF70 ports. The bird's eye view of the top flange showing the different valves are shown in Figure 4.9. In monitoring the temperature of LAr during the flight, three RTD temperature sensors were installed in the cryostat. The positions of the three sensors were: 25 cm above the LArTPC, just above the LArTPC, and at the bottom of the cryostat as shown in Figure 4.10.

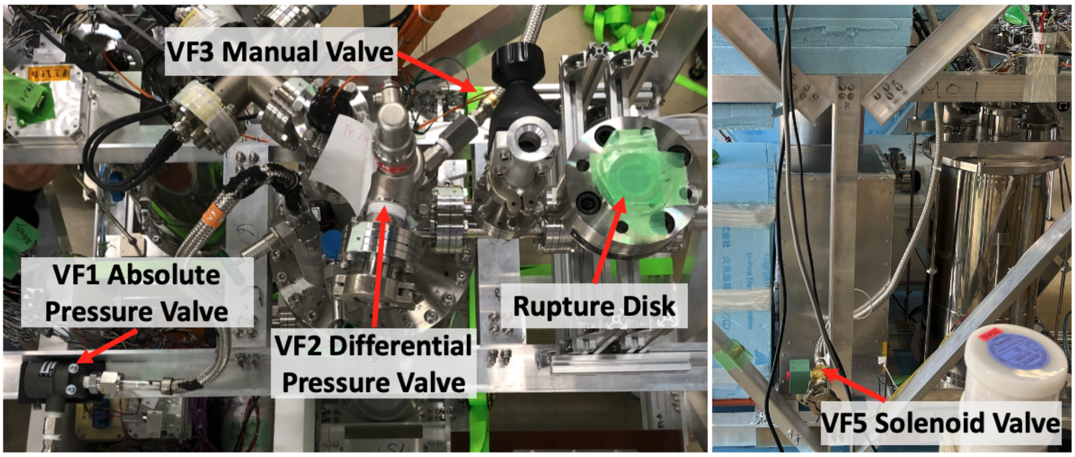

Figure 4.9: (left) Bird's eye view of the top flange with the different valves. (right) Solenoid valve used for LAr evacuation.

4.2.3 LAr evacuation

During the descent of the balloon, the LAr had to be evacuated from the cryostat for safety measures. The evacuation of LAr was done using a stainless steel pipe that extended from the VCR port inside the cryostat to the bottom of the cryostat as shown in Figure 4.10. On the outside, the VCR port had a flex hose connected with a solenoid valve connected to its end as shown on the right side of Figure 4.9. The solenoid valve represented as VF5 in the above Figures, manufactured by Nihon ASCO Ltd. (product number: J263G210LT) opens with a 24 V DC input. When the gondola is at balloon altitudes, the surrounding pressure is almost a vacuum and the inner pressure of the cryostat is 1.2 atm. Therefore, by the difference of pressure, as the solenoid valve opens, the LAr should be evacuated. However, as shown in Figure 2.3, below 0.7 atm, the liquid phase does not exist. Subsequently, the LAr is expected to solidify at the exit of the solenoid valve and become a liquid when the altitude drops and the surrounding pressure becomes larger than 0.7 atm. When the evacuation is complete, the internal pressure would become equal to the external atmospheric pressure.

4.3 Detector System

The detector system for flight B23-06 consisted of a 3ch output, 10 cm x 10 cm x 10 cm LArTPC for charge readout, and a Photomultiplier tube (PMT) for light readout. A charge-sensitive preamplifier (made by the GRAMS group at Northeastern University) was connected to the anode of the LArTPC for amplifying the charge signals. The full setup is shown in Figure 4.10. The amp box contains the preamplifiers for the charge readout from the anode. The PMT is fixed between two cross-shaped baffle plates which are installed for vibration measures. The DAQ for the LArTPC signals and the PMT signals are described in detail in Section 4.4.

Four stainless steel rods connected a circular plate with eight M8 holes to the top

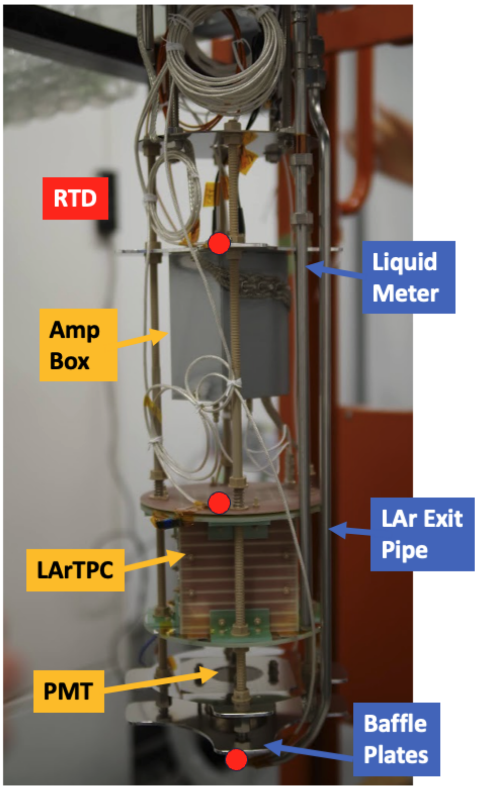

Figure 4.10: Final detector setup inside the cryostat.

flange which had four M8 bolt holes at r=130 mm as shown in Figure A.2. The other four holes on the circular plate were used for the PEEK rods which extend down to the baffle plate holding the PMT.

4.3.1 Charge Readout

The LArTPC used for this flight was a downgraded version of the GRAMS40 LArTPC in terms of size and readout channels. As the main objective of this flight was to establish a LAr handling system for balloon altitudes, the LArTPC was designed to be as simple as possible. However, the design concept is the same as the GRAMS40 LArTPC where there are components for inducing a uniform electric field (Cathode, Side Plates & Grid) and an anode for reading ionized electron signals as shown in Figure 4.11.

The anode, anode grid reinforcement, side plates, and cathode grid reinforcement parts were made of 1.6 mm thick FR4 material. The electrodes on the anode and side plates were 0.035 μm thick. The TPC reinforcement parts were made of glass epoxy and used to connect the side plates to the grid reinforcement parts. The four holes on the anode and other components are used to pass the PEEK rod through.

- **Electric Field Shaping**

For ionized electrons to drift vertically toward the anode, a uniform electric field is required. For this LArTPC, a high voltage was applied to the cathode, and by dividing

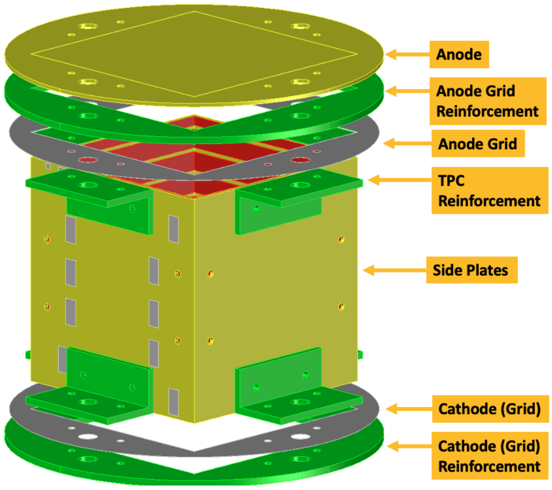

Figure 4.11: Components in the LArTPC.

the voltage vertically throughout the TPC using resistors, a uniform electric field was created. The front and back layers of the side plates used are shown in Figure 4.12 and Figure 4.13, respectively. Each side plate is 98.4 mm in thickness and 100 mm in height. Horizontal electrodes of height 8 mm are vertically aligned and are soldered at the corners of the electrodes on the other side plates. The top and bottom electrodes are electrically connected to the grids through a wire and 100 MΩ resistors are placed in between each electrode on one side plate. Since there are ten 100 MΩ resistors, the total resistance on the side plate is 1 GΩ.

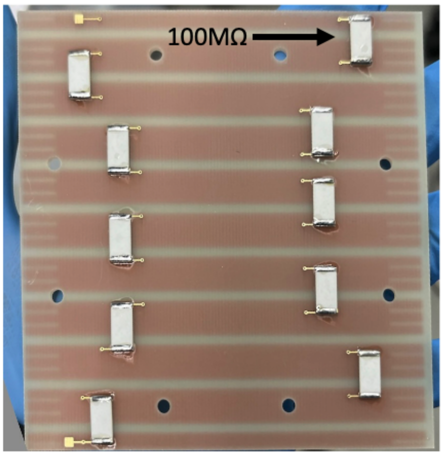

Figure 4.12: Side plate front side.

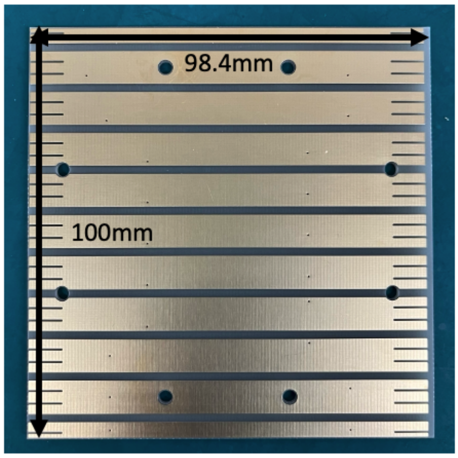

Figure 4.13: Side plate back side.

The stainless steel mesh used for the cathode and the anode grid is shown in Figure 4.14 and the reinforcement part for the grid is shown in Figure 4.15. The grid is a 0.1 mm thick, 5 mm pitch, 0.1 mm width stainless steel mesh. The grid had a diameter of 160 mm and the grid area was 100 mm x 100 mm. To support this thin grid, the reinforcement part was used. The diameter of the reinforcement part is 164 mm, 4 mm wider than the grid. This prevents the stainless steel grids, which have a voltage potential due to the high voltage applied, from touching the cryostat wall in case of violent vibrations.

A 250 MΩ resistor is placed between the anode grid and the anode. For this flight, -2500 V was applied to the cathode. Therefore, the electric field between the cathode and anode grid was 200 V/cm and 500 V/cm between the anode grid and the anode.

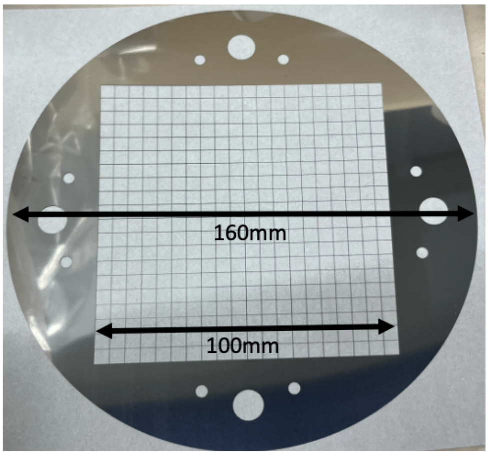

Figure 4.14: Stainless steel meshed grid.

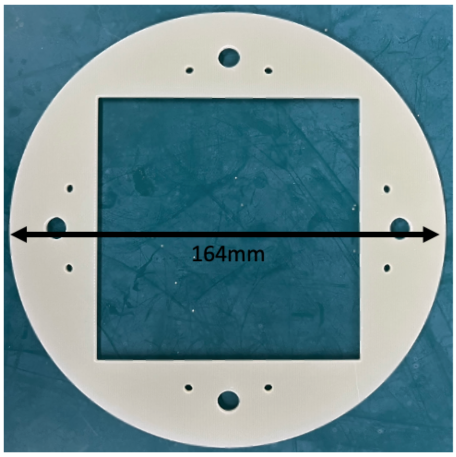

Figure 4.15: Grid reinforcement part.

- **Signal Readout**

The electrodes on the anode are used to detect the ionized electrons. Both sides of the 3ch anode are shown in Figure 4.16 and Figure 4.17. The anode pad consists of a 42 mm square pad (ch3) which is surrounded by two layers of square-shaped pads of 66 mm and 90 mm. From electric field simulations using FEMTET, the electric field was distorted in a wave-like structure near the walls of the side plate. Therefore, the outermost channel was designed to be 90 mm in width/height instead of 100 mm. A solid ground surrounds the outermost channel (ch1) to reduce noise. Each pad is connected to a wire on the front side of the anode, which connects to a LEMO receptacle.

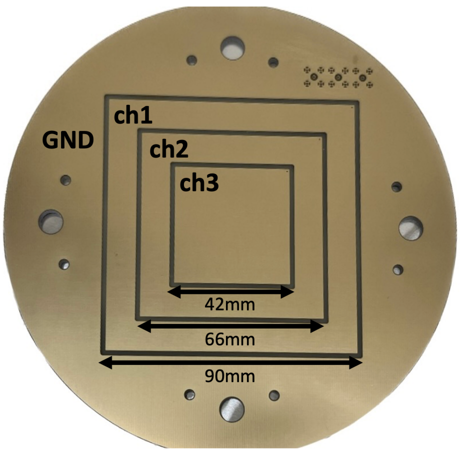

Figure 4.16: Back side of Anode.

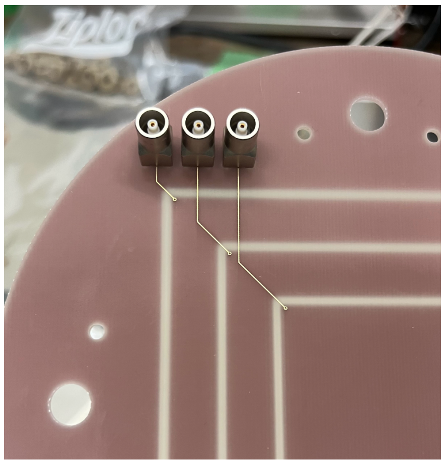

Figure 4.17: Front side of Anode.

Each of the 3 channels on the anode is connected to a charge preamplifier located in the amp box. Each charge preamplifier operates with an input voltage of ± 5 V. Figure 4.18 shows three charge preamplifiers wired aerially in the amp box. The feedback resistor was 1 GΩ and the feedback capacitor was 0.5 pF, therefore, the gain was 2 V/pC with a decay constant of 500 μs.

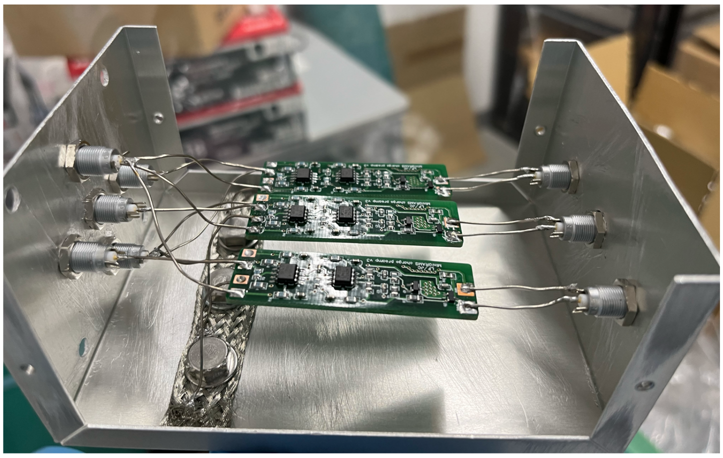

Figure 4.18: 3 charge preamplifiers in the amp box.

For simplicity, consider a LArTPC with a single channel anode and 100% pure LAr. When a charged particle enters the TPC, ionized electrons are produced and drift towards the anode as shown in Figure 4.19. A current is induced at the anode due to the drift of ionized electrons as shown in Figure 4.20. The value of the current is the total charge divided by the total drift time of the electrons (t_0 to t_1).

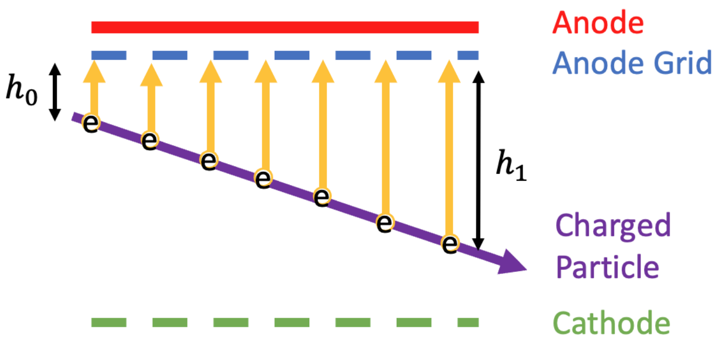

Figure 4.19: Charged Particle penetrating a 1ch LArTPC.

The signal output shown in Figure 4.21 is the convolution between the current and the charge preamplifier response function. The signal output function between t_0 and t_1 is shown in the equation below:

$$V_{out}(t) = I(t) * h(t) = \frac{Q}{t_1 - t_0} * Gain \times e^{-\frac{t-t_0}{\tau_{amp}}} = \frac{Q \times Gain \times \tau_{amp}}{t_1 - t_0} \left(1 - e^{-\frac{t-t_0}{\tau_{amp}}}\right) \quad (4.3)$$

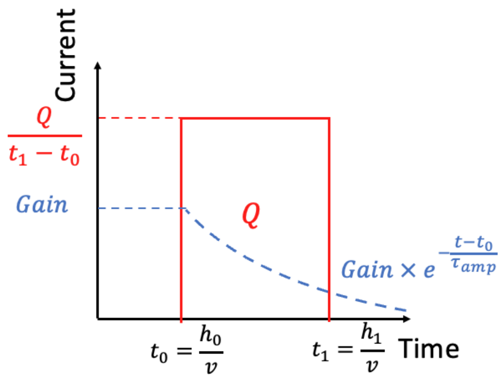

Figure 4.20: Charge signal.

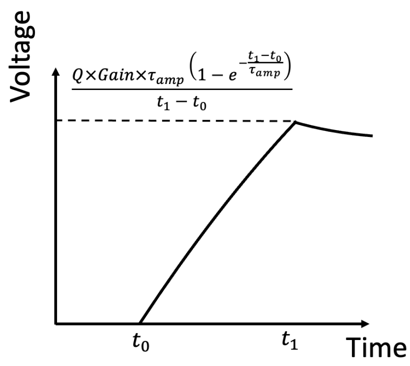

Figure 4.21: Output signal.

Here, $I(t)$ is the induced current at the anode, $h(t)$ is the charge preamplifier response function, Q is the total charge of the ionized electrons, t_0 and t_1 are the start and end of the drift time, $Gain$ is the charge preamplifier gain and τ_{amp} is the decay constant of the charge preamplifier. After t_1, the signal decays over time with the decay constant of the charge preamplifier.

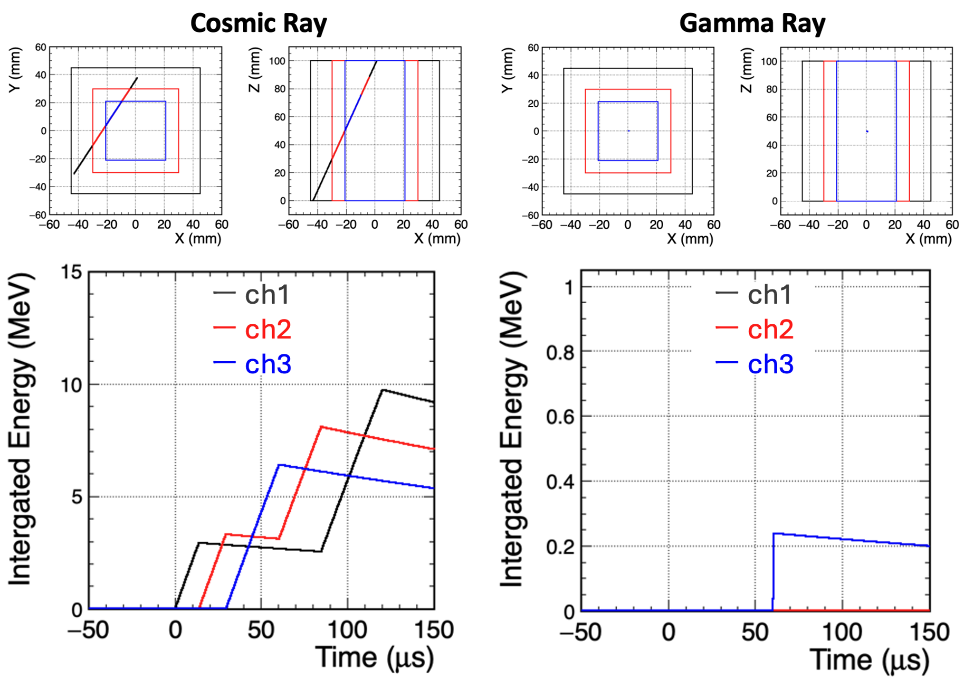

Figure 4.22: Simulated signal output for the 3ch LArTPC. (left) Cosmic ray penetration. (right) gamma ray Compton scattering.

The simulated events for the 3ch LArTPC are shown in Figure 4.22. For the cosmic ray, the trajectory of the track is shown in the top two plots. For this simulated event, the cosmic ray penetrates through the TPC, hence there will be two signals on ch1 and ch2 and one signal on ch3. The time at which the signals on each channel start to rise represents the z position of the electron. For the gamma-ray event, the Compton scattered event is a point-like event where the signal is only present in the channel where the Compton scattering occurred below the channel pad.

4.3.2 Light Readout

For detecting the scintillation light, a PMT manufactured by Hamamatsu Photonics was used (R6041-506) shown in Figure 4.23. The PMT was operated at 700 V with a gain of 2×10^5. The spectral response range is between 160 nm and 650 nm. Since the LAr scintillation light spectrum peaks at 420 nm, the wavelength had to be shifted to be detected by this PMT. Thus, TetraPhenyl Butadiene (TPB) was deposited on the PMT window. Furthermore, Enhanced Specular Reflector Films (ESR) with TPB deposited on the surface were placed on the side plates of the LArTPC as shown in Figure 4.24. The output of the PMT was used as a trigger in the DAQ system.

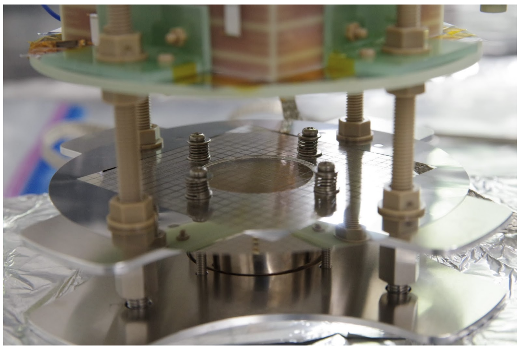

Figure 4.23: PMT fixed between the baffle plates.

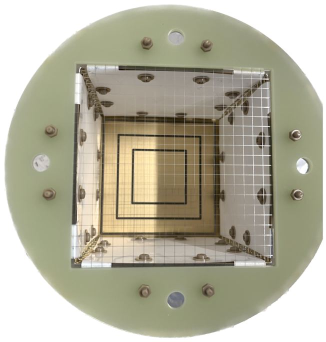

Figure 4.24: Photo of the LArTPC from below.

4.4 Pressurized Vessel

One of the technical challenges for this flight was developing the electronics required for controlling LAr and operating the LArTPC under the limited power supply, weight constraints, and under balloon altitude environments. As a countermeasure to the decrease in temperature and pressure shown in Figure 3.5, a vessel with high air-tightness was used to contain all the electronics required for the flight.

The pressurized vessel used was the 20 L vessel of the PCN-F series manufactured by MONOVATE Co. with some customization in the top flange and the inner structure. The components inside of the vessel are shown in Figure 4.25. The pressurized vessel was 530 mm in height and 260 mm in width. The top flange had an R3/8 hole, four NW40 ports, and tapped holes on the inner side to fix the pillars of the structure holding the electronics. The usage of each port on the top flange is summarized in Table 4.1 The blueprint of the pressurized vessel is shown in Figure A.3.

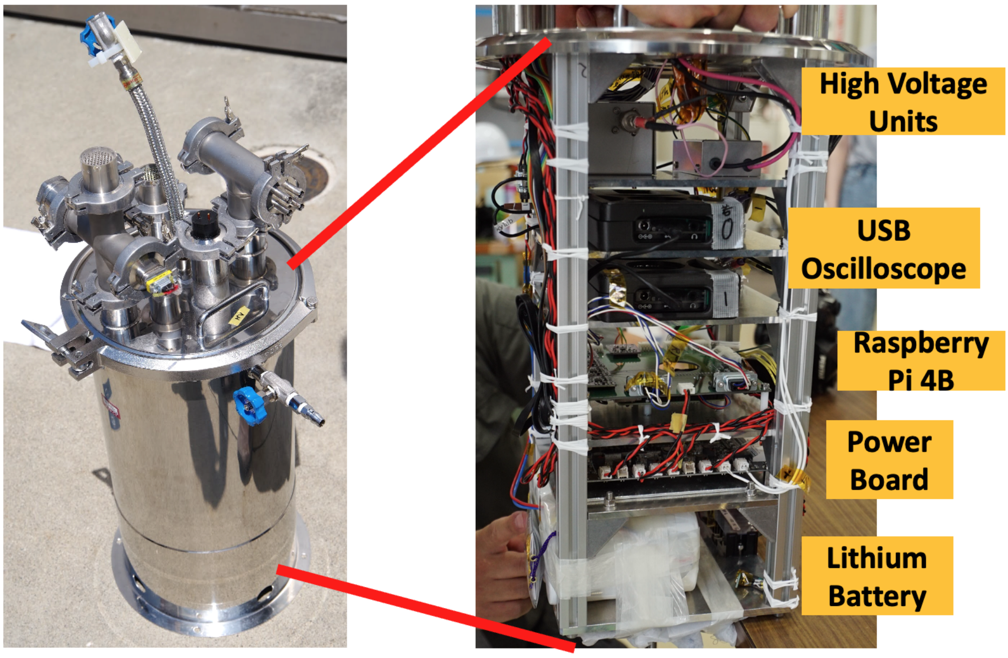

Figure 4.25: Pressurized vessel containing electronics.

	Feedthrough	Role
NW40 1	4ch BNC 1	PMT & LArTPC Signal
	4ch BNC 2	Charge Preamp Power
NW40 2	LAN	PC Connection
	D-sub	Main Power Supply
	48-pin	Slow Control
NW40 3	48-pin	Telemetry and Command
NW40 4	Custom Blank Flange	High Voltage

Table 4.1: Role of each port on the top flange of the pressurized vessel.

The components included are (from the top), the high voltage modules for the PMT and LArTPC cathode, two USB oscilloscopes for reading the PMT and LArTPC waveforms, Raspberry Pi model 4B as the PC, a power divider board to distribute the power from the battery placed at the bottom.

As mentioned in Section 3.5.2, a vacuum thermostatic chamber was used to place the payload under balloon conditions and test if the electronics were operable. In this test, a prototype Styrofoam wall was placed on each side of the gondola. The cryostat, pressurized vessel, and JAXA's bus system for telemetry and command communication were installed. Figure 4.26 shows the gondola installed into the vacuum thermostatic chamber.

For this test, the temperature was changed from room temperature to -50°C and the pressure was reduced to 10 hPa. There were six temperature monitors of which three temperature sensors were evenly placed vertically inside the pressurized vessel. The other

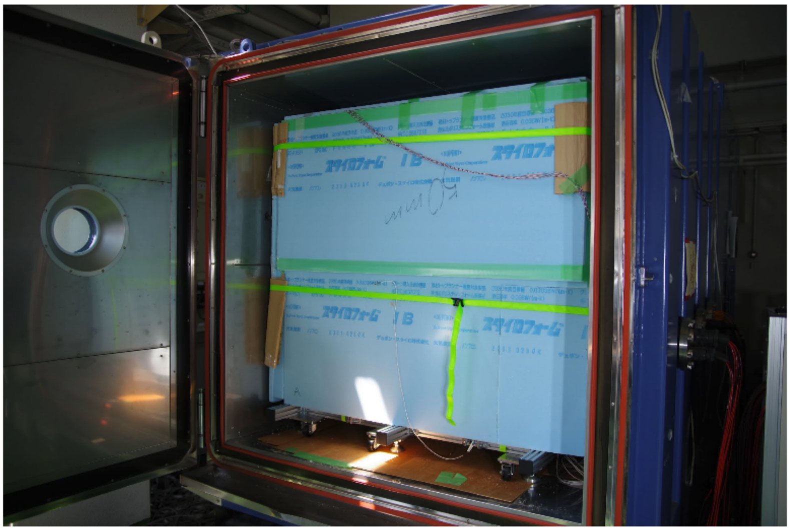

Figure 4.26: Gondola placed inside the vacuum thermostatic chamber.

three temperature sensors were placed on the top flange of the pressurized vessel, on the base of the pressurized vessel, and the gondola frame. The results are shown in Figure 4.27. It is shown that even when the temperature was set at -50°C, the temperature inside the pressurized vessel stayed over 0°C. Upon conducting this test, nitrogen gas was filled into the pressurized vessel to avoid condensation. In preparation for the flight, silica gel was placed into the pressurized vessel to further reduce water vapor concentration, and nitrogen gas was refilled.

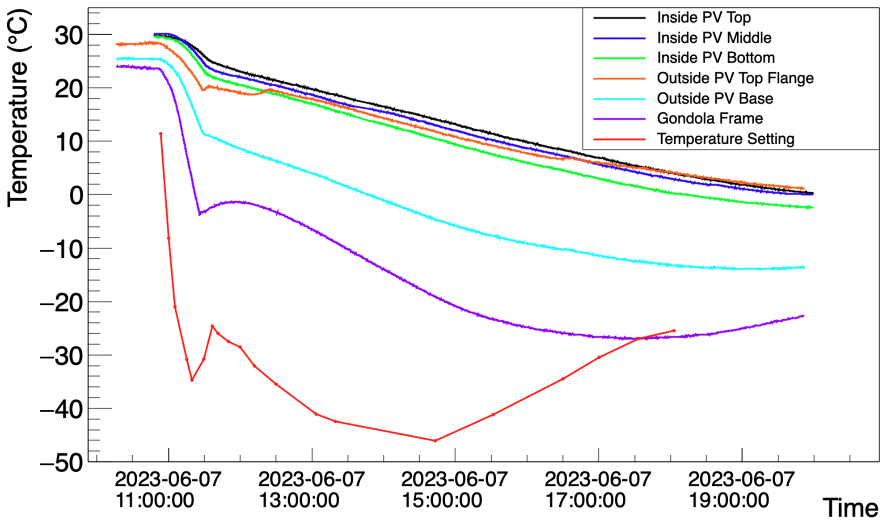

Figure 4.27: Temperature change during the vacuum test.

4.4.1 Power Supply System

One of the main challenges of a balloon experiment is the limitation in power. Therefore, designing a power system with high durability (operational at balloon conditions) and flexibility was key to the success of flight B23-06. The power supply system consisted of a primary lithium battery, a custom-made power divider board, and a switch. The schematic diagram of the power supply system is shown in Figure 4.28. In this system, the output of the battery is connected to the d-sub feedthrough. By doing this, the battery can be turned on or off with a switch, and for tests not requiring the battery power, an external power supply can be connected to the d-sub feedthrough. The power is fed to the power divider board which distributes the required power to all the components.

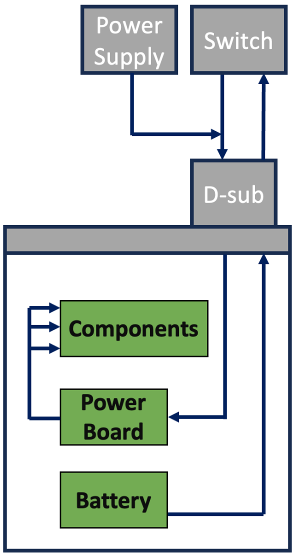

Figure 4.28: Schematic diagram of power supply system.

In selecting the battery, it was favorable to use batteries that can operate at low temperatures. The lithium primary battery used for this flight was manufactured by Electrochem Co. (product number: 3B0076). The operating temperature was from -55°C to +85°C. The nominal capacity was 30 Ah with a voltage of 3.9 V and a maximum current of 3.0 A. To provide sufficient power for the electronics, eight cells were connected in series. Therefore, the total capacity of the battery was 30 $Ah \times 3.9\ V \times 8 = 936\ Wh$. To ensure that the current doesn't exceed 3.0 A, a current limiter is placed on the power divider board. The operation voltage and current for the electric components used for the flight are shown in Table 4.2. For a 3-hour flight with the solenoid valve opened for 1 hour, the total power consumption is 108.18 Wh which is 11.5% of the total capacity.

Component	Voltage	Current
Solenoid Valve	24V	0.5A
Charge Preamp	±5V	0.5A
Pressure Gauge	12V	20mA
LArTPC Cathode High Voltage Module	12V	260mA
PMT High Voltage Module	5V	100mA
Raspberry Pi Model 4B	5V	3A
JAXA bus system	5V	40mA

Table 4.2: Operating voltage and current of each component.

The power divider board was custom-made by Shimafuji Electric Inc. and was designed to receive the discrete commands and power up the corresponding components with the given input discrete commands. The discrete commands were sent through the 37-pin D-sub cable and all the power lines were XA connectors for durability. DC-DC converters were used to convert the input voltage from the battery to the voltages shown in Table 4.2 for each component. Figure 4.29 shows a photo of the power divider board. For more details on the power divider board refer to [33].

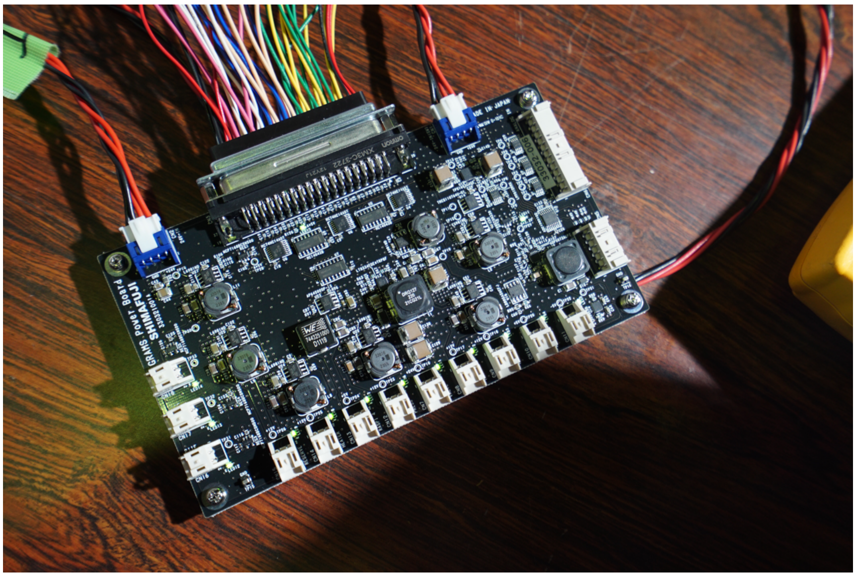

Figure 4.29: Photo of the power divider board.

4.4.2 Electronics for Detector System

In monitoring and controlling the detector system, a slow control system was required to monitor the LAr environment, and a DAQ system was required to obtain LArTPC and PMT data.

The slow control system for the cryostat was simple as most of the LAr control was done with components that do not require any power (e.g. absolute pressure valve). The

LAr environment was monitored with an absolute pressure gauge and three RTD temperature sensors. The resistance of the RTD sensors was digitized by a digital converter manufactured by Analog Devices Co. (product number: MAX31865) which was connected to the GPIO pins on the Raspberry Pi for readout. The pressure gauge value was digitized by an ADC onboarded on the power divider board which was also connected to the GPIO pins.

A schematic diagram of the DAQ system is shown in Figure 4.30. Three signal lines from the charge preamplifiers and the PMT signal (shown in the black lines) are digitized by two 2ch USB oscilloscopes. The USB oscilloscope used was the Analog Discovery 2 (AD2) made by Diligent Inc. The AD2 modules were connected to the Raspberry Pi via a USB connection (shown in light blue lines). The PMT signal was used as the trigger for the DAQ. The AD2 module connected to the PMT signal created the trigger for the other AD2 module and therefore a 4ch DAQ readout was possible. The high-voltage modules are powered by the power board and the high-voltage output is controlled by the AD2 modules as they can also function as a programmable power supply. The high voltage modules for the PMT and LArTPC cathode were compact modules manufactured by Hamamatsu Photonics (product numbers: C10940-53 and C14051-15, respectively).

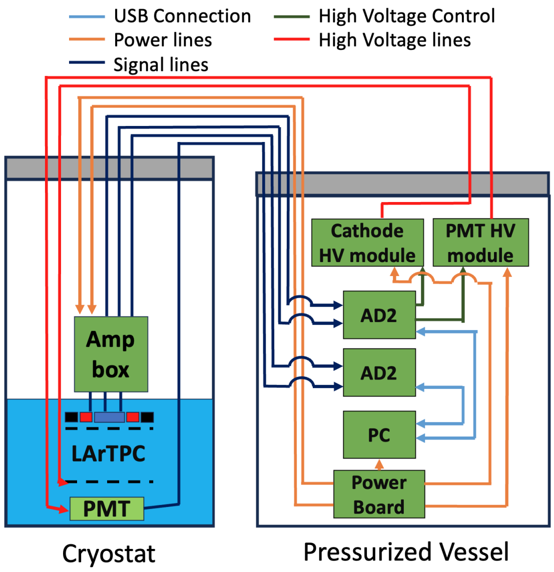

Figure 4.30: Schematic diagram of the DAQ system.

The specifications of the AD2 module are shown in Table 4.3. As the LArTPC was operated at 200V/cm, the ionized electron near the cathode takes approximately 100 μs to reach the anode. Since the buffer size is 8192 samples, the sampling rate was set at 50 MHz for the sample time window to be 160 μs long. The cathode and PMT high voltage modules had a range of -10 kV$\sim$0 V and 0 V$\sim$1.2 kV, respectively, and could be controlled with an external voltage between 0 to 5 V. Since the cathode high voltage was -2.5 kV and the PMT high voltage was 700 V, the AD2 output to the high voltage modules was 1.25 V and 3 V, respectively. For details of the software in the DAQ system, refer to [33].

Function	Specification	Value
Oscilloscope	Channels	2
	Sampling Rate	50 MHz (Max 100 MHz)
	Voltage Range	± 5 V
	Resolution	14-bit
	Buffer Size	8192 samples/channel
	Pre Trigger Time	-10 μs
	Max DAQ Rate	60 Hz
Power Supply	Channels	2
	Voltage Range	± 5 V

Table 4.3: Specifications of the Analog Discovery 2 module.

As the pressure decreases at balloon altitudes, the breakdown voltage of the surrounding atmosphere decreases, increasing the risk of discharge from high-voltage modules. Therefore, a custom-made high-voltage feedthrough was designed. The design consisted of an NW40 blank flange with two 3 mm holes, two 2.3 mm thick Kapton cables, and stycast 2850ftj epoxy. As shown in Figure 4.31, stycast was applied around the Kapton cables to prevent any leakage from the NW40 flange. The same technique was applied for the ICF70 flange for the high-voltage on the top flange of the cryostat.

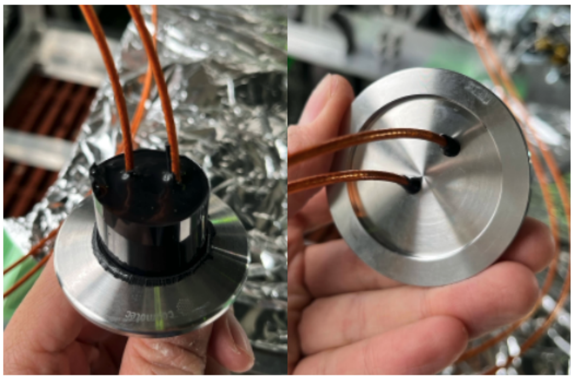

Figure 4.31: High-voltage feedthrough for NW40 port.

4.5 Telemetry and Command System

In a balloon experiment, the ground system and the experimental system are far apart, so the control and monitoring of various equipment must be done remotely. As LAr is cryogenic and requires frequent monitoring, communication with the balloon is especially important in terms of safety control. Furthermore, to operate the LArTPC at balloon altitudes, the detector system must be operated remotely.

For balloon experiments with JAXA, the communication system is provided by JAXA's balloon group. The three methods of communication are discrete commands, serial commands, and telemetry. Commands were used exclusively for transmission from the ground system to the balloon system to send commands to the balloon, while telemetry was used exclusively for transmission from the balloon to the ground to monitor the balloon's status. Serial commands and telemetry are serial communications that can send and receive multiple bits of information, while discrete commands can only send ON/OFF. A schematic diagram of the communication system for this flight is shown in Figure 4.32.

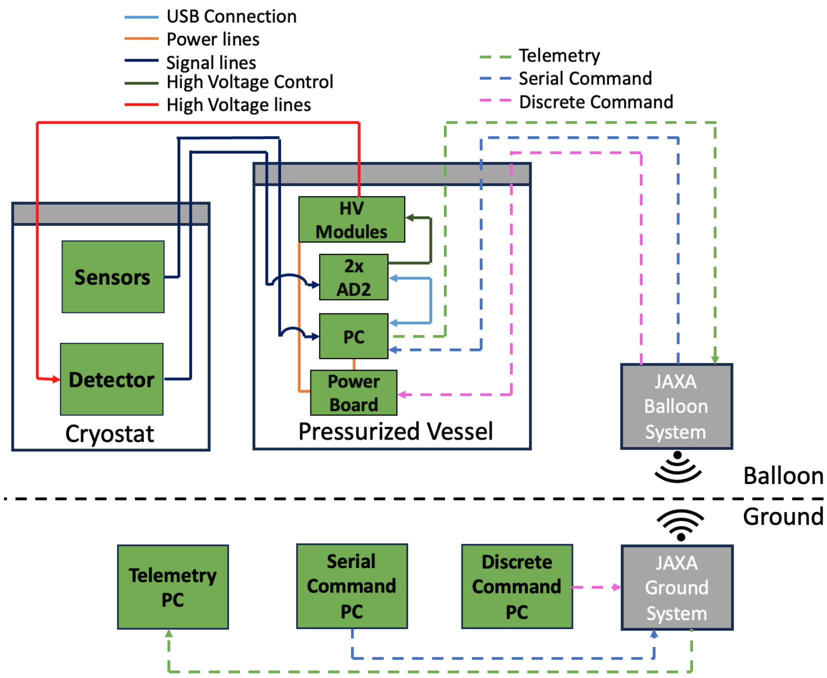

Figure 4.32: Communication system using JAXA's balloon bus system for this flight.

These communications are done using JAXA's balloon bus system which consists of a PIIF (PI Interface) device and SDCC2 (Serial Discrete Command) device as shown in Figure 4.33. The PIIF is a serial communication interface that is electrically isolated from the balloon bus, and the SDCC2 is a device that decodes discrete commands. The PIIF and SDCC2 were powered by the battery through the power board. The PIIF device was connected to the GPIO pins on the Raspberry Pi to send telemetry data. The SDCC2 was connected to the power divider board for turning ON/OFF different modules using the discrete command and was also connected to the GPIO pins of the Raspberry Pi to receive serial commands.

There were two main groups of telemetry data: continuous and on-demand. The continuous telemetry data consisted of the slow control data required for monitoring LAr. The continuous telemetry data was updated at 1∼3 Hz. Whereas, the on-demand telemetry was updated when a serial command for obtaining such data was sent. The on-demand telemetry was waveform data from the LArTPC and PMT. Therefore, the continuous telemetry was monitored at all times and the on-demand telemetry was obtained whenever the LArTPC status/setting was changed or to check waveform data. For details regarding the structure of the command and telemetry codes, refer to [33].

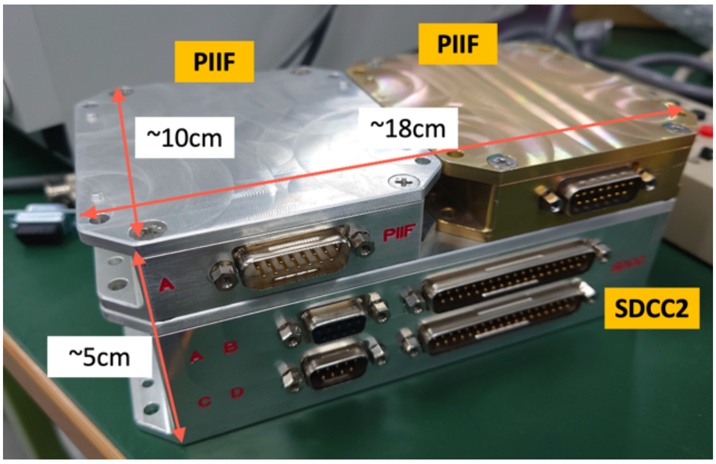

Figure 4.33: PIIF and SDCC2 device used for communication.

5 Flight Results

In this section, the results of the analysis of the slow control data, LArTPC, and PMT data will be described. In Section 5.1, a summary of the flight operations and the data obtained will be described. In Section 5.3, the waveforms of the 3ch LArTPC will be analyzed and the purity of LAr during the flight will be evaluated. In Section 5.4, the event rate will be calculated with a Geant4 simulation and compared to the flight data. Finally, in Section 5.5, the PMT data will be analyzed.

5.1 Flight Data Summary

This section will give an overview of the data that was collected on this flight. The data acquisition started during the final test before the launch, shown in Figure 3.10 in Section 3.5.2. At this stage, all the electronics were turned on except the LArTPC high voltage and charge preamplifiers. Therefore, all the slow control modules were monitored through the continuous telemetry and the PMT signal was able to be checked with the on-demand telemetry.

The operation during the flight and the event count with respect to time are shown in Figure 5.1. As shown, the LArTPC high voltage was turned on 5 minutes after launch and turned off before parachuting. This is because the LAr was expected to move around in the cryostat during launch and parachuting, and if the high voltage was turned on, the risk of discharge from the cathode increased. During the level flight, the trigger level was lowered using a serial command to collect gamma-ray events which deposit less energy in LAr. During LAr evacuation, the PMT trigger level was expected to decrease due to LAr being more sensitive than GAr. Therefore, the decrease in trigger rate which was monitored with the telemetry was an indicator of the completion of LAr evacuation. Hence, the PMT high voltage was turned on until the completion of the LAr evacuation. Shown in the red line is the event count over time and it is seen from the constant gradient that the DAQ rate is saturated from around 10 km altitude. In the DAQ system, 100 events were recorded per file and a total of 4716 files were completed during the flight. The file number and the operation state are shown in Table 5.1.

File Number	TPC High Voltage	Trigger Level	Flight Status
0∼27	off	-10mV	Ascend
28∼157	off	-200mV	Ascend
158∼3099	on	-200mV	Ascend
3100∼3458	on	-20mV	Level Flight
3459∼3632	on	-5mV	Level Flight
3633∼4070	on	-200mV	Level Flight
4071∼4716	off	-200mV	Descend

Table 5.1: Summary of the data taken and operation state during flight.

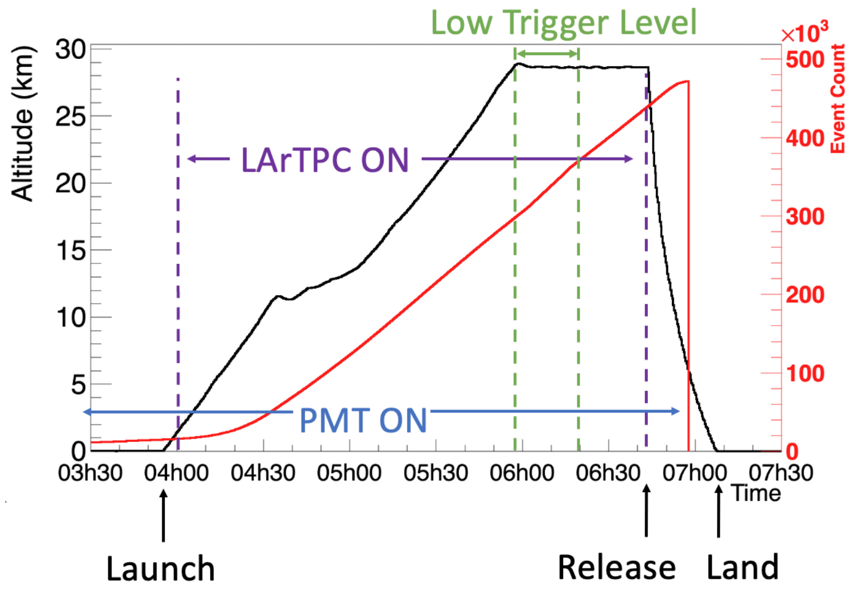

Figure 5.1: Operations during the flight.

5.2 LAr Handling Results

As mentioned above, the slow control modules were monitored throughout the flight and the data was stored in the SD card of the Raspberry Pi for offline analysis. The key measurements were the pressure of the cryostat and the temperature of LAr. Figure 5.2 shows the cryostat pressure, atmospheric pressure, and LAr temperature variations over time during the flight.

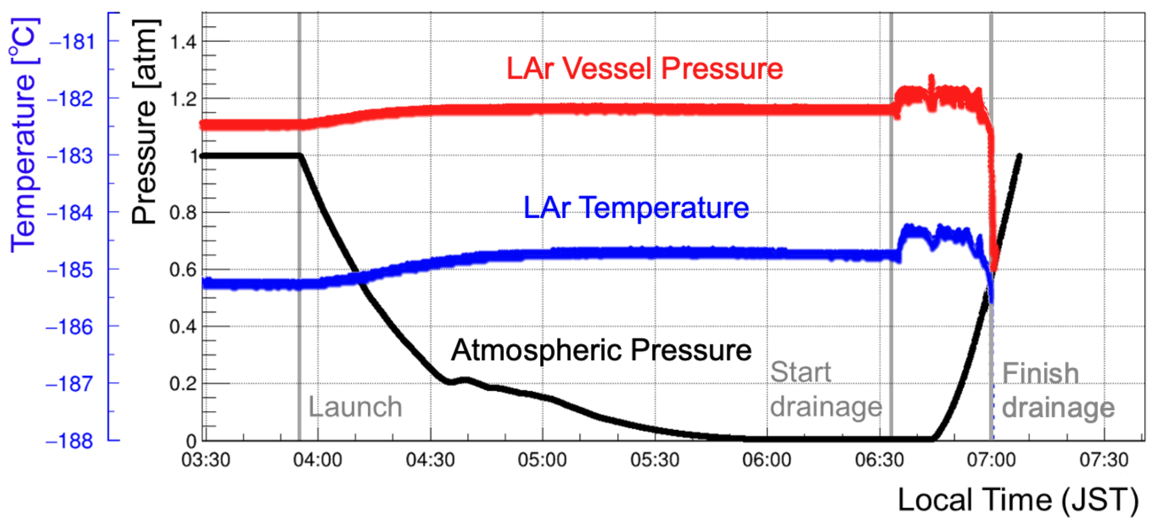

Figure 5.2: Variations in LAr vessel pressure (red) atmospheric pressure (black), and LAr temperature (blue) during flight.

It can be seen that despite the changes in atmospheric pressure (shown in black), the cryostat pressure (shown in red) was maintained within 1.1∼1.2 atm which was within the absolute pressure valve range. Therefore, the differential pressure valve and the rupture disk were not opened during the flight. The slight increase in pressure can be explained by the characteristic nature of the absolute pressure valve in which the opening pressure increases when the outer pressure decreases. The LAr temperature (shown in blue) was the measurement of the RTD sensor at the bottom of the cryostat. It can be seen that the LAr temperature was also kept constant with a slight increase corresponding to the increase in cryostat pressure.

The LAr evacuation was induced by opening the solenoid valve with a discrete command. The LAr evacuation started just before the release of the gondola. As shown in Figure 5.2, the cryostat pressure increases after the starting of the LAr evacuation. This was due to the LAr solidifying at the solenoid valve due to the atmospheric pressure being lower than 0.7 atm in which the liquid phase of argon does not exist. Therefore, the evaporated LAr goes back into the cryostat and increases the pressure. In the operation of LAr evacuation, the discrete command to open and close the solenoid valve was repeatedly sent which caused the fluctuation of the pressure. Eventually, the cryostat pressure became equal to the atmospheric pressure which suggests that the LAr evacuation was complete. Also, the decrease in trigger rate was confirmed at the same time.

5.3 LArTPC Data Analysis

As mentioned above, the LArTPC high voltage was turned on 5 minutes into the flight and turned off just before parachuting. During the flight, the LArTPC was operated at stable conditions and there were no major problems with the DAQ. In this section, the analysis of the 3ch LArTPC waveforms will be described in detail.

5.3.1 Waveform Fit using Ground Data

To gain an understanding of the LArTPC waveform, the analysis of the LArTPC data taken between the final test 1 and final test 2 shown in Figure 3.10 was conducted. This dataset is beneficial as the LAr environment was extremely stable and the events are mostly muons. A raw signal of an event (with the pedestal adjusted to 0V) obtained at the ground is shown in Figure 5.3. It can be seen that the first and last signal is ch1 (shown in black) and there are two signals on ch2 (shown in red) and one signal on ch3 (shown in blue). Therefore this event could be understood as a penetration event similar to the simulated event shown in Figure 4.22. However, the signal clarity could be improved as there is a common noise component. As shown in Figure 5.4, when there is no signal on any of the channels, the noise on each signal is very similar. Therefore, by subtracting the common noise component, the signal clarity would improve and by fitting the waveform, a simple track reconstruction would be possible.

Since the common noise component was present on all 3 channels, the noise component could not be subtracted easily when there were signals on all channels. Therefore, the difference between the two channels was considered. Precisely, ch2 was subtracted from ch1, ch3 was subtracted from ch2, and ch1 was subtracted from ch3. Therefore, in this

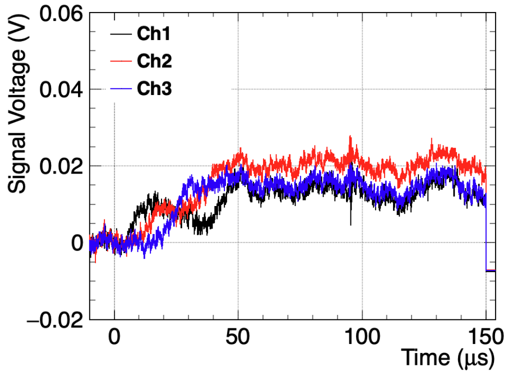

Figure 5.3: Single event obtained at ground.

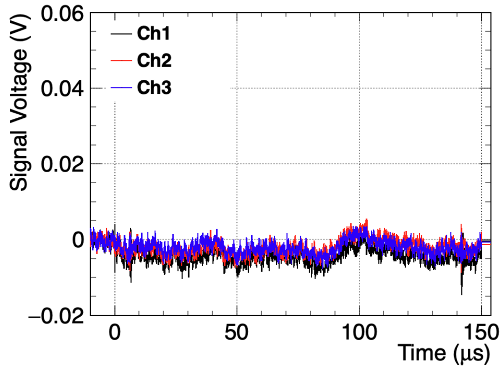

Figure 5.4: Event with no signal obtained at ground.

case, the common noise component will be removed from each channel and whenever there is a signal on any of the channels, the signal will have a certain start and end time with a positive gradient. Furthermore, for multiple hit events, the end of the first hit should be the start of the next hit, and so on. A single-track event can be divided into 14 different hit patterns as shown in Table 5.2 (except for events that are perfectly horizontal to the LArTPC).

First Signal Channel	Last Signal Channel	Number of Signals	Hit Pattern
1	-	1	1
1	2	2	12
1	1	3	121
1	3	3	123
1	2	4	1232
1	1	5	12321
2	-	1	2
2	1	2	21
2	3	2	23
2	2	3	232
2	1	3	2321
3	-	1	3
3	2	2	32
3	1	3	321

Table 5.2: Single track event hit patterns.

After the fit is completed for each subtracted signal, the fit functions are summed into a single fit function. In addition, by comparing the summed fit function to the sum of all three channels, the difference should be the common noise component multiplied by 3 (due to the summation of 3 channels). Figure 5.5 shows the subtracted signals being fit and the difference between the summed fit function and the sum of three channels (shown in pink). As shown in Figure 5.3, the signals on each channel are very distinct and have a certain start and end time with a positive gradient (the subtracted channel would have a negative gradient component at the same time). The result of subtracting the common noise component (shown in green) from each channel is shown in Figure 5.6. The event used is the same as shown in Figure 5.3 but re-binned by 50. As shown, the signal is much clearer, and due to the fit, the total signal voltage (height of the pink line in Figure 5.5) and the total signal time (time of the max height of the pink line in Figure 5.5)of the track can be calculated. Furthermore, searching for events with particular hit patterns is possible.

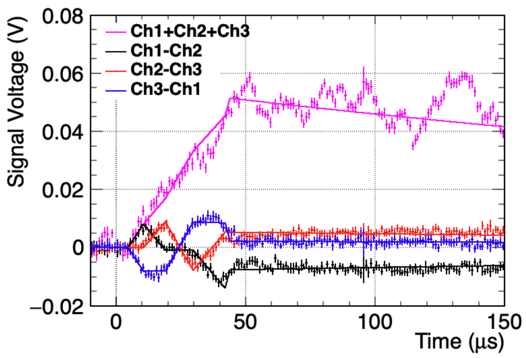

Figure 5.5: Fitting the subtracted channels and the summed fit function.

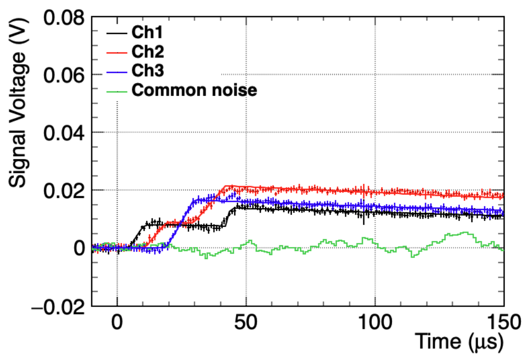

Figure 5.6: Each channel with common noise component removed.

5.3.2 Fit Result Comparison Between Ground and Flight Data

The fit method described in the previous section is valid for the flight data as there were no major changes in the detector operation between the ground and flight. In this section, the fit results are compared between the data taken on the ground and data taken during level flight. For the event selection process, the following cuts were made:

1. At least one hit in any of the channels
2. Fit range is larger than 30 μs
3. Chi^2/NDF value of fit is less than 20
4. Total signal time is longer than 10 μs

The fit results are shown in Figure 5.7. The histograms are normalized to the total event number. For the bottom two plots, dV/dt represents the total signal voltage divided by the total signal time for each event. The level flight data is shown in red and the ground data is shown in black. As shown on the top left plot, for the flight data, there is a higher ratio of events with a larger total signal voltage compared to the ground data. The bottom left plot also implies that there is a higher ratio of events which deposits more energy per unit time (length) for the flight data. This is as expected as the higher the altitude, there are more primary cosmic rays such as protons which have a larger dE/dx than muons.

Additionally, from the top right plot, it can be seen that the ground data has a higher ratio of events with longer signal time. This suggests that at the ground, events are more likely to pass from the anode to the cathode. Hence, the muons penetrating the LArTPC at the ground are coming from above. Whereas, more events penetrate the LArTPC from the side for the flight data. It can be seen from the bottom right plot, that for the flight data, the events which have a short signal time have a large dV/dt. Again, this implies that these events are not low-energy events occurring near the anode but particle tracks that penetrate sideways.

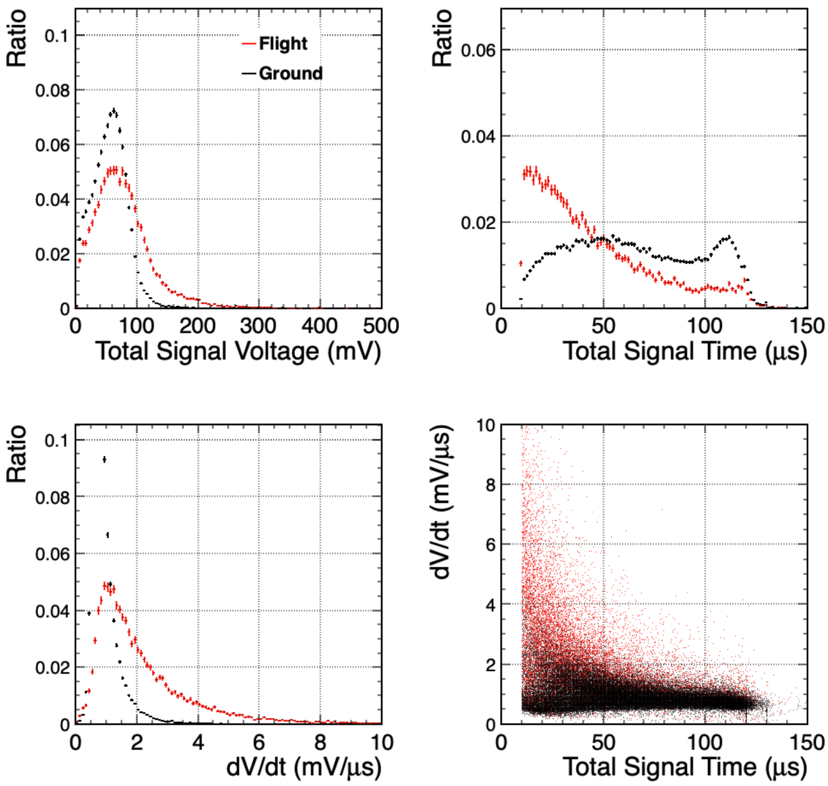

Figure 5.7: Fit result comparison between ground (black) and level flight (red) data. (Top left) Total signal voltage ratio. (Top right) Total signal time ratio. (Bottom left) dV/dt ratio (Top left) Total signal time against dV/dt.

As shown in Figure 5.7, there are more energetic events at higher altitudes. An example is shown in Figure 5.8. On the other hand, low energy events were also obtained during the start of the level flight when the trigger level decreased. Figure 5.9 shows a gamma-ray Compton scattering candidate in which the signal is only on ch3 which is the innermost pad. Since the rise time of the signal is $\sim$20 μs, this event occurred $\sim$2 cm below the anode.

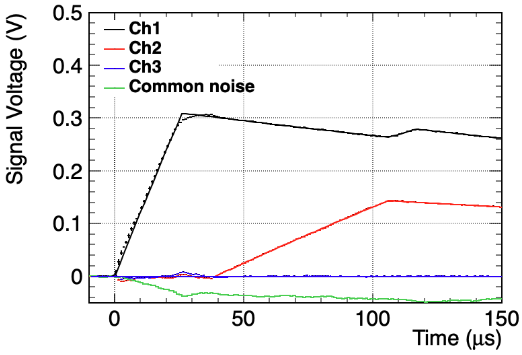

Figure 5.8: Energetic event obtained during flight.

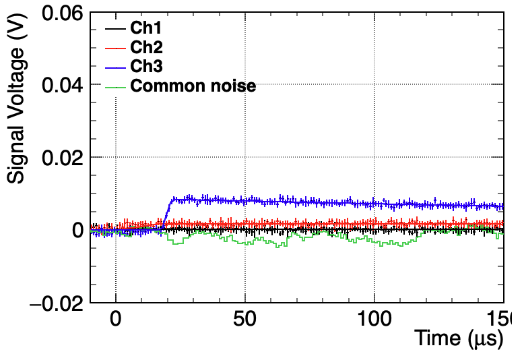

Figure 5.9: Gamma ray Compton scattering candidate.

5.3.3 LAr Purity

As mentioned in Section 2.2.1, electronegative impurities absorb the ionized electrons. Therefore, filling high-purity argon and maintaining the purity is essential for a LArTPC. In this section, the LAr purity before and after the flight will be evaluated.

As mentioned in Section 4.3.1, for LAr that is 100% pure, the charge signal should stay constant over time. However, when LAr has impurities, the charge signal and the corresponding output signal from the charge preamplifiers would be as shown in Figure 5.10.

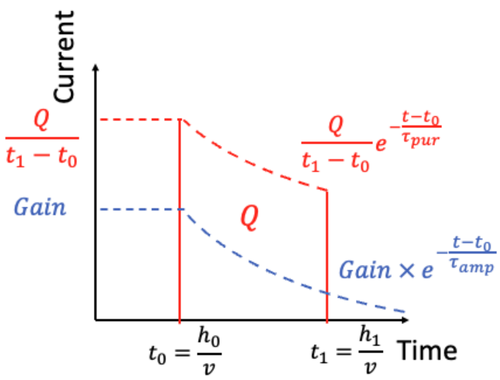

Figure 5.10: Charge signal for LAr with impurities.

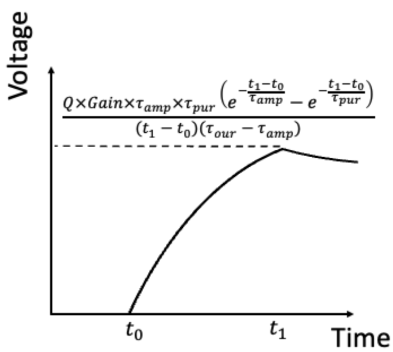

Figure 5.11: Output signal for LAr with impurities.

As shown in Figure 5.10 the current (charge signal) exponentially decays over time with the electron lifetime as the time constant. Therefore, the output signal from the charge preamplifiers will be a convolution between the current function and the charge preamplifier response function as shown below:

$$V_{out}(t) = I(t) * h(t) = \frac{Q}{t_1 - t_0} e^{-\frac{t-t_0}{\tau_{pur}}} * Gain \times e^{-\frac{t-t_0}{\tau_{amp}}} \tag{5.1}$$

$$= \frac{Q \times Gain \times \tau_{amp} \times \tau_{pur}}{(t_1 - t_0)} \left(e^{-\frac{t-t_0}{\tau_{pur}}} - e^{-\frac{t-t_0}{\tau_{amp}}} \right) \tag{5.2}$$

Here, τ_{amp} is the electron lifetime. For fitting this function, an output signal shown in Figure 5.11 is ideal. Therefore, for the 3ch LArTPC, the ideal hit pattern for purity evaluation would be 3, where a cosmic ray penetrates the LArTPC from the anode (above ch3) to the cathode (under ch3), leaving only a signal in ch3.

By using the fit method described in the previous section, events with hit pattern 3 were found for the ground data and level flight data. Single events from the ground and flight data are shown in Figure 5.12 and Figure 5.13, respectively. The dashed lines represent the signal with the same total signal voltage but with different LAr purity. The function above was used with the gain of the charge preamplifier as a free parameter and the start and end of the signal fixed. Additionally, the time constant of the charge preamplifier was set at 500 μs. It can be seen that for both ground and flight data, the liquid argon purity is sub-ppb level and therefore the purity was maintained during the flight. As shown in Figure 2.5, LAr purity of sub-ppb level corresponds to an electron lifetime of ~300 μs. Since the LArTPC is 10 cm in height, the maximum drift time is ~100 μs which implies that the purity was sufficient to read out the ionized electrons.

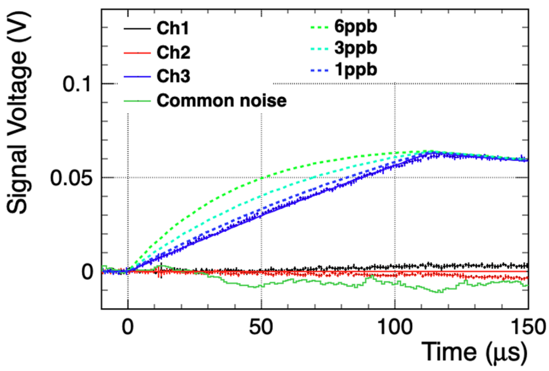

Figure 5.12: Hit pattern 3 event from ground data.

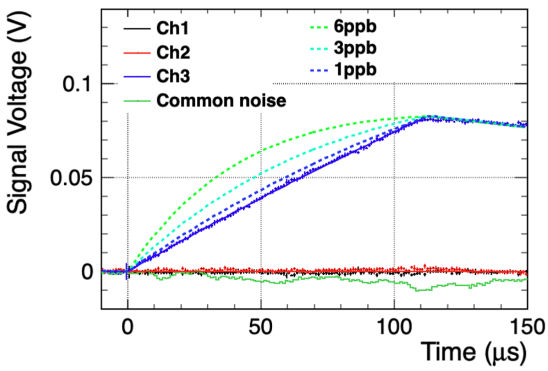

Figure 5.13: Hit pattern 3 event from flight data.

5.4 Event Rate Calculation

The analysis of event rates during the flight is crucial to understanding the performance of LArTPC under different fluxes of cosmic rays. In this section, the results of the Geant4 simulations will be presented, which were conducted to estimate the event rates at different altitudes. Following this, the simulated results and the actual data collected during the flight will be compared.

5.4.1 Rate Calculation using Geant4 Simulation

The rate calculation was conducted with Geant4 simulation with initialization inputs from EXPACS. Firstly, the flux, angular, and energy distribution of various particles at different altitudes were calculated using EXPACS. Secondly, The angular and energy distribution was used for the initialization of Geant4. Thirdly, the energy deposition distribution was outputted from Geant4 for each particle, for each altitude. Finally, the rate at each altitude was calculated using the energy deposition distribution and flux of each particle.

- **EXPACS Simulation**

Within the EXPACS simulation, the flux, energy distribution for energies between 0 to 10 GeV in 10 MeV bins, and angular distribution for every 10 MeV were calculated for each particle, for each altitude. Furthermore, the latitude and longitude were set before the simulation. For this simulation, the latitude and longitude were set for Taikicho, hence 35.75°N and 139.70°E, respectively. The simulated particles are protons, helium, mu^+, mu^-, e^+, e^-, and gamma-ray. The simulated altitudes range from 0 to 27.5 km with 2.5 km increments. As an example for mu^+ at ground (0 km), the flux is 0.007422610 /cm^2/s and the angular distribution between 5 GeV and 5.01 GeV energy range and energy distribution is shown in Figure 5.14 and Figure 5.15. The angular distribution is in the form of $\cos(\theta)$ where θ is the zenith angle.

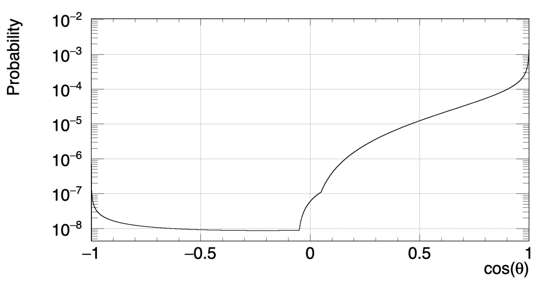

Figure 5.14: Angular distribution of mu^+ at the ground for energies between 5 GeV and 5.01 GeV.

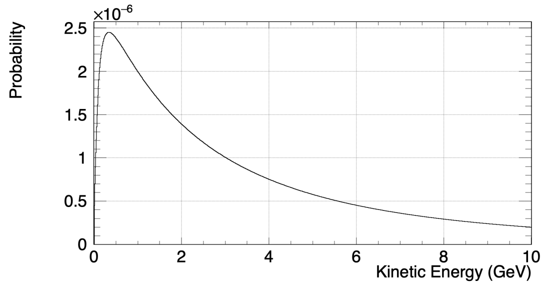

Figure 5.15: Energy distribution of mu^+ at ground between 0 and 10 GeV.

- **Geant4 Simulation**

The initialization parameters for the Geant4 Simulation are particle ID, particle energy, particle direction, and number of events. The setup of the cryostat and LArTPC is shown in Figure 5.16. The LAr in the cryostat was set to have a height of 160 mm from the base, covering the LArTPC. Above the LAr, the space was filled with GAr.

For each iteration, the type of particle and altitude was chosen. Then, 400000 particles were generated from a sphere of radius 800 mm which covers the entire cryostat. The particle energy and particle direction were initialized based on the distributions as shown in Figure 5.15 and Figure 5.14. Finally, the total energy deposition in the LArTPC for each event was recorded. As an example, Figure 5.17 shows the energy deposition distribution for mu^+ at the ground.

- **Rate Calculation**

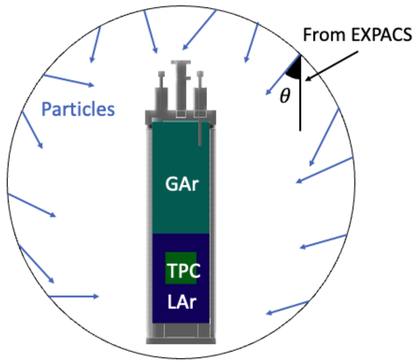

Figure 5.16: Geant4 setup with LAr and GAr filled into the cryostat containing the LArTPC.

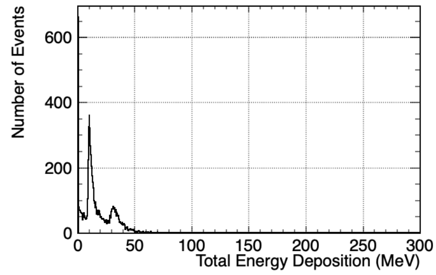

Figure 5.17: Energy deposition in LArTPC for mu$^+$ at ground.

From the Geant4 output, the energy deposition distribution is obtained. Since the flux of each particle at a given altitude can be calculated from EXPACS, the y-axis of the energy deposition distribution can be converted into the rate. The calculation for the conversion is stated below:

$$Rate\,(/s) = Flux\left(/cm^2/s\right) \times ratio \times OrthodromeArea\left(cm^2\right) \tag{5.3}$$

In this equation, the flux is the calculated value from EXPACS, the ratio is the number of events depositing a given energy divided by the total number of events generated in Geant4 and the orthodrome area is πr^2 where r is the radius of the sphere which particles are generated from. Therefore, by taking the energy deposition distribution, the flux and orthodrome area is multiplied to each bin content and divided by the total number of events. Figure 5.18 and Figure 5.30 show the rate of each particle at the ground to 27.5 km altitude, respectively. Here, the y-axis is normalized to (/s/MeV). It can be seen that on the ground, most of the particles entering the LArTPC are muons. On the other hand, as the altitude increases, the rate of muons is suppressed and the rate of primary cosmic rays such as protons increases. Additionally, the rate of events that deposit more energy in the LArTPC is higher at higher altitudes compared to the ground. Furthermore, the high-energy deposition events are induced by electrons and protons rather than muons which are mostly MIPs.

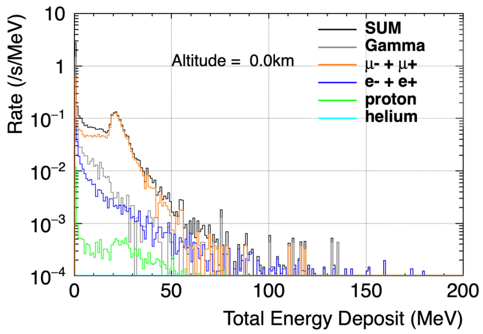

Figure 5.18: Rate of different particles at 0.0 km.

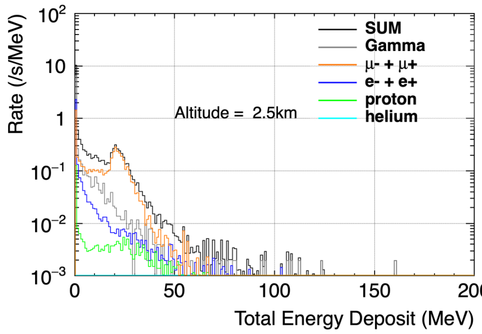

Figure 5.19: Rate of different particles at 2.5 km.

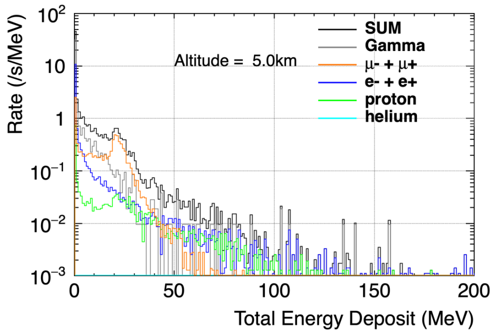

Figure 5.20: Rate of different particles at 5.0 km.

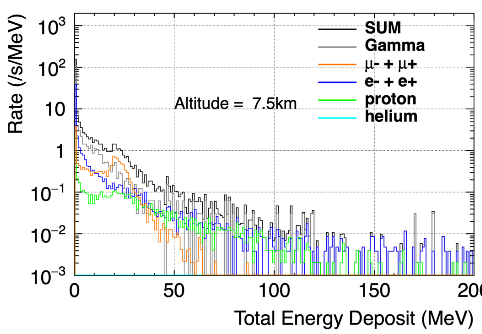

Figure 5.21: Rate of different particles at 7.5 km.

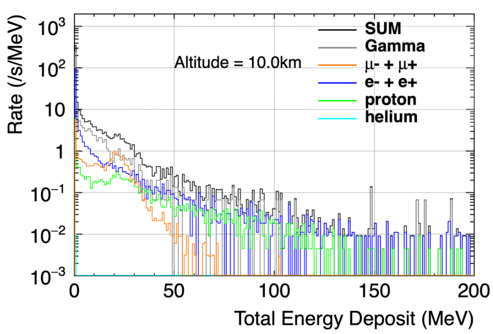

Figure 5.22: Rate of different particles at 10.0 km.

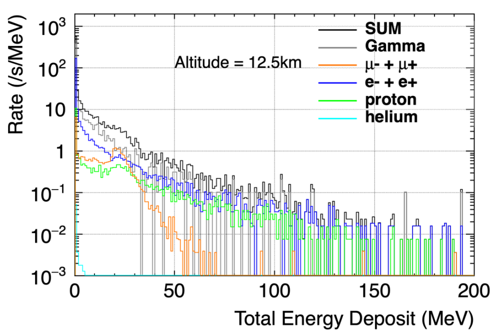

Figure 5.23: Rate of different particles at 12.5 km.

Figure 5.24: Rate at different altitudes (0.0 km to 12.5 km).

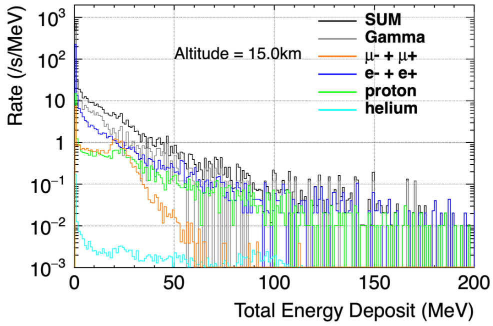

Figure 5.25: Rate of different particles at 15.0 km.

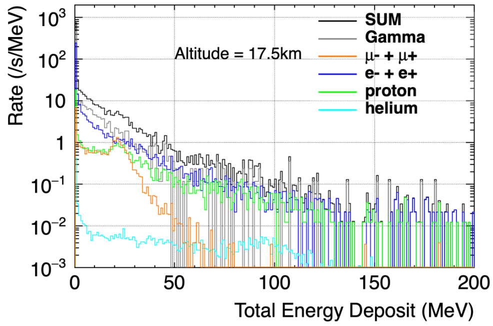

Figure 5.26: Rate of different particles at 17.5 km.

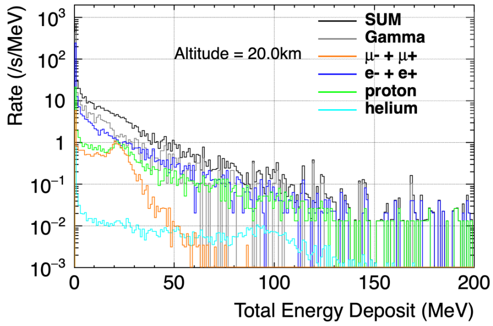

Figure 5.27: Rate of different particles at 20.0 km.

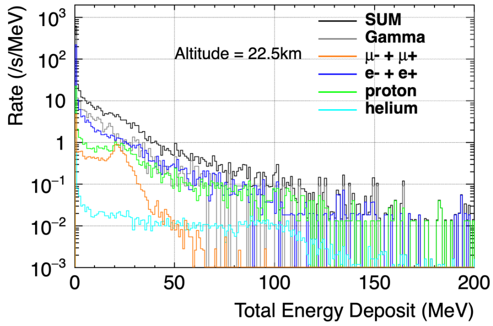

Figure 5.28: Rate of different particles at 22.5 km.

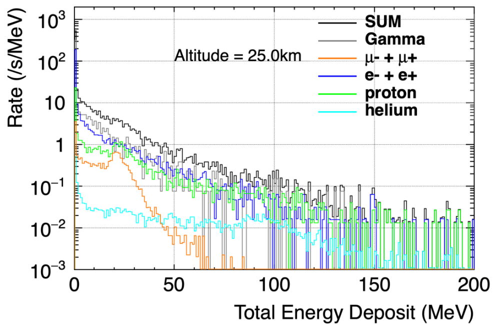

Figure 5.29: Rate of different particles at 25.0 km.

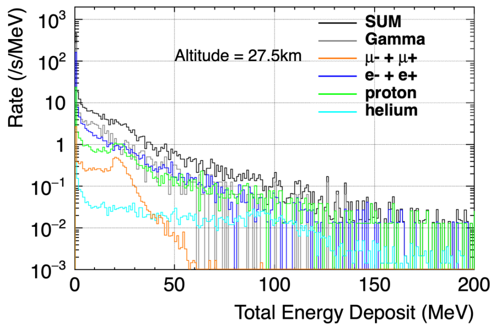

Figure 5.30: Rate of different particles at 27.5 km.

Figure 5.31: Rate at different altitudes (15.0 km to 27.5 km).

By integrating the rate over the total energy deposit, a threshold distribution is made. The threshold rate distribution describes the total rate at a given threshold. The threshold rate distribution for the ground to 27.5 km is shown in Figure 5.32 and Figure 5.44, respectively. From the threshold rate, it can be seen that the maximum rate is the value of the first bin which is the total rate of events that deposit more than 1 MeV in the LArTPC. Furthermore, when comparing the maximum rate between ground and 27.5 km, the maximum rate is 2 orders of magnitude larger at 27.5 km. Additionally, the rate gradually increases from 0.0 km to 20.0 km but decreases at higher altitudes.

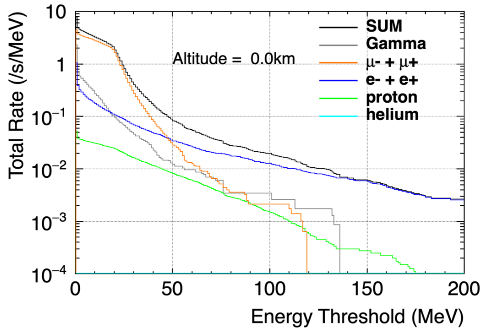

Figure 5.32: Threshold rate of different particles at 0.0 km.

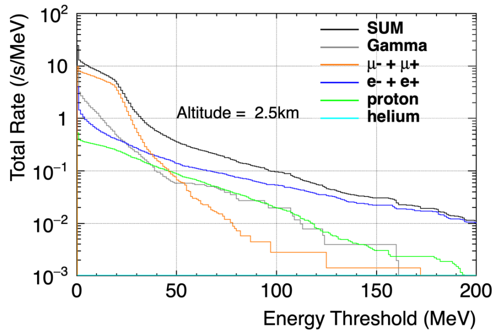

Figure 5.33: Threshold rate of different particles at 2.5 km.

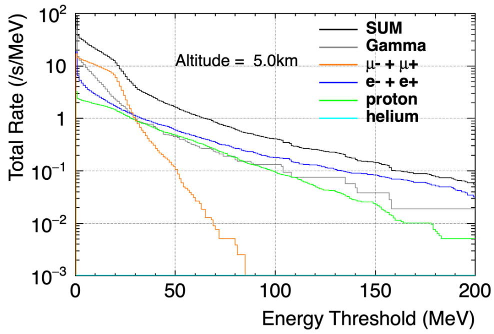

Figure 5.34: Threshold rate of different particles at 5.0 km.

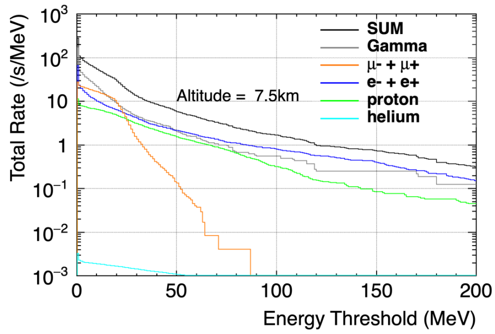

Figure 5.35: Threshold rate of different particles at 7.5 km.

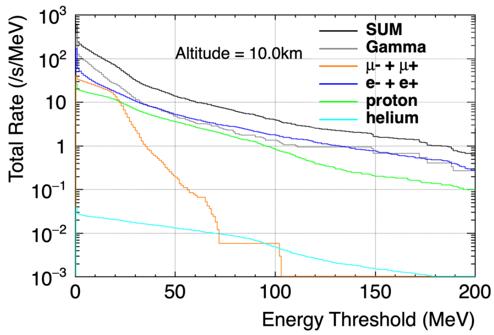

Figure 5.36: Threshold rate of different particles at 10.0 km.

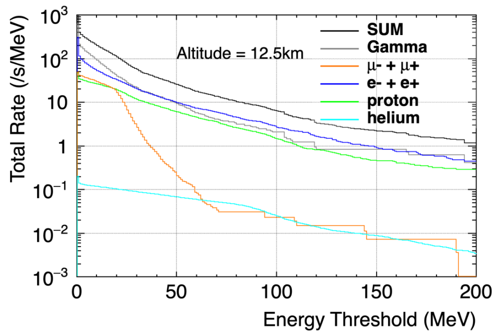

Figure 5.37: Threshold rate of different particles at 12.5 km.

Figure 5.38: Threshold rate at different altitudes (0.0 km to 12.5 km).

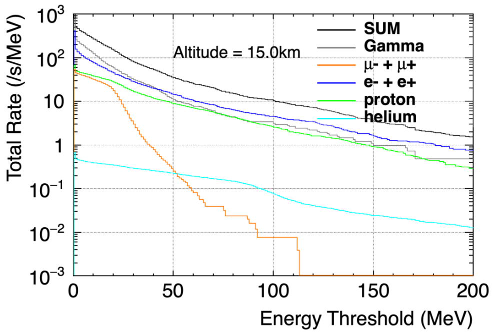

Figure 5.39: Threshold rate of different particles at 15.0 km.

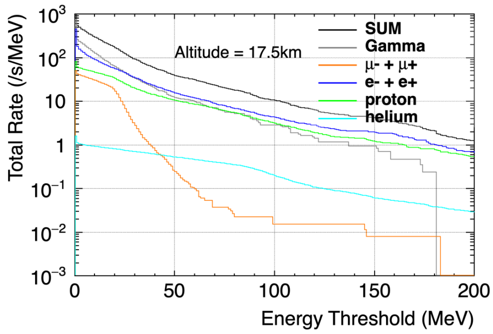

Figure 5.40: Threshold rate of different particles at 17.5 km.

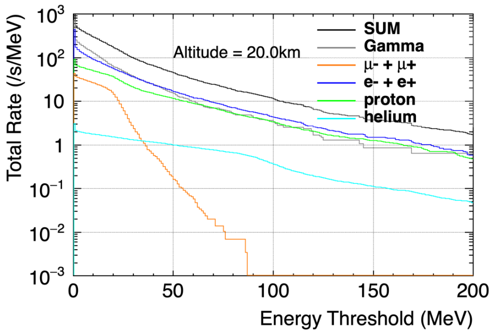

Figure 5.41: Threshold rate of different particles at 20.0 km.

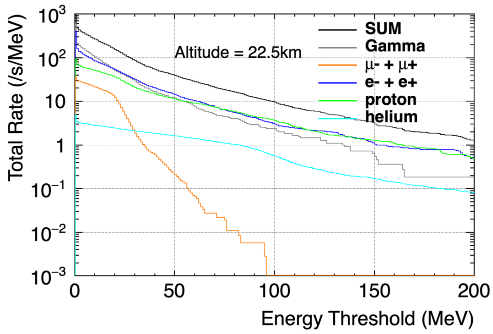

Figure 5.42: Threshold rate of different particles at 22.5 km.

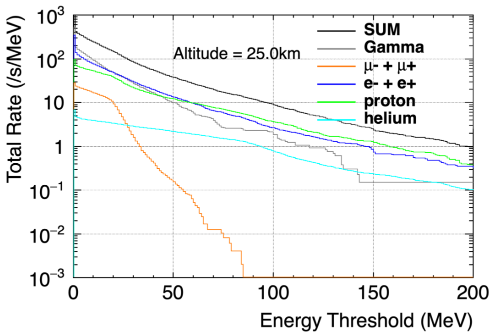

Figure 5.43: Threshold rate of different particles at 25.0 km.

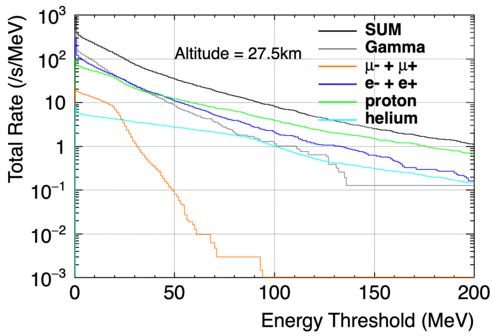

Figure 5.44: Threshold rate of different particles at 27.5 km.

Figure 5.45: Threshold rate at different altitudes (15.0 km to 27.5 km).

5.4.2 Rate Calculation with Flight Data

For this flight, the AD2 modules used in the DAQ system had a maximum trigger rate of 60 Hz. Therefore, the trigger rate was saturated during the flight and cosmic rays that entered the TPC during dead time were not able to be recorded. Therefore, to calculate the true rate, the distribution of event time intervals was used. In other words, the interval between two corresponding events was filled in a histogram. By modeling the rate of cosmic rays entering the LArTPC as a Poisson parameter, the event time interval distribution should be able to be fitted by an exponential function with the fit parameter being the true rate given by:

$$y = Ae^{-Rate \times \Delta t} \tag{5.4}$$

Therefore, to calculate the true rate at a given altitude, the time interval distribution of 1000 events at a certain altitude was made at 2.5 km increments. Figure 5.46 shows the event time distribution at 5 km altitude fitted with an exponential function. The x-axis represents the time between each event, Δt in equation 5.4. Additionally, Figure 5.47 shows the true rate at each altitude from the exponential fit compared to a 5 MeV threshold rate from the Geant4 simulation results. The rate calculated from the event time interval distribution is shown in black and the threshold rate from the Geant4 simulation is shown in red. As shown in Figure 5.47, the rate increases with altitude, reaches a shower maximum at $\sim$20 km which is observed for both the data and Geant4 simulation results, and decreases after the shower maximum with increasing altitude. The difference between the data and simulation results stems from the PMT having a TPB layer which implies that events which does not enter the TPC but leave a track above the PMT are included in the data. Whereas, the Geant4 simulation only considers the energy deposited in the LArTPC.

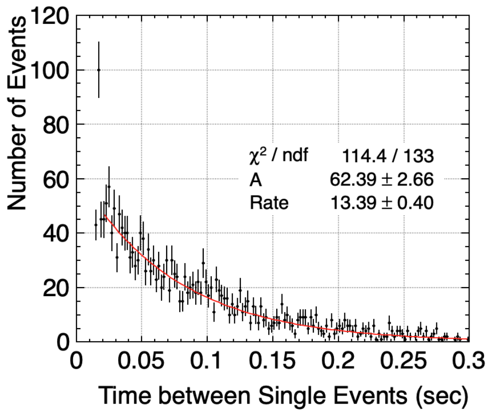

Figure 5.46: Event time interval distribution at 5 km altitude and the exponential fit results. The X-axis represents the difference between the trigger time of successive events.

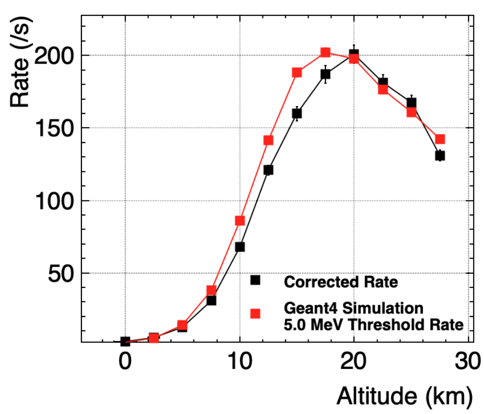

Figure 5.47: Calculated rate and threshold rate from Geant4 simulation at given altitudes.

In addition to the comparison between the calculated rate and Geant4 simulations, the top left plot which is the total signal voltage distribution in Figure 5.7, could be compared to the rate plot from the Geant4 simulation. Firstly, the units of the x-axis have to be converted from mV to MeV. In order to do this, the bottom left plot showing the dV/dt distribution for ground in Figure 5.7 is used. This is because, for the ground data, most of the events are muons. Therefore by fitting the dV/dt distribution with

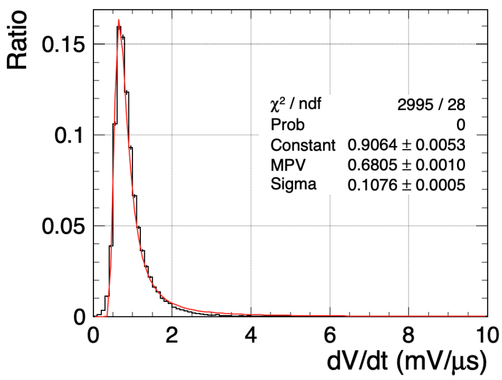

Figure 5.48: dV/dt distribution at ground fitted with a landau distribution.

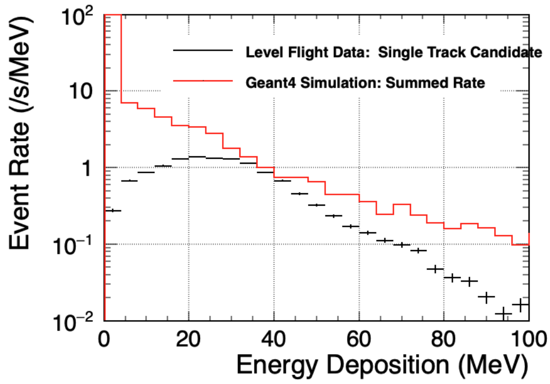

Figure 5.49: (Black) Rate at level flight converted from total signal voltage distribution. (Red) Summed rate of particles at 27.5 km from Geant4 simulation.

a landau distribution, the MPV value of dV/dt can be obtained. Since the dE/dx of a muon (2.1 MeV/cm @ MIP) is known from the Bethe-Bloch equation, the conversion is possible as follows:

$$\frac{dV}{dt} = \frac{dE}{dx} \times v \tag{5.5}$$

Here, v is the drift speed of electrons in LAr, shown in Figure 2.7. At 200 V/cm, the drift speed is approximately 0.12 cm/s. The dV/dt distribution fit with a landau distribution is shown in Figure 5.48. The MPV value is calculated as 0.6805±0.001. Therefore, 1 $mV = 2.1 \times \frac{0.12}{0.6805} = 0.37$ MeV. Secondly, the y-axis has to be converted. This can be done by multiplying each bin by the flux at 27.5 km which is 130 Hz from the calculated rate.

The converted plot from the total signal voltage distribution to a rate plot with MeV as x-axis units is shown as the black line in Figure 5.49. The red line represents the summed rate of particles at 27.5 km altitude which is the same as the black line in Figure 5.30. The difference between the data and simulation arises from the data applying cuts to the event selection. The difference is largest at low energies and higher energies. Regarding the low energy region, the trigger level for the level flight data used is set at -200 mV, and therefore low energy events were less likely to be triggered. At higher energy regions, the events are more violent and could contain electromagnetic showers which are not a single track, hence being rejected by the goodness of fit. However, the data and simulation are in agreement within an order of magnitude from 10 MeV and above.

5.5 PMT Data Analysis

For this engineering flight, the PMT signal was used for the trigger in the DAQ system. However, by analyzing the PMT data, the correlation between the LArTPC signal and the PMT signal can be understood. Furthermore, the Geant4 + EXPACS simulation can be compared to the PMT data. This section will describe the signal processing and analysis of the PMT data.

A typical PMT signal for a cosmic ray penetration event is shown in Figure 5.50. As mentioned in Section 2.2.1, a fast (7 ns) component is followed by a slow (1.6 μs) component. As a characteristic of the PMT used for this flight, the signal contains an undershoot component (red line in Figure 5.50. Therefore, the PMT signal is corrected as shown in blue. By integrating the PMT signal, the total light yield for each event can be obtained. Figure 5.51 shows the distribution of the total light yield of all events in black, and the total light yield of cosmic ray penetration events with the hit pattern 12321 in red. Both the distributions show a landau distribution as expected from cosmic rays.

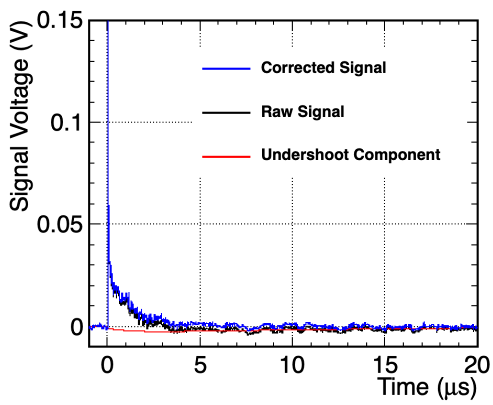

Figure 5.50: A typical PMT event for a cosmic ray penetration event.

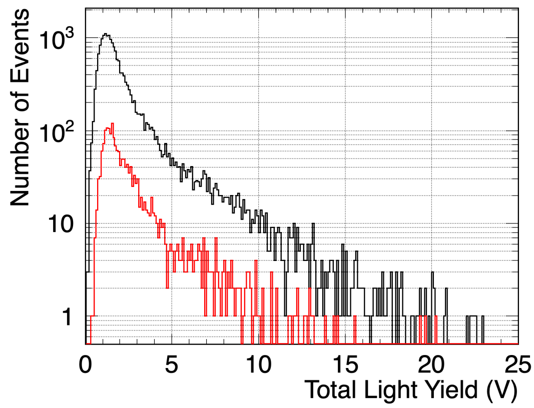

Figure 5.51: Total light yield of PMT signal. (Black) all events, (red) cosmic ray penetration events with hit pattern 12321.

Next, the correlation between the total light yield from the PMT signal and the total signal voltage from the LArTPC signals is investigated. The main purpose of this is to be able to find a correlation between light and charge signals to convert the light yield into energy deposited (as the conversion from charge to energy deposited has already been established). Therefore, for cosmic ray penetration events with the hit pattern 12321, the total light yield and the total signal voltage are calculated and plotted as shown in Figure 5.52. To visualize the correlation, the data along the X-axis (light) is projected, while taking the average of the corresponding Y-values (charge) as shown in Figure 5.53. The range of the total light yield was set from 0 to 5 V as there were limited statistics above a light yield of 5 V. Then, a linear fit was conducted showing a correlation of 29.14 mV of signal voltage per volt of light yield. Ideally, the fit should pass through the origin as there should not be an event when there is a charge signal but no light signal as impurities affect the ionized electrons more drastically. However, this could be explained due to the data being limited to the cosmic ray penetration events with a hit pattern of 12321 and a possible low light detection efficiency.

Finally, by using the correlation factor, the light yield can be converted to the energy deposited by first converting the light to charge followed by the charge to the energy de-

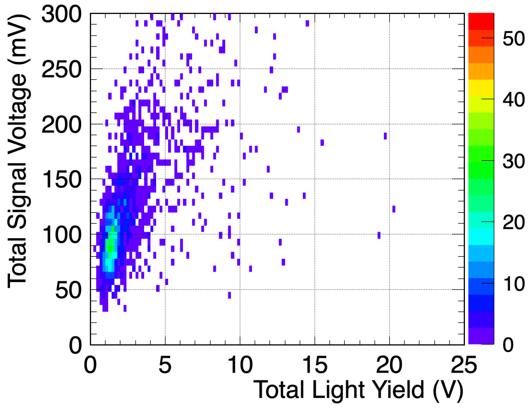

Figure 5.52: Plot showing the correlation between light and charge signals

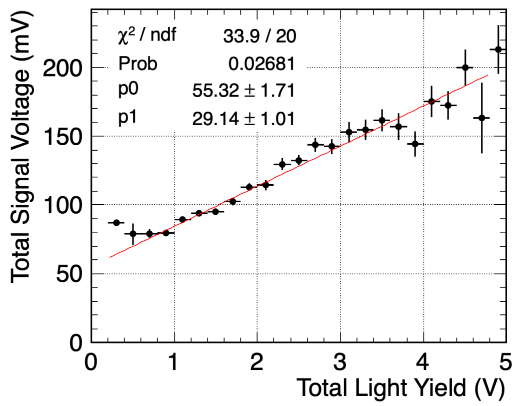

Figure 5.53: Projection of the Total light yield to the total signal voltage.

posited. Therefore, the total light yield distribution shown in Figure 5.51 can be compared to the rate plot from the Geant4 simulation shown in the red line in Figure 5.49. Firstly, the x-axis is converted from total light yield to total signal voltage by multiplying each bin by the light-to-charge conversion factor (29.14). Then, the same steps are repeated as described in Section 5.4.2.

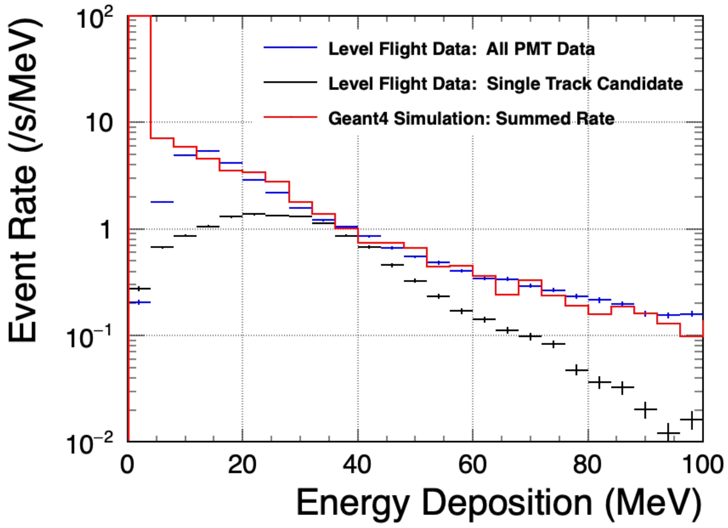

Figure 5.54: (Blue) Rate at level flight converted from total light yield distribution. (Black) Rate at level flight converted from total signal voltage distribution. (Red) Summed rate of particles at 27.5 km from Geant4 simulation.

The result is shown in Figure 5.54, and the total light yield distribution converted to a rate plot is shown in blue, drawn upon Figure 5.49. It can be seen that the rate plot from the PMT data agrees better with the Geant4 simulation than the single-track candidate. This is expected as the PMT data includes events in which the LArTPC signals could not be fitted (electromagnetic showers). However, the Geant4 simulation only considers events that deposited energy within the LArTPC volume. Whereas, the PMT data includes events with only light signals and no LArTPC signals (due to a possible low light collection efficiency, cosmic rays penetrating the cryostat between the PMT and the cathode). Therefore, improving the Geant4 simulation to include these effects would produce more accurate results.

6 Discussion

Through this engineering flight, a stable LAr handling system for a 22 L cryostat with a small-scale LArTPC was established. As the main goal was to safely handle LAr at balloon altitudes, the LAr handling system was designed to be robust with minimal operations required during the flight. Furthermore, the LArTPC was designed to be as simple as possible to prevent it from being a bottleneck during the R&D duration. Our findings reveal that for a short-duration flight (a few hours), the LAr could be continuously evaporated and the pressure could be maintained with a single absolute pressure valve. Furthermore, the LAr purity was maintained with no circulation system required. However, areas of R&D for future balloon flights were also identified and are summarized below.

- **LAr Evacuation Procedure**

For this engineering flight, the LAr handling system consisted of an absolute pressure gauge with two safety valves: differential pressure valve & rupture disk. In this system, the cryostat pressure was maintained without electronics with no operations needed. The only operation required during the flight was opening the solenoid valve to evacuate the LAr during descent. As expected, due to the low atmospheric pressure, the LAr froze at the solenoid valve outlet causing the evacuation pipe to be stuck until the atmospheric pressure increased to the triple point pressure. For future flights, even if the LAr evacuation is not necessary before recovery, to minimize the risk, a system able to evacuate LAr at higher altitudes may be required, especially for future flights in which more LAr is needed for a larger LArTPC.

- **LAr Purity**

In addition, operating the LArTPC and obtaining cosmic ray data was another objective of this engineering flight. In evaluating the LAr purity through the LArTPC data, a relative comparison to theoretical signals with different LAr purity was conducted. However, a more quantitative approach would be to fit the LArTPC waveform with the final output function to obtain the electron lifetime purity. The difficulty in this approach was the uncertainty in the gain and time constant of the charge preamplifier under cryogenic conditions. Therefore, for future flights, a thorough calibration process for electronics is required for a more accurate analysis. Furthermore, although the LAr purity was maintained and subsequent for a 3-hour flight with a 10cm LArTPC, a study on the time degradation of LAr purity is required as for the full GRAMS flight at the South Pole, the LAr purity has to be maintained for around 30 days.

- **Event Rate (Pile Up)**

Next, the event rate was calculated from the trigger rate interval and simulated from an EXPACS + Geant4 simulation. The results showed that for a 10 cm x 10 cm x 10 cm LArTPC, the shower maximum is approximately 200 Hz. Therefore, when considering a

LArTPC of similar size to the GRAMS40 detector, the rate will increase by an order of magnitude. Considering the drift time of electrons, a pile-up of events is expected. In this case, various aspects need to be taken into consideration. For example, to counteract the high rate, the electric field could be increased to drift the electrons faster and reduce the DAQ time window. If so, a high-voltage supply system ($\geq$10kV) that can be operated safely at balloon altitudes must be developed. Towards future flights, building the electronics for a larger LArTPC (a few hundred channels on the anode) with a higher rate, under newly defined power and weight limitations are the next topics for R&D.

7 Summary and Prospects

The GRAMS experiment is a next-generation balloon experiment utilizing a LArTPC with the goal to simultaneously observing MeV gamma-rays and cosmic antiparticles. In preparation for the long-duration balloon flight in Antarctica, various areas of R&D need to be conducted. One of the main R&D topics is being able to handle LAr safely and stably at balloon altitudes. To establish this milestone, an engineering balloon flight using a small-scale 3ch LArTPC was conducted with JAXA's balloon group on 27th July 2023.

The main objective of this flight was to establish a LAr handling system to monitor and control LAr throughout the flight. For the full objective, a maximum altitude of 28 km and a level flight of 10 minutes were requested. Also, the LArTPC was to be operated during the flight to obtain cosmic ray data. Furthermore, as it was the first balloon flight for the GRAMS experiment, it was essential to gain a thorough understanding of how balloon experiments are conducted and the implications it may have for preparing and utilizing LArTPCs for balloon experiments. The flight was successfully conducted and a maximum altitude of 28.9 km was reached where a 44-minute level flight was completed. The temperature and pressure of LAr were monitored during the flight and the pressure was controlled with an absolute pressure valve. The LAr evacuation was completed during the descent and a safe recovery of the payload was conducted.

The LArTPC was operated during the flight and cosmic ray data was obtained. In analyzing the LArTPC data, the signals on the three channels were fit to obtain energy deposition, signal time information, and track patterns. The LAr purity was evaluated and the results show that the LAr purity was sub-ppb level before and during the flight. In addition, the true event rate was calculated from the trigger rate and compared to an EXPACS + Geant4 simulation. In both the data and simulation results, the rate function shows a shower maximum at around 20 km altitude. In summary, the flight was successful as the full objective was achieved.

Regarding the future R&D timeline for GRAMS, an antiproton beam test is planned for Winter 2024 at J-PARC K1.8BR beamline. The main purpose of this test is to clarify the antiparticle capture process in LAr which is one of the major milestones for GRAMS. Therefore, the plan is to move the LAr test stand at Waseda to the K1.8BR beamline. For the GRAMS40 LArTPC, the anode will be upgraded to have double the position resolution (1 cm to 0.5 cm pitch) and the readout electronics will also be upgraded to readout 120ch from the anode. Additionally, a balloon flight was approved by the NASA/APRA program (pGRAMS) which will take place from Fall 2025 to Spring 2026 in Arizona, USA. The goal of this balloon flight is to observe gamma-ray Compton scattering events with the LArTPC. The LArTPC for this flight is planned to be comparable in size to the GRAMS40 LArTPC which suggests that the particle tracking of various cosmic rays would be possible. Furthermore, to reach an antideuteron sensitivity around 10^{-6}, a long-duration balloon flight at high latitudes ($\geq$60°) and high altitudes ($\geq$35 km) is required. The experience and insights gained from this engineering flight and pGRAMS will be leveraged in future balloon flights reaching the scientific goals for GRAMS.

A Vessel Designs

The blueprint of the Cryostat and the top flange is shown in Figure A.1 and A.2. Figure A.3 is the blueprint for the pressurized vessel.

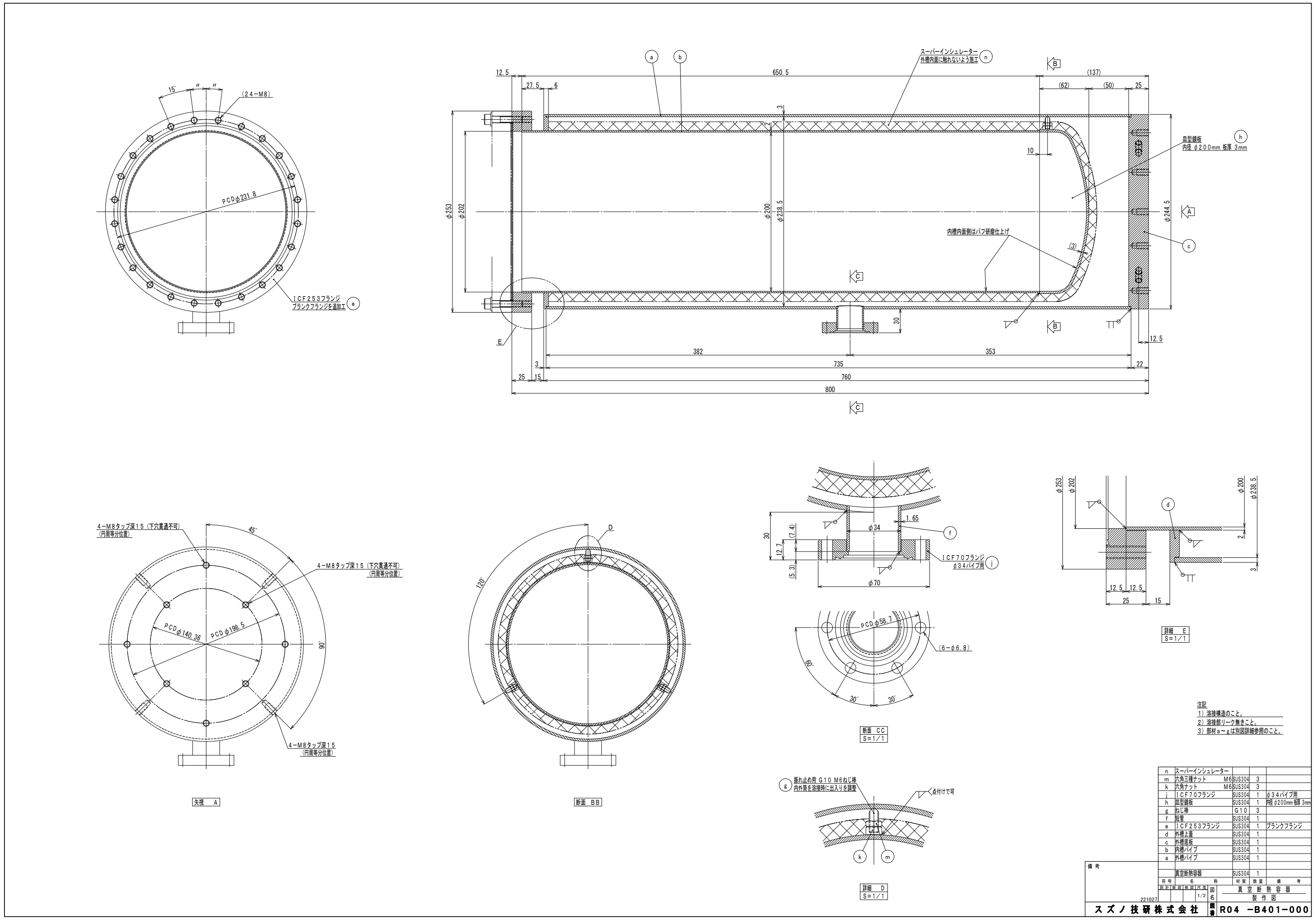

Figure A.1: Blueprint of the cryostat.

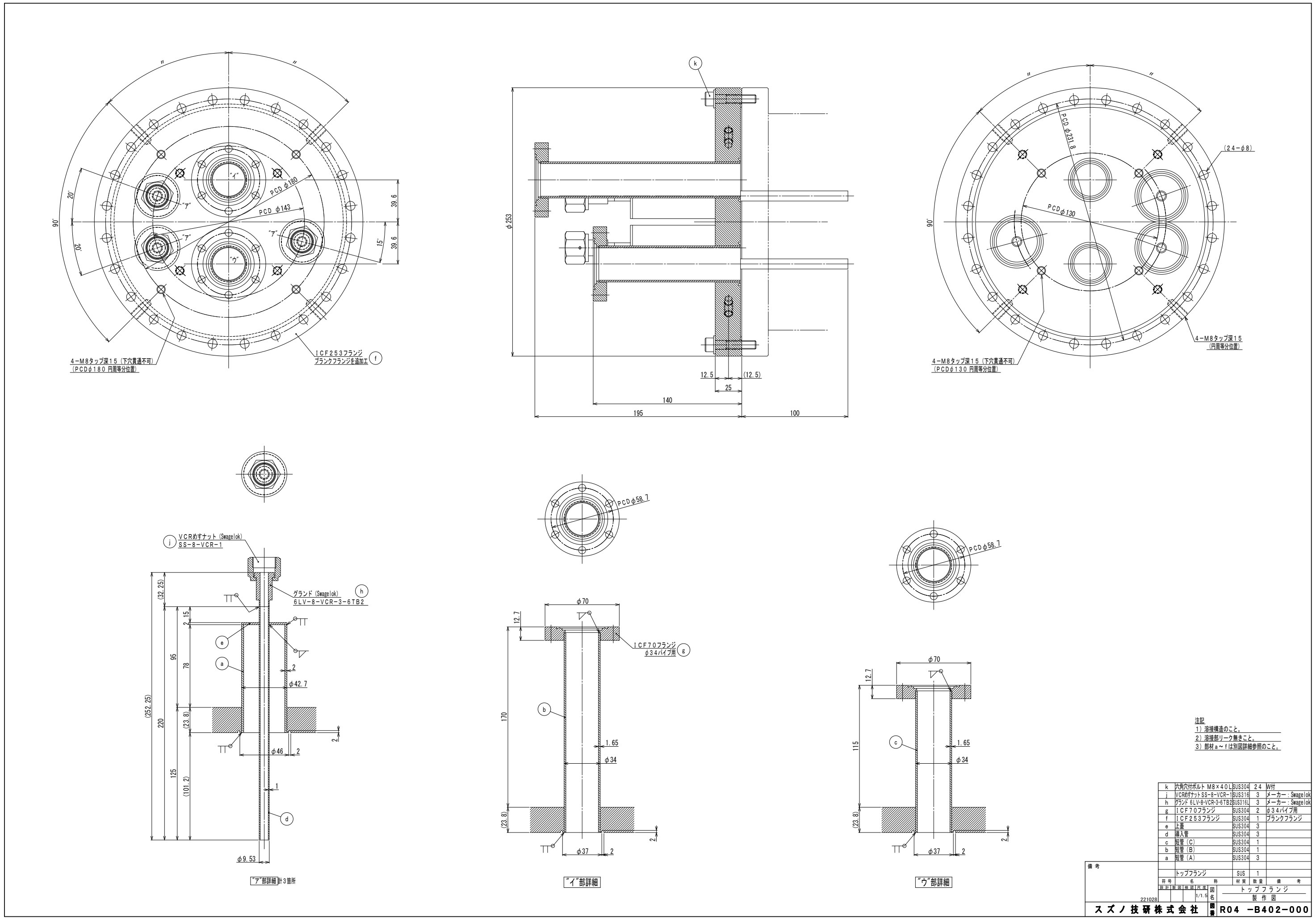

Figure A.2: Blueprint of the top flange.

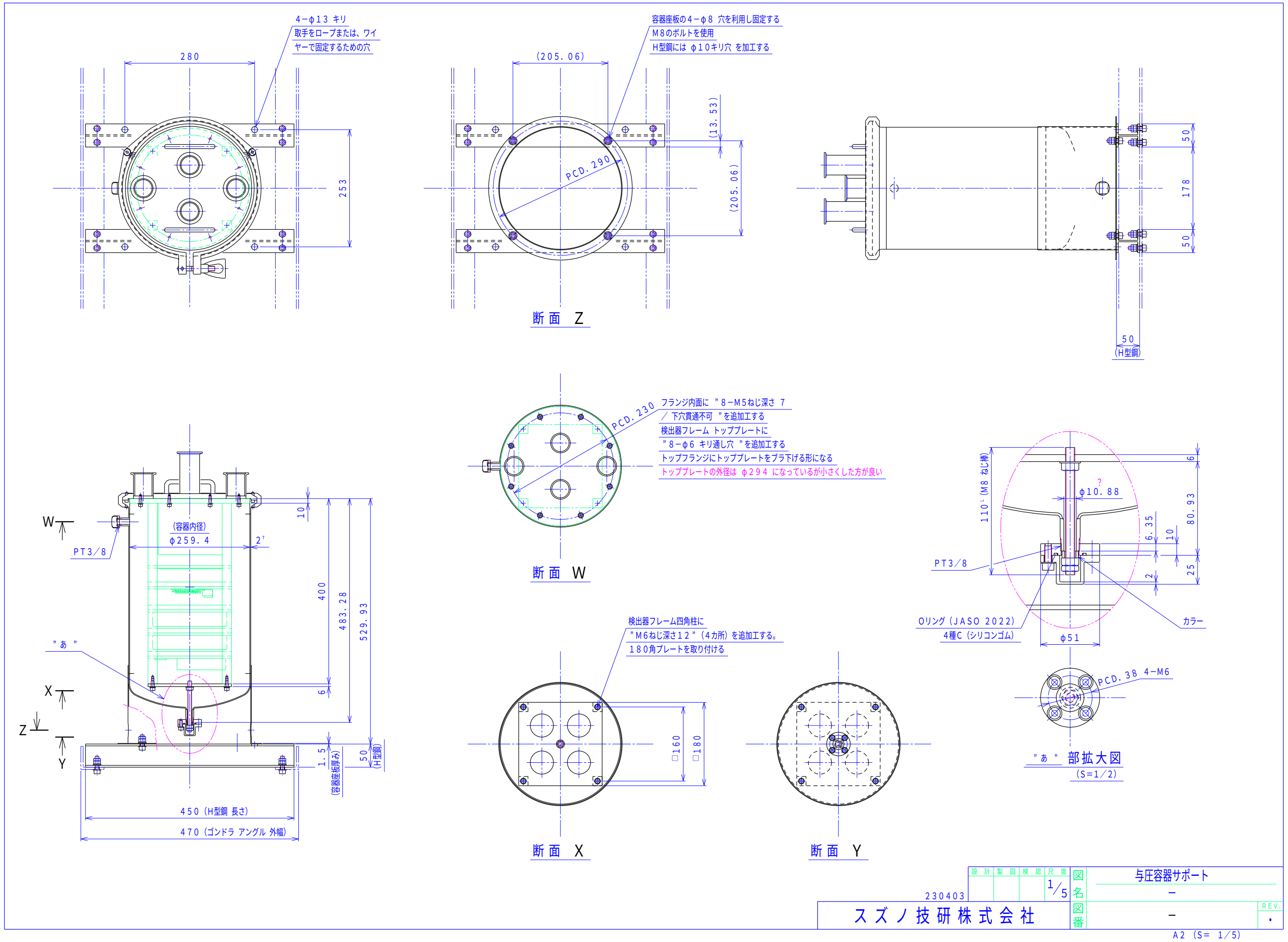

Figure A.3: Blueprint of Pressurized Vessel.

B LArTPC Event Zoo

This section of the appendix displays various events obtained throughout the flight and their explanations.

- **Cosmic Ray Penetration Events**

The two events below show cosmic ray penetration events leaving two signals on ch1 and ch2 and one signal on ch3. Figure B.1 shows the ch1 signal rising at around 15 μs and the second signal on ch1 ends at around 75 μs. Since the electron drift time is around 1 mm/μs, it can be understood that the cosmic ray entered the TPC from the side around 1.5 cm below the anode and left the TPC 7.5 cm below the anode. On the other hand, Figure B.2 shows a more vertical cosmic ray penetration due to an earlier rise of the first signal and a later end of the second signal on ch1.

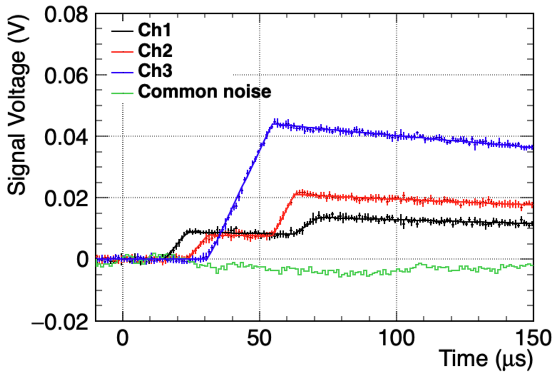

Figure B.1: Cosmic ray penetration example (more horizontal).

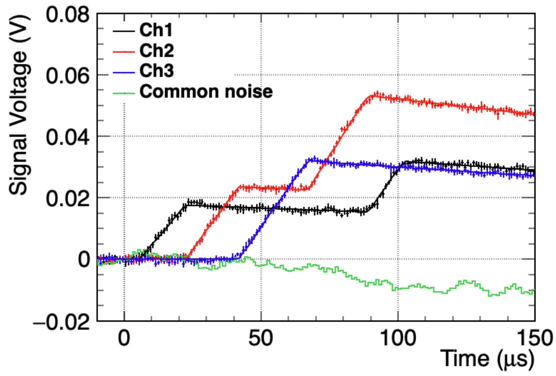

Figure B.2: Cosmic ray penetration example (more vertical).

- **Stopped Events**

The two events below show a cosmic ray stopped in the LArTPC. For a cosmic ray penetrating through the LArTPC, it will either leave the LArTPC from the side or through the cathode. In the former case, the last signal will be on ch1 which is the outermost anode pad. In the latter case, the LArTPC signal should end at the full electron drift time (110∼120 μs). Therefore, Figure B.3 shows a cosmic ray stopping around 7 cm below the ch3 (innermost) anode pad and Figure B.4 shows a cosmic ray stopping around 9 cm below the ch2 anode pad.

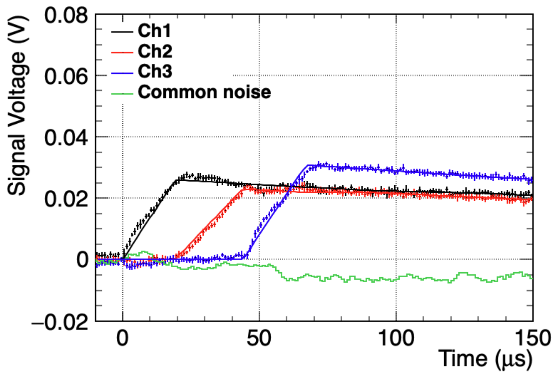

Figure B.3: Cosmic ray stopped in LArTPC (below ch3).

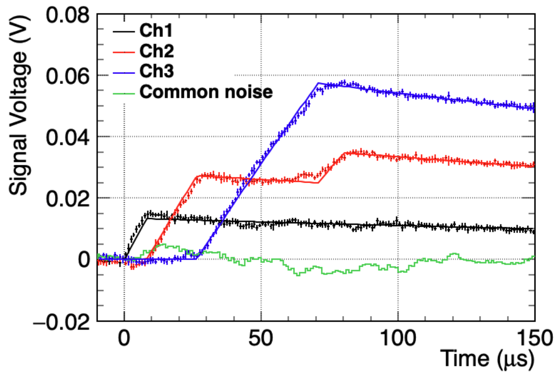

Figure B.4: Cosmic ray stopped in LArTPC (below ch2).

- **In flight Decay Candidates**

The two events below show only a signal in ch3 with the signal rise time ≥20 μs. Since the signal rise time is ≥20 μs, ionized electrons are only produced from 2 cm below the anode. Therefore these events could be explained by a neutral particle (not producing ionized electrons) decaying into charged particles in the LArTPC, from 2 cm below the anode. It could also be explained by a pair production from a gamma-ray. Furthermore, the ch3 signal ends before the full drift time which suggests that the decay products are stopped within the LArTPC.

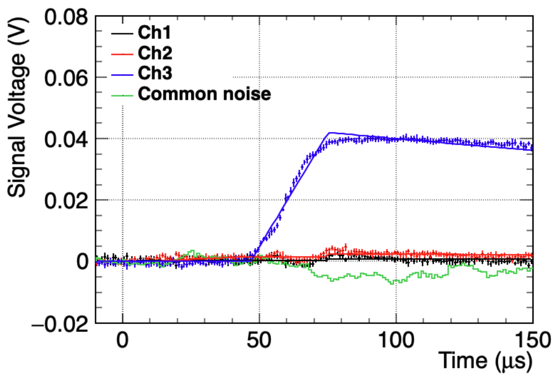

Figure B.5: Decay in LArTPC (5 cm below ch3).

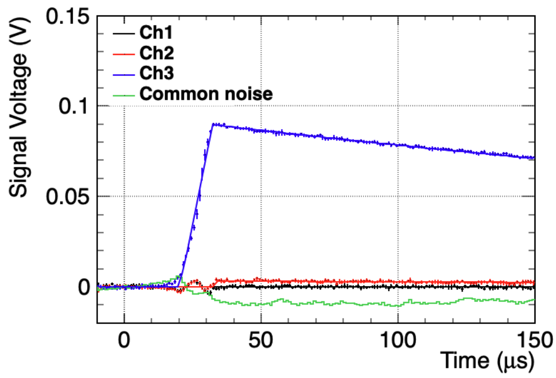

Figure B.6: Decay in LArTPC (2 cm below ch3).

Acknowledgements

I would like to express my deepest gratitude to everyone who has supported and guided me throughout the process of completing my master's thesis.

First and foremost, I would like to thank my advisor, Prof Yorita Kohei, for providing me the opportunity to conduct research at his lab. He has not only helped me in conducting proper research but also taught me how to think and take action independently. Also, I would like to thank Senior Scientist Tanaka Masashi. His expertise in liquid argon and in-depth knowledge of detector systems were always helpful during experiments and constructing simulations. Their unwavering support, guidance, and encouragement have helped me over the past three years. I truly believe that this engineering flight would not have been possible without them.

Also, I would like to thank JAXA's balloon group for providing the opportunity to conduct this engineering flight. Even though this flight was the first balloon experiment for GRAMS, they were very supportive and taught us the know-how of a balloon experiment from scratch.

Next, I would like to thank the secretary of our lab, Ms.Sakamoto. She has supported me in preparing for trips and purchasing equipment for research. She always lightened up the lab with her humor and it was of great help during the tough times. Although he has already graduated from this lab, I would like to thank Dr. Aoyama Kazutaka. As a former leader of this lab, he has helped me in numerous situations and I am grateful to have been able to conduct this engineering flight with him. Also, as the core member of this engineering flight, I would like to thank Utsumi Yorinobu who was in charge of the LAr handling system, and Arai Shota who designed the software system. Without them, this engineering flight wouldn't have been possible, and been such an amazing and unforgettable experience. Also, I would like to thank all other members of Yorita Lab for making my time at this lab enjoyable and for having deep conversations about physics and casual talks about life. It was always a source of motivation for me. I hope for their success and am excited about their potential contribution to the discovery of new physics.

Finally, special thanks are due to my family, especially my parents who have supported me financially and mentally for the past years at Waseda.

References

[1] F. Zwicky, "On the Masses of Nebulae and of Clusters of Nebulae," *Astrophysical Journal*, vol. 86, p. 217, oct 1937.

[2] V. C. Rubin, J. Ford, W. K., and N. Thonnard, "Rotational properties of 21 SC galaxies with a large range of luminosities and radii, from NGC 4605 (R=4kpc) to UGC 2885 (R=122kpc).," *Astrophysical Journal*, vol. 238, pp. 471–487, jun 1980.

[3] A. Bosma, "21-cm line studies of spiral galaxies. I. Observations of the galaxies NGC 5033, 3198, 5055, 2841, and 7331.," *Astronomical Journal*, vol. 86, pp. 1791–1824, dec 1981.

[4] D. Clowe, M. Bradač, A. H. Gonzalez, M. Markevitch, S. W. Randall, C. Jones, and D. Zaritsky, "A direct empirical proof of the existence of dark matter*," *The Astrophysical Journal*, vol. 648, p. L109, aug 2006.

[5] *Particle Dark Matter: Observations, Models and Searches.* Cambridge University Press, 2010.

[6] D. E. Dorfan, J. Eades, L. M. Lederman, W. Lee, and C. C. Ting, "Observation of antideuterons," *Phys. Rev. Lett.*, vol. 14, pp. 1003–1006, Jun 1965.

[7] L. Šerkšnytė, S. Königstorfer, P. von Doetinchem, L. Fabbietti, D. M. Gomez-Coral, J. Herms, A. Ibarra, T. Pöschl, A. Shukla, A. Strong, and I. Vorobyev, "Reevaluation of the cosmic antideuteron flux from cosmic-ray interactions and from exotic sources," *Phys. Rev. D*, vol. 105, p. 083021, Apr 2022.

[8] M. Aguilar *et al.*, "The alpha magnetic spectrometer (ams) on the international space station: Part ii — results from the first seven years," *Physics Reports*, vol. 894, pp. 1–116, 2021. The Alpha Magnetic Spectrometer (AMS) on the International Space Station: Part II - Results from the First Seven Years.

[9] K. Abe, H. Fuke, S. Haino, T. Hams, M. Hasegawa, K. Kim, M. Lee, Y. Makida, J. Mitchell, J. Nishimura, M. Nozaki, R. Orito, J. Ormes, N. Picot-Clemente, K. Sakai, M. Sasaki, E. Seo, R. Streitmatter, J. Suzuki, K. Tanaka, N. Thakur, A. Yamamoto, T. Yoshida, and K. Yoshimura, "The results from bess-polar experiment," *Advances in Space Research*, vol. 60, no. 4, pp. 806–814, 2017. Solar Energetic Particles, Solar Modulation and Space Radiation: New Opportunities in the AMS-02 Era.

[10] K. Sakai, H. Fuke, K. Yoshimura, M. Sasaki, K. Abe, S. Haino, T. Hams, M. Hasegawa, K. C. Kim, M. H. Lee, Y. Makida, J. W. Mitchell, J. Nishimura, M. Nozaki, R. Orito, J. F. Ormes, E. S. Seo, R. E. Streitmatter, N. Thakur, A. Yamamoto, and T. Yoshida, "Search for antideuterons of cosmic origin using the bess-polar ii magnetic-rigidity spectrometer," *Phys. Rev. Lett.*, vol. 132, p. 131001, Mar 2024.

[11] T. Aramaki, C. Hailey, S. Boggs, P. von Doetinchem, H. Fuke, S. Mognet, R. Ong, K. Perez, and J. Zweerink, "Antideuteron sensitivity for the gaps experiment," *Astroparticle Physics*, vol. 74, pp. 6–13, 2016.

[12] C. J. Hailey, T. Aramaki, W. W. Craig, L. Fabris, F. Gahbauer, J. E. Koglin, N. Madden, K. Mori, H. T. Yu, and K. P. Ziock, "Accelerator testing of the general antiparticle spectrometer; a novel approach to indirect dark matter detection," *Journal of Cosmology and Astroparticle Physics*, vol. 2006, p. 007, jan 2006.

[13] P. von Doetinchem, T. Aramaki, N. Bando, S. Boggs, H. Fuke, F. Gahbauer, C. Hailey, J. Koglin, S. Mognet, N. Madden, S. Okazaki, R. Ong, K. Perez, T. Yoshida, and J. Zweerink, "The flight of the gaps prototype experiment," *Astroparticle Physics*, vol. 54, pp. 93–109, 2014.

[14] W. B. Atwood *et al.*, "The large area telescope on the fermi gamma-ray space telescope mission," *The Astrophysical Journal*, vol. 697, p. 1071, may 2009.

[15] F. A. Harrison *et al.*, "The Nuclear Spectroscopic Telescope Array (NuSTAR) High-energy X-Ray Mission," *Astrophysical Journal*, vol. 770, p. 103, June 2013.

[16] V. Schoenfelder, "The first comptel source catalogue," *Astron. Astrophys. Suppl. Ser.*, vol. 143, p. 145, 2000.

[17] P. Agnes *et al.*, "First results from the darkside-50 dark matter experiment at laboratori nazionali del gran sasso," *Physics Letters B*, vol. 743, pp. 456–466, 2015.

[18] B. Abi *et al.*, "Deep Underground Neutrino Experiment (DUNE), Far Detector Technical Design Report, Volume I Introduction to DUNE," *JINST*, vol. 15, no. 08, p. T08008, 2020.

[19] R. Acciarri *et al.*, "Design and construction of the microboone detector," *Journal of Instrumentation*, vol. 12, p. P02017, feb 2017.

[20] E. Aprile, A. E. Bolotnikov, A. L. Bolozdynya, and T. Doke, *Noble Gas Detectors*. Wiley, 2008.

[21] S. Amoruso *et al.*, "Study of electron recombination in liquid argon with the icarus tpc," *Nuclear Instruments and Methods in Physics Research Section A: Accelerators, Spectrometers, Detectors and Associated Equipment*, vol. 523, no. 3, pp. 275–286, 2004.

[22] W. Walkowiak, "Drift velocity of free electrons in liquid argon," *Nucl. Instrum. Meth. A*, vol. 449, pp. 288–294, 2000.

[23] T. Aramaki, P. O. H. Adrian, G. Karagiorgi, and H. Odaka, "Dual mev gamma-ray and dark matter observatory - grams project," *Astroparticle Physics*, vol. 114, pp. 107–114, 2020.

[24] T. Sato, "Analytical model for estimating the zenith angle dependence of terrestrial cosmic ray fluxes," *PLOS ONE*, vol. 11, pp. 1–22, 08 2016.

[25] M.Sakurai, "Grams 実験のための地上プロトタイプ液体 artpc の製作と宇宙線粒子反粒子識別能力の検証," Master's thesis, Waseda University, 2022.

[26] H. FUKE, D. AKITA, I. IIJIMA, N. IZUTSU, Y. KATO, J. KAWADA, Y. MATSUZAKA, E. MIZUTA, M. NAMIKI, N. NONAKA, S. OHTA, Y. SAITO, T. SATO, M. SEO, A. TAKADA, K. TAMURA, M. TORIUMI, K. YAMADA, and T. YOSHIDA, "Opening of the new japanese balloon base at the taiki aerospace research field," *TRANSACTIONS OF THE JAPAN SOCIETY FOR AERONAUTICAL AND SPACE SCIENCES, AEROSPACE TECHNOLOGY JAPAN*, vol. 8, no. ists27, 2010.

[27] H. Fuke, "宇宙科学用大気球実験の概要." MeVガンマ線天文学研究会@京都大学, feb 2017. Tokyo, Japan, Accessed: 2024-06-12.

[28] H. Tanaka *et al.*, "Demonstration of a deformable structure equipped with a grating pattern printing measurement system -flight experiment in fy2023-." Balloon Symposium 2023, Oct 2023.

[29] M. Kokubun *et al.*, "レーザー周波数比較による一般相対論の高精度検証に向けた基礎実験 (ii)." Balloon Symposium 2023, Oct 2023.

[30] E. Aprile, U. G. Oberlack, A. Curioni, V. Egorov, K.-L. Giboni, S. Ventura, T. Doke, J. Kikuchi, K. Takizawa, E. L. Chupp, and P. P. Dunphy, "Preliminary results from the 1999 balloon flight of the Liquid Xenon Gamma-Ray Imaging Telescope (LXeGRIT)," in *X-Ray and Gamma-Ray Instrumentation for Astronomy XI* (K. A. Flanagan and O. H. W. Siegmund, eds.), vol. 4140, pp. 344 – 359, International Society for Optics and Photonics, SPIE, 2000.

[31] C. Mustafar, "The international standard atmosphere (isa)."

[32] A. Curioni, B. Fleming, W. Jaskierny, C. Kendziora, J. Krider, S. Pordes, M. Soderberg, J. Spitz, T. Tope, and T. Wongjirad, "A regenerable filter for liquid argon purification," *Nuclear Instruments and Methods in Physics Research Section A: Accelerators, Spectrometers, Detectors and Associated Equipment*, vol. 605, no. 3, pp. 306–311, 2009.

[33] S.Arai, "Demonstration of atmospheric mev gamma-ray detection by a balloon-borne liquid argon radiation detector for the grams experiment," Master's thesis, Tokyo University, 2023.

Dec. 20, 2023 Revised

Student ID Number: 5322A608-2

Pledge against Misconduct in Research Activities

Date of Submission (mm/dd/yyyy) 07/04/2024

To the Dean of the Graduate School of Advanced Science and Engineering

Graduate School of Advanced Science and Engineering,

Department of Pure & Applied Physics 2 nd/rd/th year student

Name Riki Nakajima

(Signature)

I have understood the definition of misconduct in research activities stated on the following pages. I pledge that I have not committed any such misconduct in my research activities and/or master's thesis. I fully understand that if I committed such any act(s) at any point(s) during my studies at Waseda University, I will be subject to disciplinary measures (such as suspension from school for an indefinite period, revoking of course credits, revoking of degree(s) regardless of whether I am a current or former student of Waseda University.

Confirmation of Taking Courses on Research Ethics

Date of Submission (mm/dd/yyyy) 07/04/2024

Name Riki Nakajima

(Signature)

I have taken the following course on research ethics to write my master's thesis.

✓	"Introduction to Academic and Research Integrity (For Life Sciences, Biological Science, Sciences, and Engineering) " offered by GEC
	"Research Ethics / Introduction to Research Ethics" offered by GEC
	A course offered by the department Course Name( )
	Others ( ) *Make sure to obtain the approval from the department chief through your supervisor before taking the course. *Attach a certificate of attendance.

Fraud and Misconduct (Fabrication, Falsification, Plagiarism) of Research Activities

Please pay attention to the following points when conducting research and writing your master's thesis.

◆Students must not fabricate nor falsify the existing documents, materials and data they refer to. These rules must be followed by not only professionals but also students.

※Fabrication: Claiming research results (including experiment data), material evidence, and/or documents as authentic or genuine even though they were known to be invented, created, made up, or/and forged.

※Falsification : Modifying or omitting all or part of research results, including data, intentionally. This includes, but is not limited to, alterations of the content data, the data format, and records of when the data was collected.

◆Intellectual honesty is critical to the advancement of research. You must give sufficient care in collecting, storing, and managing all research data. When collecting data, you must obtain the informed consent of all parties involved in providing information. Moreover, it is your responsibility to make sure that all the obtained data is securely protected.

In addition, if you refer to all or part (including, but not limited to, written words, charts, diagrams, or data) of a work (including, but not limited to, books, reports, lectures, lectures, internet sites), you must take sufficient care to avoid plagiarism.

Plagiarism is an intellectually dishonest act and is prohibited by copyright laws. Regardless of whether you are a professional or student, it is an act that you must not commit.

※Misappropriation・Plagiarism:
Those are to announce others' sentences, results, opinions, ideas, theories, including academic theories etc. as your own without appropriately describing the citation source.

◆Originality and creativity are also important to the advancement of research. It is the duty of all researchers, including student researchers, to give proper credit whenever they invoke work that is not their own. We must clearly distinguish between what is our own work and what is not. To do so, proper citation is necessary. In an academic paper, each place where you draw upon the work of others (i.e. a source) should be given a number and the source information must be given in the corresponding number at the bottom of the page (i.e. a footnote) or at the end of the paper (i.e. an endnote). Whatever you cite a source verbatim must be put in quotation marks. Depending on the field/journal/academic society/department, the order in which the source information is given differs. Listed below is the information that is generally included when citing a specific type of source, but you should consult the guidelines specific to your field/journal/academic society.

1. When citing a journal article, the author, journal title, volume number, year (month), and page(s) are given.
2. When citing a conference/symposium proceeding or/and presentation, the author/speaker, article/talk title, conference/symposium title, place the conference/symposium was held, year/month, issue volume, page number, publisher, publication year, are given.
3. When citing a book, the title, author, page, publisher, publication year, and page(s) are given.
4. When citing an internet site, the author, title, URL, and search date are given.

◆In a PowerPoint presentation, you may use a simplified version of the above, as long as there is sufficient information to locate the source. For example, when citing a journal article in a PowerPoint presentation, it may be sufficient to give the author, journal title, and the year it was published.